

大亚湾反应堆反中微子反常现象 的研究

(申请清华大学理学博士学位论文)

培养单位: 工程物理系

学 科: 物理学

研 究 生: 张 一 鸣

指导教师: 陈 少 敏 教 授

二〇一八年四月

**A study of the reactor antineutrino
anomaly at Daya Bay**

Dissertation Submitted to
Tsinghua University
in partial fulfillment of the requirement
for the degree of
Doctor of Philosophy
in
Physics
by
Zhang Yiming

Dissertation Supervisor : Professor CHEN Shaomin

April, 2018

关于学位论文使用授权的说明

本人完全了解清华大学有关保留、使用学位论文的规定，即：

清华大学拥有在著作权法规定范围内学位论文的使用权，其中包括：（1）已获学位的研究生必须按学校规定提交学位论文，学校可以采用影印、缩印或其他复制手段保存研究生上交的学位论文；（2）为教学和科研目的，学校可以将公开的学位论文作为资料在图书馆、资料室等场所供校内师生阅读，或在校园网上供校内师生浏览部分内容；（3）根据《中华人民共和国学位条例暂行实施办法》，向国家图书馆报送可以公开的学位论文。

本人保证遵守上述规定。

（保密的论文在解密后应遵守此规定）

作者签名： _____

导师签名： _____

日 期： _____

日 期： _____

摘要

中微子振荡的实验发现表明中微子有质量，意味着标准模型还不完善，或者存在超出标准模型的新物理。对它的精确测量研究，对于揭示中微子的本质与属性具有重大的意义。反应堆裂变反应产生的高流强反电子中微子是测量中微子振荡属性的理想来源，但是反应堆反电子中微子在短基线区域的振荡行为与三代中微子振荡理论模型的预期相比存在反常的缺失，这就是“反应堆反中微子反常”现象。本论文利用距离反应堆 300-500 米距离的大亚湾反应堆中微子实验近点探测数据对反应堆反电子中微子流强与能谱进行高精度的绝对测量，并且对反应堆反中微子反常现象进行研究。论文的主要工作包括以下三个方面：

1) 分析了大亚湾反应堆中微子实验近点探测器 1230 天的数据，通过选择来自反应堆反电子中微子反贝塔衰变过程产生的正电子快信号与延迟中子核俘获的慢信号，成功得到了超过两百万个反应堆反电子中微子信号事例。利用镅-铍源和镅-碳源产生的不同能量中子在探测器内独立重构了慢信号事例，研究了中子在实验中被不同核素俘获的概率与能量的关联性，并基于此精确模拟了中子在探测器物质中的输运和中子核俘获退激发过程，改善了模拟与数据的一致性，使得对中微子探测绝对效率的系统误差减小了 40%，进而提高了对反电子中微子流强测量的精度。

2) 精确测量了在大亚湾近点探测器中的反电子中微子流强，与反应堆核物理模型的理论预期进行了比较，实验与理论的比值为 $R = 0.952 \pm 0.014(\text{exp.}) \pm 0.023(\text{theo.})$ ，实验精度超过了理论模型的误差，并确认了大亚湾反应堆实验与其他短基线反应堆实验同样存在与三代中微子振荡模型预期不符的缺失现象。进一步地，结合对反电子中微子流强与反应堆燃料裂变周期关联性的测量，从惰性中微子和裂变核素中微子产额两个方面研究了导致该缺失的可能原因。

3) 精确测量了大亚湾反应堆反电子中微子能谱，在 5-7MeV 区间观测到不同于反应堆模型理论预期的结构，并且通过测量反应堆反电子中微子能谱随反应堆燃料裂变周期的关联情况，排除了由单一裂变核素（铀-235 或钚-239）引起该反常结构的假设。

关键词：中微子；中微子振荡；反应堆；反中微子反常；大亚湾实验

Abstract

The existence of neutrino oscillations indicates that neutrinos are massive, implying that the Standard Model is incomplete, or there is new physics beyond it. The precision measurement of neutrino oscillations is significant for revealing the nature and property of neutrinos. The intensive flux of electron antineutrino generated by the nuclear fissions inside the nuclear reactor is an ideal source for observing the neutrino oscillations. However, the measurements of reactor neutrino oscillations at a short baseline deviate from the prediction in the framework of three-flavor neutrino oscillations, with an anomalous deficit (referred to as the “reactor antineutrino anomaly”). Utilizing the near detectors of the Daya Bay reactor neutrino experiment with the short baseline varying from 300 to 500 meters away from the reactor, we conducted a precision absolute measurement on the reactor antineutrino flux and spectrum, and studied the reactor antineutrino anomaly. This thesis presents the studies in the following three aspects.

1) We analyzed the data sample of 1230 days in the Daya Bay near detectors and successfully observed more than two millions of reactor antineutrino events. The signal has a signature of a prompt signal of positron and a delayed signal of neutron capture on nuclei from the inverse beta decay (IBD) reaction. We used the ^{241}Am - ^{13}C and ^{241}Am - ^9Be sources to generate neutrons with different kinetic energy and independently simulate the IBD delayed signals inside the detector. The study of the correlations between the delayed spectrum and the neutron captures on various isotopes eventually enable us to obtain precision Monte Carlo simulation for the processes of neutron propagation in different detector materials and the de-excitation of nuclei after capturing the neutrons, improving the entire agreement between simulations and real detector performance. This led to a reduction of the systematic uncertainty by 40% on the absolute efficiency of IBD detection, hence improved the measurement precision of antineutrino flux.

2) We did a precision measurement on the flux of reactor antineutrinos in the Daya Bay near detectors and compared it with the prediction from the theoretical model, with a measurement to prediction ratio as $R = 0.952 \pm 0.014(\text{exp.}) \pm 0.023(\text{theo.})$, in which the theoretical uncertainty dominates. This confirmed the reactor antineutrino anomaly in Daya Bay as those observed in the other short-baseline reactor neutrino experiments. Furthermore, we measured the correlations of changes in antineutrino flux and the reactor

nuclear fuel evolution, and studied the possible reasons for reactor antineutrino anomaly in the two aspects of existence of sterile neutrino and the bias in model prediction of antineutrino yields from fissionable isotopes.

3) We did a precision measurement of the reactor antineutrino spectrum, observing an anomalous structure deviating from the reactor model prediction. We studied the correlations of changes in antineutrino spectra and the reactor nuclear fuel evolution. The observation disfavored the hypothesis that the anomalous structure is caused by only one fissionable isotope of ^{235}U or ^{239}Pu .

Key words: neutrino; neutrino oscillation; reactor; antineutrino anomaly; Daya Bay experiment

Contents

Chapter 1 Introduction	1
1.1 Neutrinos and Discoveries of Neutrinos	1
1.2 Neutrino Oscillation	3
1.2.1 Neutrino Oscillation in Vacuum	4
1.2.2 Neutrino Oscillation Experiments	9
1.3 Sterile Neutrinos and Neutrino Anomalies	16
1.3.1 Accelerator Neutrino Anomaly	17
1.3.2 Gallium Anomaly.....	19
1.3.3 Reactor Antineutrino Anomaly	20
Chapter 2 The Daya Bay Reactor Neutrino Experiment	29
2.1 The Experiment Site	29
2.2 Antineutrino Detector	33
2.2.1 AD Liquids.....	33
2.2.2 Signal Detection	34
2.3 Muon Veto System.....	35
2.4 Automatic Calibration Units.....	37
2.5 Data Taking	41
2.6 IBD Event Selection	43
Chapter 3 The Energy Non-linearity Model	45
3.1 Gamma Calibrations	45
3.2 Energy Non-linearity Model	46
3.3 Energy Non-linearity Model in Simulation.....	51
Chapter 4 IBD Detection Efficiency Study	58
4.1 Definition of Efficiency	58
4.2 Study of Correlated Efficiencies	59
4.3 Neutron Propagation and nGd De-excitation Study via Neutron Calibration ...	61
4.3.1 Mechanism of the AmC and AmBe Neutron Source	61
4.3.2 Impact of Neutron Kinetic Energy on Neutron Propagation Process	64
4.3.3 Event Selection and Background Subtraction For Neutron Calibration....	65
4.4 Monte Carlo Simulation	74

Contents

4.4.1	Neutron Related Efficiency in MC	74
4.4.2	Implementation of MC	75
4.5	IBD Detection Efficiency and Uncertainty	87
4.5.1	Comparison Between Data and MC	88
4.5.2	Neutron Detection Efficiency	89
4.5.3	MC Validation	97
4.5.4	IBD Detection Efficiency and Uncertainty	102
Chapter 5	Flux and Spectrum Measurements at Daya Bay	103
5.1	Reactor Antineutrino Flux	103
5.1.1	Flux Per Fission	103
5.1.2	Flux Evolution With Fuel Cycle	110
5.1.3	Flux Anomaly at Daya Bay	118
5.2	Reactor Antineutrino Spectrum	121
5.2.1	Spectrum and Its Evolution	121
5.2.2	Spectrum Anomaly at Daya Bay	123
Chapter 6	Summary and Outlook	126
References	129
Acknowledgement	137
Declaration	138
Appendix A	Systematic uncertainty calculation for accidental background subtraction in neutron calibration data	139
Resume and Publications	141

Denotation

SM	Standard Model
IBD	Inverse Beta Decay
CC	Charged-Current (weak interaction)
NC	Neutral-Current (weak interaction)
PMT	Photomultiplier Tube
NPP	Nuclear Power Plant
FST	Fourier Sine Transform
FCT	Fourier Cosine Transform
AD	Antineutrino Detector
ILL	Institut Laue-Langevin
PWR	Pressurized Water Reactor
BSM	Beyond Standard Model
LHC	Large Hadron Collider
CCQE	Charged-Current Quasi-Elastic
m.w.e.	meter water equivalent
EH	Experimental Hall
GdLS	Gd-doped Liquid Scintillator
LS	Liquid Scintillator
MO	Mineral Oil
IAV	Inner Acrylic Vessel
OAV	Outer Acrylic Vessel
SSV	Stainless Steel Vessel
ESR	Enhanced Specular Reflector, 3M [®]
ACU	Automated Calibration Unit
LED	Light-Emitting Diode
IWS	Inner Water Shield
OWS	Outer Water Shield
RPC	Resistive Plate Chamber
nGd	Neutron captured on Gadolinium
nH	Neutron captured on Hydrogen
PE	Photoelectron

Denotation

QE	Quantum Efficiency
LAB	Linear Alkylbenzene
PPO	2,5-di-phenyloxazole
bis-MSB	p-bis-(o-methylstyryl)-benzene
THMA	3,5,5-tri-methylhexanoic acid
ppb	Parts Per Billion
SPE	Single Photoelectron
ADC	Analog to Digital Converter
DAQ	Data acquisition
DCS	Detector control system
MC	Monte Carlo
PDF	Probability Distribution Function
GS	Ground State
ES	Excited State
NE	Non-equilibrium
SNF	Spent Nuclear Fuel

Chapter 1 Introduction

This chapter will give a brief introduction for the concepts about neutrino, neutrino oscillation, and the corresponding experiments to measure the properties of neutrinos.

1.1 Neutrinos and Discoveries of Neutrinos

In the well-established Standard Model^[1] (SM), twelve elementary fermions (and their respective antiparticles) in three generations are identified to build up the matter world, with four bosons to carry out the interactions. Each generation of fermions involve two quarks, an electron-like charged lepton, and a partner neutrino. The three generations charged leptons are electron, muon, and tau. The respective three neutrinos are electron neutrino, muon neutrino, and tau neutrino. Unlike their partner leptons, neutrinos have no electric charge, and are nearly massless (less than eV). In the Standard Model, the neutrinos are left-handed and must be massless. Later, more and more experiments confirmed that neutrinos can oscillate among different flavors, indicating that neutrinos are massive and the Standard Model is incomplete, or there is new physics beyond it. Details about the neutrino oscillation will be introduced in Section 1.2. With finite mass and no electric charge, neutrinos can only interact with matter through gravity and weak forces. In the Standard Model, neutrinos are created in the weak interaction process, together with their charged partner leptons. A typical interaction is the beta decay,

$$n \rightarrow p + e + \bar{\nu}_e, \quad (1-1)$$

which generates an electron antineutrino.

The story of neutrino began with the beta decay as well. In the early decades of 1900s, the process of beta decay occurring in the transmutation between nuclei were studied intensely through the emitted beta ray (electron) . The definite amount of nuclear energy released in the process was thought to be shared by the recoiled nucleus and emitted electron. Energy conservation and momentum conservation require that the emitted electron should carry away nearly all the released nuclear energy. However, in 1914, James Chadwick observed a continuous spectrum of energies for the emitted electrons in beta decays, neither the expected single energy, nor even a set of discrete

energies^[2]. This contradicted the longstanding cornerstone of energy conservation law for physics. Niels Bohr even suspected that the time-honored energy conservation law may not hold in these cases of beta decays, except as a statistical law.

To save the energy conservation theorem, in 1930, Wolfgang Pauli proposed another nucleon what he himself thought as a “desperate remedy”, in a letter to a conference in Tübingen^[3]. The so-called nucleon should have a spin 1/2 and a finite mass. It comes out together with electron in the beta decay without being detected, leading to a continuous spectrum for the observed electron energy and ensuring both energy and momentum conservation at the same time.

In 1934, Enrico Fermi formulated a four-fermion theory^[4,5] for the neutron decay in equation (1-1), assuming a so-called weak force working in the process. Fermi’s theory successfully predicted the continuous spectrum for the emitted electrons in the beta decay. To detect the new particle, a possible way suggested by Fermi’s theory is to use the inverse beta decay (IBD) process,



in which the electron antineutrino is captured by a proton and transforms into a neutron and a positron. In so doing, all the particles in the final state are observed. Unfortunately, the weak force is so weak that to stop a single neutrino in the target one needs a light-year thick lead. A solution to this is to have intensive neutrino flux and large target mass to increase the probability of neutrino interaction with matter.

In 1956, the team of Clyde Cowan and Frederick Reines from the Los Alamos National Laboratory built a neutrino detector just 11 meters from a 700 MW reactor at Savannahrive Site. The detector included 300 liters liquid scintillator and 90 photomultiplier tubes (PMTs). The first one serves as a target and illuminating material. The PMTs are employed to detect the light emitted in the neutrino interaction process. By using the electron antineutrinos produced by the nuclear fissions, they successfully observed electron antineutrinos via IBD reaction^[6,7].

In 1962, the team of Leon M. Lederman, Melvin Schwartz, and Jack Steinberger confirmed that the neutrino from pion decay is genuinely different from the neutrino from beta decay by the experiment at the Brookhaven National Laboratory^[8]. The 15 GeV proton beam from accelerator produced abundant pions, which would decay in flight and

generate a muon neutrino beam via

$$\pi^+ \rightarrow \mu^+ + \nu_\mu . \quad (1-3)$$

The muon neutrino subsequently interacted with neutron via

$$\nu_\mu + n \rightarrow p + \mu^- . \quad (1-4)$$

The charged muon showed its tracks in the spark chamber.

In July 2000, the DONUT collaboration from Fermilab eventually detected tau neutrino^[9,10] via the similar reaction (1-4) where the μ is replaced with τ . The created tau left a short track of several millimeters in the nuclear emulsion before its decay. The discovery of tau neutrino successfully encloses the three generation framework for elementary fermions in the Standard Model.

In 1957, M. Goldhaber, L. Gerodzins and A. W. Sunyar found that neutrinos are left-handed from an experiment that measured the helicity of the neutrino by analyzing the circular polarization and resonant scattering of γ rays following orbital electron capture^[11]. In the Standard Model, all neutrinos are left-handed. Therefore they must be massless. If they have mass, they can not travel at speed of light. Under the CPT (C: interchange particles and antiparticles, P: parity operation, T: time-reversal) theorem in quantum field, a left-handed neutrino ν_L must correspond to a $\bar{\nu}_R$. This means there is no right-handed neutrino ν_R or left-handed antineutrino $\bar{\nu}_L$ existing. However, this picture was overturned by a number of discoveries in neutrino oscillations starting from 1996.

1.2 Neutrino Oscillation

Neutrino oscillation is a quantum mechanical phenomenon due to the fact of non-zero neutrino masses and the resultant neutrino mixing between neutrino flavors and mass eigenstates^[1]. The neutrino of one flavor can transform into another flavor during its propagation process. This means when the produced neutrino is a particular flavor (ν_e or ν_μ or ν_τ), it can change its identity to the other two flavors with a certain probability after any given time.

The first concept of neutrino oscillation was proposed by Bruno Pontecorvo in 1957^[12]. He raised an issue of neutrino-antineutrino oscillation which has never been

observed by experiments. However the idea of neutrino flavor oscillation was latter formulated by Maki, Nakagawa, and Sakata in 1962^[13], and subsequently elaborated by Bruno Pontecorvo in 1967^[14].

Other than the flavor oscillation in vacuum, when neutrinos propagate inside matter, the scattering with electrons and nucleons via weak interactions would affect the flavor oscillation. Lincoln Wolfenstein firstly proposed that these scatterings would change the neutrino effective mass eigenstates in 1978-1979^[15,16]. Later in 1985, Stanislav Mikheyev and Alexei Smirnov formulated how the neutrino oscillation is resonantly enhanced by the coherent elastic forward scattering with electron^[17]. This extra oscillation effect in matter is called the Mikheyev - Smirnov - Wolfenstein (MSW) effect, also referred to as the matter effect. Soon after the matter effect was introduced, Hans Bethe, S. Peter Rosen *et al.* applied the theory to solve the solar neutrino deficit problem (the solar neutrino experiments all measured smaller solar neutrino flux than the model prediction) preliminarily^[18,19].

1.2.1 Neutrino Oscillation in Vacuum

Generally, the neutrino mixing between the flavor and mass eigenstates can be expressed as

$$|\nu_\alpha\rangle = \sum_j U_{\alpha j}^* |\nu_j\rangle, \quad (1-5)$$

where α represents the neutrino flavors of (e, μ, τ), $|\nu_j\rangle$ represents the mass eigenstates, and U is the neutrino mixing matrix which is assumed to be unitary. For the neutrino flavor eigenstates, the precision electroweak measurements of the Z -boson resonance^[20] concluded that only three light flavor neutrinos are coupled to Z . For the neutrino mass eigenstates, the total number of them n can, in general, be greater than 3 if there are additional so-called "sterile" neutrinos existing, for example. These sterile neutrinos have no interactions with the Standard Model particles, and thus give no access for direct detection. The experimental hints for their existence will be discussed in Section 1.3. At present, most of the compelling neutrino oscillation results confirmed that at least three of the neutrino mass eigenstates ν_j , say ν_1, ν_2, ν_3 , must exist and have different masses from each other, $m_1 \neq m_2 \neq m_3$, all very small $m_{1,2,3} \lesssim 1$ eV.

The time evolution of the neutrino mass eigenstate $|\nu_j\rangle$ during its propagation process

can be obtained by solving the Schrödinger equation

$$i \frac{\partial}{\partial t} |\nu_j(t)\rangle = \mathcal{H} |\nu_j(t)\rangle . \quad (1-6)$$

Upon the production and detection, the real localized neutrinos are described by superpositions of plane waves, or called as the wave packets. More discussions of the wave-packet treatment can be found in the reference^[21]. For a brief introduction of the oscillation mechanism, we will use the simple plane-wave treatment for the neutrino here.

The solution of a plane-wave description for all space-time is expressed as

$$|\nu_j(t)\rangle = e^{-i(E_j t - \vec{p} \cdot \vec{x})} |\nu_j(0)\rangle , \quad (1-7)$$

where E_j is the energy of mass eigenstate j (eigenvalue of Hamiltonian \mathcal{H} , $E_j^2 = p^2 + m_j^2$), \vec{p} is the three-dimensional momentum, and \vec{x} is the present position relative to the initial position. As the neutrino energy studied in experiments is generally greater than 1 MeV while the rest mass is less than 1 eV, $E_j \gg m_j$, a reasonable approximation in this ultrarelativistic limit holds

$$E_j = \sqrt{p^2 + m_j^2} \approx p + m_j^2/2E_j = p + m_j^2/2E , \quad (1-8)$$

where E is the neutrino energy. Since neutrinos travel almost at the speed of light. the neutrino propagation direction with a distance $x = L = t$ (in natural unit). Then equation (1-7) reads as

$$|\nu_j(L)\rangle = e^{-im_j^2 L/2E} |\nu_j(0)\rangle . \quad (1-9)$$

As the neutrinos are created and detected in flavor eigenstates, what we concern is the probability for a neutrino created as one flavor ν_α and detected as another flavor ν_β after a propagation length of L from the source. The probability amplitude reads as

$$\begin{aligned} \text{Amp}(\nu_\alpha \rightarrow \nu_\beta) &= \langle \nu_\beta | \nu_\alpha(L) \rangle = \langle \sum_k U_{\beta k} \nu_k | \sum_j U_{\alpha j}^* e^{-im_j^2 L/2E} \nu_j(0) \rangle \\ &= \sum_j U_{\alpha j}^* U_{\beta j} e^{-im_j^2 L/2E} \end{aligned} \quad (1-10)$$

Therefore the oscillation probability for $\nu_\alpha \rightarrow \nu_\beta$ is the modulus square of amplitude as

$$\begin{aligned}
 \text{Prob}(\nu_\alpha \rightarrow \nu_\beta) &= |\text{Amp}(\nu_\alpha \rightarrow \nu_\beta)|^2 \\
 &= \sum_{jk} U_{\alpha j}^* U_{\beta j} U_{\alpha k} U_{\beta k}^* e^{-i(m_j^2 - m_k^2)L/2E} \\
 &= \delta_{\alpha\beta} - 4 \sum_{j>k} \mathcal{R}(U_{\alpha j}^* U_{\beta j} U_{\alpha k} U_{\beta k}^*) \sin(\Delta m_{jk}^2 \frac{L}{4E}) \\
 &\quad + 2 \sum_{j>k} \mathcal{J}(U_{\alpha j}^* U_{\beta j} U_{\alpha k} U_{\beta k}^*) \sin(\Delta m_{jk}^2 \frac{L}{2E}),
 \end{aligned} \tag{1-11}$$

where the squared mass difference $\Delta m_{jk}^2 \equiv m_j^2 - m_k^2$.

For the antineutrino case, with the CPT symmetry, we have

$$\begin{aligned}
 |\bar{\nu}_\alpha\rangle &= \sum_j U_{\alpha j} |\bar{\nu}_j\rangle \\
 \text{Prob}(\bar{\nu}_\alpha \rightarrow \bar{\nu}_\beta) &= \text{Prob}(\nu_\beta \rightarrow \nu_\alpha).
 \end{aligned} \tag{1-12}$$

It is easy to deduce the oscillation probability for $\bar{\nu}_\alpha \rightarrow \bar{\nu}_\beta$ as

$$\begin{aligned}
 \text{Prob}(\bar{\nu}_\alpha \rightarrow \bar{\nu}_\beta) &= \delta_{\alpha\beta} - 4 \sum_{j>k} \mathcal{R}(U_{\alpha j}^* U_{\beta j} U_{\alpha k} U_{\beta k}^*) \sin(\Delta m_{jk}^2 \frac{L}{4E}) \\
 &\quad - 2 \sum_{j>k} \mathcal{J}(U_{\alpha j}^* U_{\beta j} U_{\alpha k} U_{\beta k}^*) \sin(\Delta m_{jk}^2 \frac{L}{2E}),
 \end{aligned} \tag{1-13}$$

Comparing equation (1-11) and equation (1-13), we can find the difference term for neutrino and antineutrino oscillations, called the CP asymmetry,

$$A_{CP}^{\alpha\beta} = \text{Prob}(\nu_\alpha \rightarrow \nu_\beta) - \text{Prob}(\bar{\nu}_\alpha \rightarrow \bar{\nu}_\beta) = 4 \sum_{j>k} \mathcal{J}(U_{\alpha j}^* U_{\beta j} U_{\alpha k} U_{\beta k}^*) \sin(\Delta m_{jk}^2 \frac{L}{2E}). \tag{1-14}$$

If the neutrino mixing matrix is in complex, the term would be nontrivial. Otherwise, it would vanish and there is no CP violation.

The neutrino mixing matrix is also known as the Pontecorvo-Maki-Nakagawa-Sakata (PMNS) matrix. In the framework of three generations of neutrino, the PMNS matrix can be parameterized for convenience with three mixing angles (θ_{12} , θ_{23} , θ_{13}), a Dirac CP violation phase (CPV) δ , and additionally two Majorana CP violation phases (α_{21} , α_{31}) if all three neutrino mass eigenstates are Majorana particles, by the Particle

Data Group^[1]:

$$\begin{aligned}
 U_{\text{PMNS}} &= \begin{pmatrix} U_{e1} & U_{e2} & U_{e3} \\ U_{\mu1} & U_{\mu2} & U_{\mu3} \\ U_{\tau1} & U_{\tau2} & U_{\tau3} \end{pmatrix} \\
 &= \begin{pmatrix} 1 & 0 & 0 \\ 0 & c_{23} & s_{23} \\ 0 & -s_{23} & c_{23} \end{pmatrix} \times \begin{pmatrix} c_{13} & 0 & s_{13}e^{-i\delta} \\ 0 & 1 & 0 \\ -s_{13}e^{i\delta} & 0 & c_{13} \end{pmatrix} \times \begin{pmatrix} c_{12} & s_{12} & 0 \\ -s_{12} & c_{12} & 0 \\ 0 & 0 & 1 \end{pmatrix} \quad (1-15) \\
 &\quad \times \text{diag}(1, e^{i\alpha_{21}/2}, e^{i\alpha_{31}/2}) \\
 &= \begin{pmatrix} c_{12}c_{13} & s_{12}c_{13} & s_{13}e^{-i\delta} \\ -s_{12}c_{23} - c_{12}s_{23}s_{13}e^{i\delta} & c_{12}c_{23} - s_{12}s_{23}s_{13}e^{i\delta} & s_{23}c_{13} \\ s_{12}s_{23} - c_{12}c_{23}s_{13}e^{i\delta} & -c_{12}s_{23} - s_{12}c_{23}s_{13}e^{i\delta} & c_{23}c_{13} \end{pmatrix} \\
 &\quad \times \text{diag}(1, e^{i\alpha_{21}/2}, e^{i\alpha_{31}/2}),
 \end{aligned}$$

where $c_{ij} \equiv \cos \theta_{ij}$, $s_{ij} \equiv \sin \theta_{ij}$, the angles $\theta_{ij} = [0, \pi/2]$.

Combining equations (1-11) and (1-15), we can have a panorama of the fundamental parameters characterizing the three-flavor neutrino oscillations:

- (1) Three mixing angles (θ_{12} , θ_{23} , θ_{13});
- (2) One Dirac CPV phase δ , and if necessary, two additional Majorana CPV phases (α_{21} , α_{31}) for Majorana neutrinos;
- (3) Three neutrino masses (m_1 , m_2 , m_3).

To have a minimally extended Standard Model with massive neutrinos, we need to add these 7 or 9 additional parameters, depending on whether neutrinos are Dirac or Majorana particles, in which the later means that the Majorana particle is indential to its antiparticle. As the two extra Majorana CPV phases do not change the probability of neutrino oscillation^[22], they can not be directly measured by neutrino oscillation experiments. The neutrino oscillation parameters except for the Majorana CPV phases, have been measured by various neutrino experiments, which would be briefly reviewed in Section 1.2.2. A remained critical question about neutrino oscillation is the so-called ‘‘mass hierarchy’’ (MH) problem. By definition, we number the first two mass eigenstates by mass order $m_1 < m_2$. A natural assumption for the hierarchy of the three neutrino masses is $m_1 < m_2 < m_3$, which is called the normal hierarchy (NH); on the contrary, the order of $m_3 < m_1 < m_2$ is called the inverted hierarchy (IH). As the squared mass differences have $\Delta m_{12}^2 \ll |\Delta m_{23}^2|$

from experimental measurements, the order of $m_1 < m_3 < m_2$ is excluded.

Table 1.1 shows a global fit for the three-flavor neutrino oscillation parameters with the current neutrino oscillation data in 2016^[1,23]. Both the results for normal hierarchy and inverted hierarchy (in the brackets) are shown in the table. From Table 1.1 we can see that θ_{13} is quite small compared with θ_{12} and θ_{23} . Before the precise measurement of θ_{13} by the new generation of reactor antineutrino experiments, people had worried about the question whether θ_{13} equals 0 or not. If $\theta_{13} = 0$ indeed, it would be impossible to measure the Dirac CPV phase δ by long baseline neutrino experiments, as δ is always coupled with $\sin^2 \theta_{13}$ in the PMNS matrix. This would affect the design of the future neutrino oscillation experiments. Fortunately, in 2012, the Daya Bay reactor antineutrino experiment published the first measurement of a non-zero θ_{13} at 5.2σ confidence level, $\sin^2 2\theta_{13} = 0.092 \pm 0.016(\text{stat.}) \pm 0.005(\text{syst.})$ ^[24].

Table 1.1 The best-fit values and the 3σ allowed regions of the three-flavor neutrino oscillation parameters for the normal and inverted hierarchies in brackets, from a global fit with the present neutrino oscillation data^[23]. The new parameter $\Delta m^2 \equiv m_3^2 - (m_1^2 + m_2^2)/2$. For the Dirac CPV phase δ , only the best-fit value and 2σ allowed region is given in the table, as physical values of δ are disfavored at 3σ level.

Parameter	Best-fit	3σ
Δm_{21}^2 [10^{-5} eV ²]	7.37	6.93 - 7.97
$ \Delta m^2 $ [10^{-3} eV ²]	2.50	2.37 - 2.63
	(2.46)	(2.33 - 2.60)
$\sin^2 \theta_{12}$	0.297	0.250 - 0.354
$\sin^2 \theta_{23}$	0.437	0.379 - 0.616
	(0.569)	(0.383 - 0.637)
$\sin^2 \theta_{13}$	0.0214	0.0185 - 0.0246
	(0.0218)	(0.0186 - 0.0248)
δ/π	1.35	0.92 - 1.99 (2σ)
	(1.32)	(0.83 - 1.99) (2σ)

A simple scenario of two-flavor neutrino mixing, just as in the initial Maki, Nakagawa, and Sakata paper^[13], is also useful and thought-provoking. In the previous oscillation experiments and in some specific cases today, the data were/are analyzed under this two-neutrino frame with sufficient precision. The PMNS matrix in this scenario is simplified

as a 2×2 matrix of an Euler rotation:

$$U = \begin{pmatrix} \cos \theta & \sin \theta \\ -\sin \theta & \cos \theta \end{pmatrix}, \quad (1-16)$$

where θ is the mixing angle. With the squared mass difference Δm^2 between the two mass eigenstates, for the case an initial neutrino of one flavor oscillates as another flavor, the complicated equation (1-11) turns out to be as simple as

$$\text{Prob}(\nu_\alpha \rightarrow \nu_\beta) = \sin^2 2\theta \sin^2\left(\frac{\Delta m^2 L}{4E}\right), \quad (\alpha \neq \beta). \quad (1-17)$$

This formula has been used in the data analysis of the atmospheric neutrino oscillation at Super-K for the case $\alpha = \mu$, $\beta = \tau$ (this is the first compelling evidence for neutrino oscillation)^[25], and also in the long-baseline reactor neutrino experiment KamLAND for the case $\alpha = e$, $\beta = \mu$ ^[26,27].

We can also calculate the Hamiltonian in the neutrino flavor basis with $\mathcal{H}_{\alpha\beta} = \langle \nu_\alpha | \mathcal{H} | \nu_\beta \rangle$. The result reads as

$$\mathcal{H} = \frac{\Delta m^2}{4E} \begin{pmatrix} -\cos 2\theta & \sin 2\theta \\ \sin 2\theta & \cos 2\theta \end{pmatrix}, \quad (1-18)$$

with some identity matrix already subtracted from the Hamiltonian by a phase shift, which has no effect on the oscillation probability.

1.2.2 Neutrino Oscillation Experiments

Neutrino oscillation experiments are categorized into two types. One is to measure the probability of $\text{Prob}(\nu_\alpha \rightarrow \nu_\alpha)$ referred to as survival probability, while the other measures the case for $\alpha \neq \beta$, the probability of $\text{Prob}(\nu_\alpha \rightarrow \nu_\beta)$ referred to as transition probability. Moreover, according to the neutrino sources, neutrino oscillation experiments are also classified into four types: solar neutrino, atmospheric neutrino, accelerator neutrino, and reactor neutrino experiments. From the oscillation probability equation (1-17), we can see that the oscillation probability depends on the term $\sin^2(\Delta m^2 L/4E)$. Since the squared mass difference Δm^2 is fixed by nature, neutrino oscillation experiments are designed with a proper L/E in order to measure specific oscillation parameters, for

the man-made neutrino sources of reactor neutrinos and accelerator neutrinos. If the condition of $\Delta m^2 L/2E \sim 1$ is satisfied, the experiments can be sensitive to the squared mass difference. Since the solar neutrinos and atmospheric neutrinos are created by nature, the spectra and the propagation distances between the sources and detectors can not be artificially controlled. These experiments can only be used for the studies in the sensitive region given by nature. Table 1.2 shows the sensitivity of Δm^2 for neutrino oscillation experiments with different sources. Also listed are the neutrino types, mean energies and general baselines.

Table 1.2 Sensitivity of different neutrino oscillation experiments^[1]

Source	ν types	\bar{E} [MeV]	L [km]	$\min(\Delta m^2)$ [eV ²]
Reactor	$\bar{\nu}_e$	~ 1	1	$\sim 10^{-3}$
Reactor	$\bar{\nu}_e$	~ 1	100	$\sim 10^{-5}$
Accelerator	$\nu_\mu, \bar{\nu}_\mu$	$\sim 10^3$	1	~ 1
Accelerator	$\nu_\mu, \bar{\nu}_\mu$	$\sim 10^3$	1000	$\sim 10^{-3}$
Atmospheric vs	$\nu_{\mu,e}, \bar{\nu}_{\mu,e}$	$\sim 10^3$	10^4	$\sim 10^{-4}$
Sun	ν_e	~ 1	1.5×10^8	$\sim 10^{-11}$

1.2.2.1 Reactor Neutrino Oscillation Experiments

The nuclear reactor is a powerful source of electron antineutrinos. It was ever used as the source in the discovery of neutrino in the Savannah River Experiment. Since then, many reactor neutrino experiments have been built up to detect neutrinos via the IBD reactions, with an energy threshold of 1.8 MeV. Generally the commercial reactors in the nuclear power plants (NPPs) use the low-enriched uranium materials as the nuclear fuels. The electron antineutrinos are produced by the beta decays of the fission fragments from the fissionable isotopes, primarily ^{235}U , ^{238}U , ^{239}Pu , and ^{241}Pu , accounting for more than 99% of the total fissions^[28]. As the burn-up of the fuel increases, more and more plutonium nuclei are produced via the neutron capture on ^{238}U , giving increasing fission fraction in the reactor. Each fission of these four primary isotopes will release about 6 neutrinos and ~ 200 MeV energy, on average. The other flavor of electron neutrino ν_e can also be created by the fission fragments via beta plus decay, but the total rate is negligible (less than 10^{-5})^[29] compared with that of the antineutrino. The electron antineutrino energy spectra per fission from four primary fissionable isotopes and the IBD

reaction cross-section are shown in Fig. 1.1. The detected neutrino spectra of $S(E)\sigma(E)$ after normalization have discrepancies among different isotopes, while the mean neutrino energies are all about 3 MeV. Additionally, because of the energy threshold 1.8 MeV in IBD reaction, only about 1.5 $\bar{\nu}_e$ per fission (*i.e.*, $\sim 25\%$) of the total antineutrinos can be detected, with an extremely small cross-section^[30].

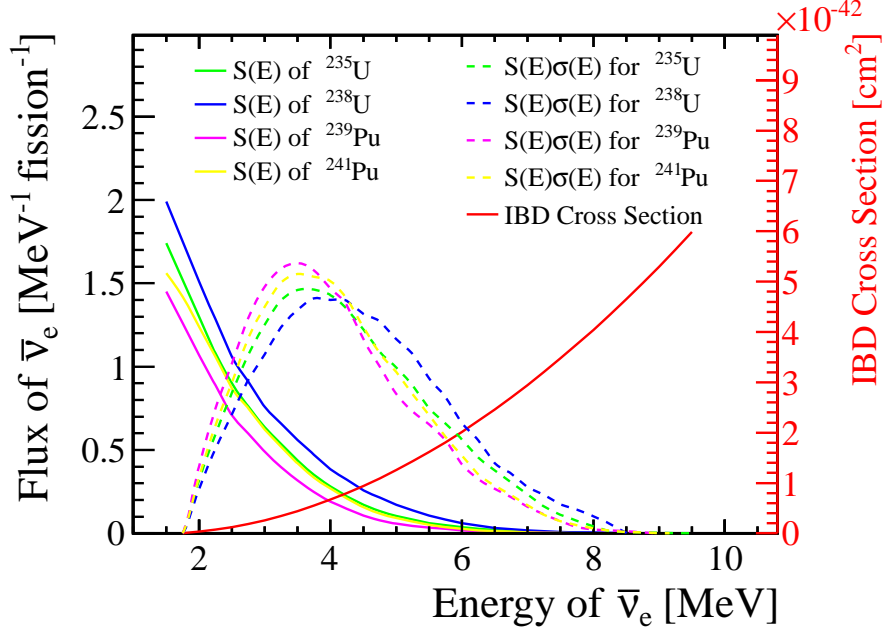


Figure 1.1 The electron antineutrino energy spectra per fission from four primary fissionable isotopes^[31,32] are shown with solid colorful lines. The red line and axis on the right side is for the IBD reaction cross-section^[33]. The detected neutrino spectra of $S(E)\sigma(E)$ are the dashed lines with corresponding colors, while each of them is self-normalized. The y-axis for these normalized spectra is not drawn.

Because of this low energy neutrino spectra, the detection of coincidence events with positron and neutron signals from IBD reaction is essential to identify the neutrino signals and reject the backgrounds, especially from the natural radioactivities. Moreover, the gadolinium-loaded liquid scintillator has been widely used in recent reactor neutrino experiments, to highly improve the neutron detection efficiency. Neutron captured on hydrogen in liquid scintillator leads to a 2.2 MeV single γ emission, the neutron captured on gadolinium isotopes produces multiple γ 's, with a total energy about 8 MeV. These energy feature help a lot in the neutrino detection. Another important type of backgrounds originates from the spallation processes induced by cosmic rays. Since high energy muons can travel deeply under the ground, producing not only spallation neutrons but also other short-lived isotopes which can have subsequent cascade decays, mimicking the IBD events.

Therefore, the reactor neutrino experiments should be built deeply underground and have extra muon-veto system to reduce these cosmogenic backgrounds.

In principle, reactor neutrino oscillation experiments can be attributed into the disappearance experiment type, *i.e.*, measuring the disappearance of the electron antineutrino. The survival probability from equation (1-13) with the present three-flavor neutrino mixing matrix of equation (1-15) can be written as

$$\begin{aligned} \text{Prob}(\bar{\nu}_e \rightarrow \bar{\nu}_e) &= 1 - \sin^2 2\theta_{13} \sin^2\left(\Delta m_{ee}^2 \frac{L}{4E}\right) - \cos^4 \theta_{13} \sin^2 2\theta_{12} \sin^2\left(\Delta m_{21}^2 \frac{L}{4E}\right) \\ \sin^2\left(\Delta m_{ee}^2 \frac{L}{4E}\right) &\equiv \cos^2 \theta_{12} \sin^2\left(\Delta m_{31}^2 \frac{L}{4E}\right) + \sin^2 \theta_{12} \sin^2\left(\Delta m_{32}^2 \frac{L}{4E}\right), \end{aligned} \quad (1-19)$$

where Δm_{ee}^2 ^[34] is the effective mass splitting used in the short-baseline reactor neutrino experiments. Since the neutrino mass splittings have $\Delta m_{21}^2 \ll |\Delta m_{31}^2| \approx |\Delta m_{32}^2|$, the second term on the r.h.s. of equation (1-19) is more important in oscillation for a short baseline, while the third term is dominant in oscillation for a long baseline. The effective mass splitting Δm_{ee}^2 is applied in the data analysis of short-baseline reactor experiments to get rid of the mass hierarchy problem. The Fig. 1.1 illustrates the survival probability of equation (1-19) along the baseline L for a generic reactor neutrino spectrum, showing the different impacts of the short-baseline and long-baseline terms. Thus so far, reactor neutrino oscillation experiments are divided into the short-baseline experiments ($L \sim 1$ km, aiming at θ_{13} and Δm_{ee}^2) and the long-baseline experiments ($L \sim 100$ km, sensitive to θ_{12} and Δm_{21}^2). Another new type of medium-baseline ($L \sim 50$ km) reactor neutrino oscillation experiments have been proposed for multiple physics programs, in particular, to determine the unsolved problem of neutrino mass hierarchy. The experiments with very short baseline ($L < 100$ m) are generally designed for the reactor neutrino spectra measurements, not for oscillation.

Short-baseline Reactor Experiments

For short-baseline reactor neutrino experiments, since the mixing angle θ_{13} is too close to 0, the small neutrino flux deficit caused by neutrino oscillation is very difficult to measure with big statistical fluctuation, as well as the big uncertainties from reactor flux and detector. Two measurements by the Chooz experiment^[29] in France and Palo Verde experiment^[35] in USA in the 1990s showed no evidence for antineutrino disappearance and gave only a very weak constraint on θ_{13} as $\sin^2 2\theta_{13} < 0.17$ at the confidence level of

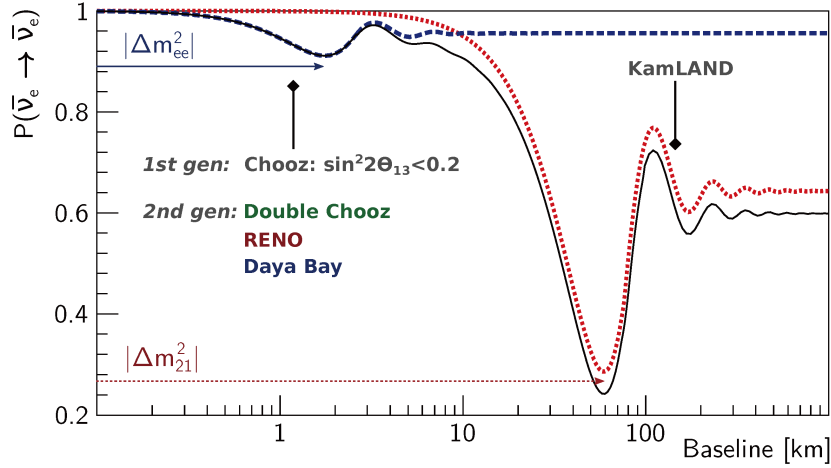


Figure 1.2 The reactor electron antineutrino survival probability vs baseline. The black line is for the total survival probability in equation(1-19); the blue dashed line is for the short-baseline term; the red dashed line is for the long-baseline term. The survival probability is calculated with a generic reactor neutrino spectrum. The figure also shows the approximate baselines for the already built short-baseline reactor neutrino experiments (the first generation of Chooz and the second generation of Double Chooz, RENO and Daya Bay) and long-baseline experiment (KamLAND). Figure by Sören Jetter of the Daya Bay collaboration.

90%. They both employed a single detector of Gd-loaded liquid scintillator, with baseline about 1 km for Chooz and 800 m for Palo Verde.

In 2000, Mikaelyan and Sinev came up with the proposal of a near-far relative measurement of reactor antineutrino disappearance with two functionally identical detectors^[36], summarized in equation (1-20).

$$\frac{N_{\text{far}}}{N_{\text{near}}} = \left(\frac{N_{\text{p, far}}}{N_{\text{p, near}}} \right) \left(\frac{L_{\text{far}}}{L_{\text{near}}} \right)^2 \left(\frac{\epsilon_{\text{far}}}{\epsilon_{\text{near}}} \right) \left[\frac{P_{\text{sur}}(E_{\nu}, L_{\text{far}})}{P_{\text{sur}}(E_{\nu}, L_{\text{near}})} \right], \quad (1-20)$$

where N_p is the target proton number for IBD reaction, L is the baseline, ϵ is the detector efficiency, and $P_{\text{sur}}(E_{\nu}, L)$ is the survival probability depending on neutrino energy and baseline. The reactor flux is absent in the equation (1-20) since they are canceled in the calculation for detected neutrino events for near and far detectors. Therefore, this relative measurement can get rid of the big reactor flux uncertainty. As the two detectors are designed identically, the variation of relative target proton number N_p and detector efficiency ϵ can be highly reduced. Together with other conditions to reduce the backgrounds, it seems possible to reveal the very small mixing angle of θ_{13} by measuring the reactor antineutrino disappearance.

Under this suggestion, the new generation of reactor neutrino oscillation experiments

have been built in the first decade after 2000. They are the Double Chooz experiment in France, the RENO experiment in South Korea and the Daya Bay experiment in China. All of these three experiments have very similar nested three-layer structure of coaxial cylinders for the antineutrino detector (AD). The most inside vessel is filled with Gd-loaded liquid scintillator as the fiducial volume, which is surrounded by the middle layer of Gd-free liquid scintillator as the “ γ -catcher”. The most outside is the buffer layer of mineral oil, surrounded by the PMTs to collect the optical photons from scintillation. All the antineutrino detectors are immersed in highly purified water as a muon veto system. Besides, they all have very good shield from the cosmic rays with thick rock overburden. The RENO and Daya Bay (with six ADs) experiments started data taking for both near and far sites in 2011. The Daya Bay experiment finished the whole 8-AD configuration after installing the last two ADs in 2012 summer. Double Chooz firstly had only the far detector in operation, and its near detector was completed latter in 2014. The profiles of the three experiments are illustrated in the Fig. 1.3, showing the information of reactor cores and powers, detectors numbers and weights, baselines, and the overburden. Soon after the T2K experiment measurement ($\nu_\mu \rightarrow \nu_e$ appearance channel) in 2011^[37] and the Double Chooz far detector measurement in early 2012^[38] showed the hints of a non-zero θ_{13} , the Daya Bay experiment successfully discovered this last unknown mixing angle θ_{13} at a confidence level of 5.2σ in 2012 for the first time^[24]. Later in the same year, the non-zero θ_{13} was confirmed by the RENO experiment with a significance of 4.9σ ^[39]. With more cumulated data sample and additional spectral analysis to the initial rate-only analysis, the precision of $\sin^2 2\theta_{13}$ measurement has been improved to an unparalleled level of $\sin^2 2\theta_{13} = 0.0841 \pm 0.0027(\text{stat.}) \pm 0.0019(\text{syst.})$ by the most recent measurement of the Daya Bay experiment^[40], combined with a precise measurement of $\Delta m_{32}^2 = (2.45 \pm 0.06(\text{stat.}) \pm 0.06(\text{syst.})) \times 10^{-3} \text{eV}^2$ for the normal neutrino mass hierarchy, comparable and consistent with the results obtained by atmospheric neutrino oscillation experiments and accelerator neutrino experiments. This measurement is illustrated in Fig. 1.3, where the observed deficit and spectral distortion of positron spectrum from IBD events have very good agreements with the present three-flavor neutrino oscillation prediction, and the survival probability $\nu_s L/E$ is consistent with the oscillation prediction as well.

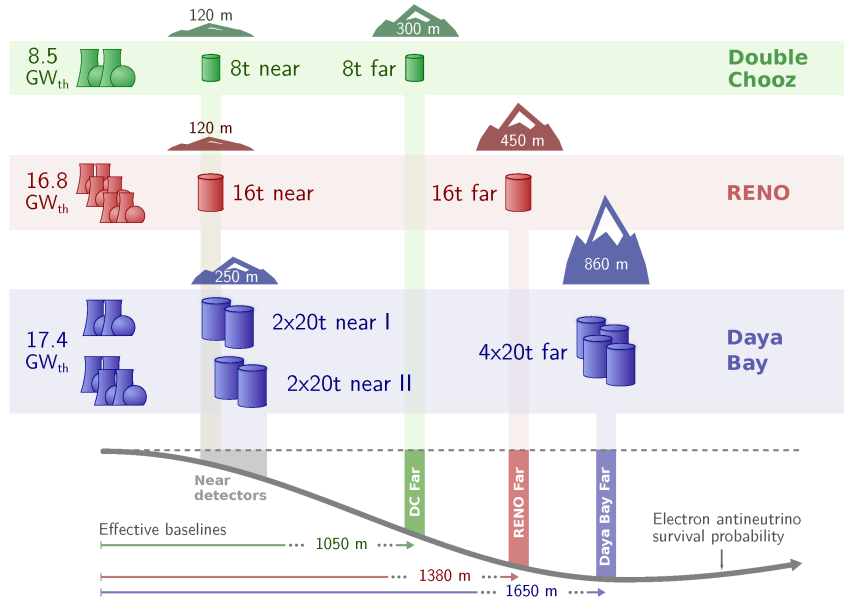


Figure 1.3 The profiles of the three new-generation reactor neutrino oscillation experiments: Double Chooz, RENO, and Daya Bay. The most left side shows the number of reactor cores and total thermal power. The cylinders in the middle are the antineutrino detectors, labeled with their weights and near/far positions. The mountain symbols represents the meter water equivalent (m.w.e.) overburden. On the bottom is the survival probability along the baseline. Figure by Sören Jetter of the Daya Bay collaboration.

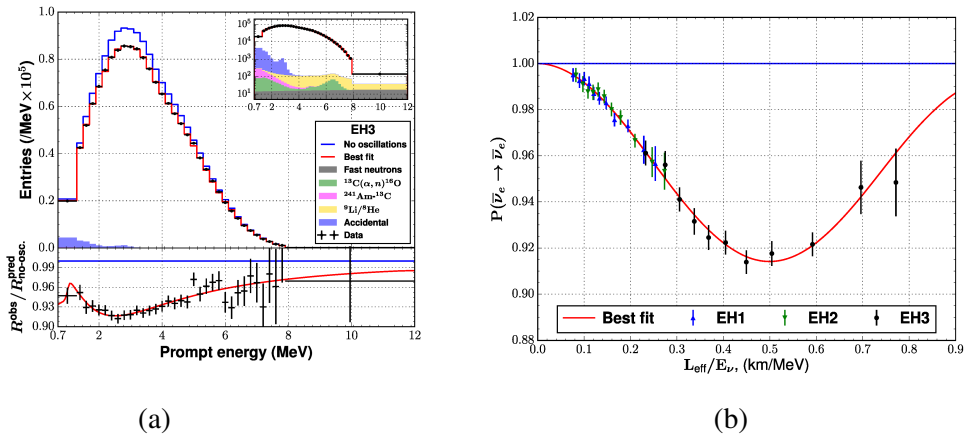


Figure 1.4 Left: the top panel shows the observed positron energy spectrum of IBD events from Daya Bay far detectors (black dots), compared with the non-oscillation prediction (blue line) and the best-fit prediction with oscillation (red line); in the small panel is the spectra in log scale to see the backgrounds clearly; the bottom panel shows the ratio of observed spectrum to the non-oscillation prediction, with clear deficit and spectral distortion. Right: the survival probability vs $L_{\text{eff}}/\langle E_\nu \rangle$ measured by Daya Bay detectors, where L_{eff} is the effective baseline from 6 reactor cores to 8 ADs and $\langle E_\nu \rangle$ is the mean energy. Figures from reference^[40].

1.3 Sterile Neutrinos and Neutrino Anomalies

When we introduced the mixing between neutrino flavor eigenstates and mass eigenstates for the neutrino oscillation in Section 1.2.1, we have mentioned that the precision electroweak measurements of the Z-boson resonance^[20] concluded that only three light flavor neutrinos are coupled to Z while there can be more than three mass eigenstates if there are sterile neutrinos. A sterile neutrino is a hypothetical neutrino not participating in the weak interactions and is beyond the Standard Model (BSM). The existence of one or more sterile neutrino(s) is introduced to address both the theoretical and the experimental issues. The sterile neutrinos of great research interests can be categorized by the mass scale as:

- (1) beyond TeV scale: it is introduced by many theories beyond the Standard Model, such as the see-saw mechanism^[41,42] to explain the question of very tiny neutrino masses;
- (2) GeV to TeV scale: this sterile neutrino can be searched at the large hadron collider (LHC)^[43], though no popular theoretical models or evidences in experiment strongly support its existence;
- (3) keV scale: it is introduced as a possible candidate of dark matter^[44];
- (4) eV scale: this type of sterile neutrino, usually called as the light sterile neutrino, is motivated by the anomalous deficits/excess observed in many experimental measurements. It can provide additional oscillation mode to the general three-flavor neutrino oscillation.

The possible discovery of light sterile neutrinos in experiments has crucial implications for the future researches in the field of particle and nuclear physics. The knowledge of all the neutrinos participating in oscillations is essential for the interpretation of the long-baseline accelerator experiments. Additional sterile neutrino will make the future measurements of leptonic CP-violation by accelerator neutrinos more complicated^[45]. Moreover, the existence of a light sterile neutrino will change the accessible parameter space for the neutrinoless double beta decay ($\beta\beta 0\nu$) experiments^[46,47] to investigate the question of Dirac or Majorana neutrinos.

At present, many anomalous neutrino phenomena mismatching the current theory predictions have been observed in the short-baseline accelerator neutrino experiments, Gallium-based solar neutrino experiments and also the short-baseline reactor neutrino experiments, all indicating existence of extra oscillation mode beyond present model at

short baseline.

1.3.1 Accelerator Neutrino Anomaly

The Liquid Scintillator Neutrino Detector (LSND) experiment was an appearance experiment to measure the $\bar{\nu}_\mu \rightarrow \bar{\nu}_e$ neutrino oscillation at a short baseline about 30 m with average beam energy about 30 MeV^[48]. The $\bar{\nu}_\mu$ beam was produced by the μ^+ decay $\mu^+ \rightarrow e^+ \nu_e \bar{\nu}_\mu$ at rest. Appeared electron antineutrinos from oscillation were detected by inverse beta decay in the liquid scintillator. A total excess of $87.9 \pm 22.4 \pm 6.0$ events were observed mainly due to the oscillation, as shown in Fig. 1.5. Roughly a 3.8σ excess of $\bar{\nu}_e$ was observed^[49], and the allowed region for the sterile neutrino is shown in Fig. 1.7.

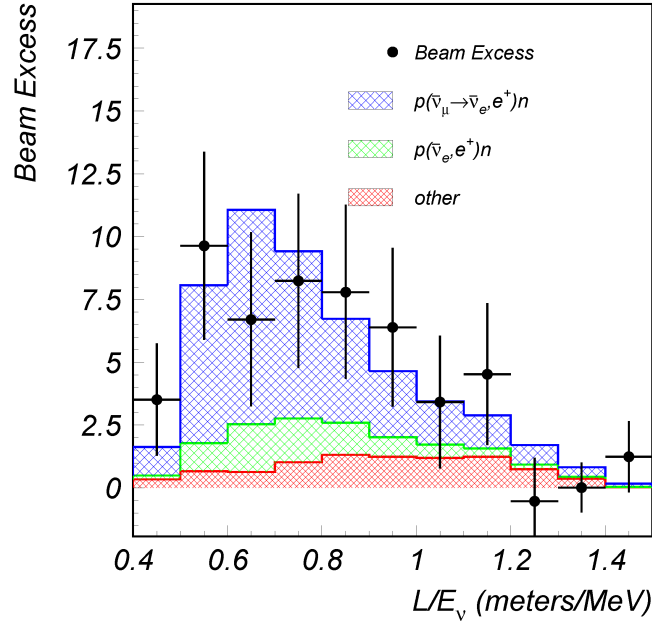


Figure 1.5 The measured L/E distribution for the electron antineutrinos in LSND. The excess higher than the expectation in the small L/E region may come from sterile neutrino oscillation at 1 eV mass scale. Figure from reference^[49].

The MiniBooNE experiment was designed to test the LSND result at a longer baseline of 541 m. Using the magnetic horn to select the polarity, transitions in both the neutrino mode ($\nu_\mu \rightarrow \nu_e$) and the antineutrino mode ($\bar{\nu}_\mu \rightarrow \bar{\nu}_e$) were able to be observed in the neutrino energy between 200 MeV and 1250 MeV, with the L/E configuration similar to LSND. Electron neutrinos were identified by the events from charged-current quasi-elastic (CCQE) interaction with neutron ($\nu_e n \rightarrow e^- p$) while electron antineutrinos were identified by the inverse beta decay (also CCQE). MiniBooNE observed the excess of

$78.4 \pm 8.5 \nu_e$ events and $162.0 \pm 47.8 \bar{\nu}_e$ events in the CCQE energy region of 200-1250 MeV respectively, as shown in Fig. 1.6. More excess of events observed in the low energy region hinted extra oscillation mode due to the sterile neutrino, supporting the interpretation of sterile neutrino oscillation in LSND. The allowed region for the extra oscillation parameters are shown in Fig. 1.7.

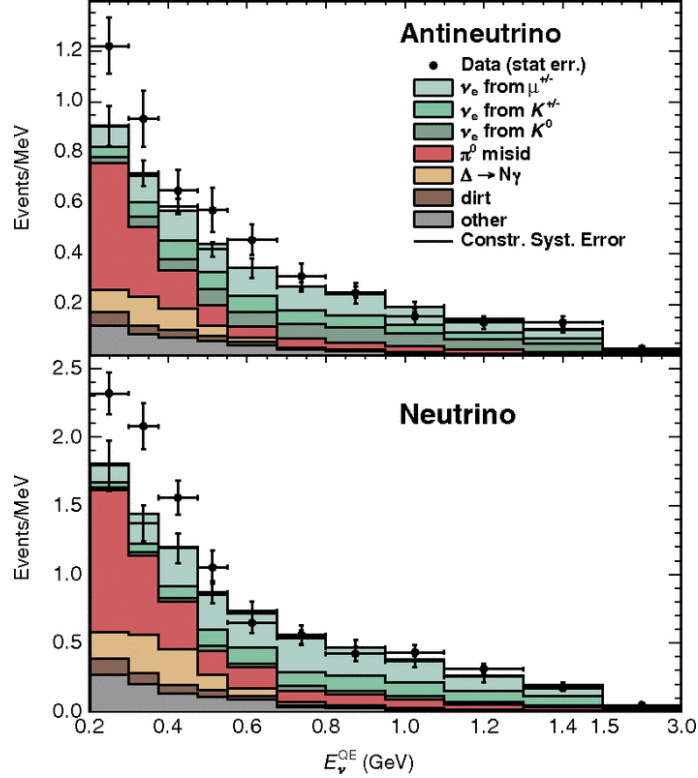


Figure 1.6 The antineutrino mode (top panel) and neutrino mode (bottom panel) neutrino energy spectra for CCQE data and backgrounds. Figure from reference^[50].

However, this anomalous excess in the $\nu_\mu \rightarrow \nu_e$ and $\bar{\nu}_\mu \rightarrow \bar{\nu}_e$ oscillations did not appear in the following measurements of the other accelerator neutrino experiments, including KARMEN^[51], ICARUS^[52], and NOMAD^[53]. The excluded regions for each experiments are shown in Fig. 1.7 as well. The accelerator neutrino anomaly still needs more investigations with future experiments.

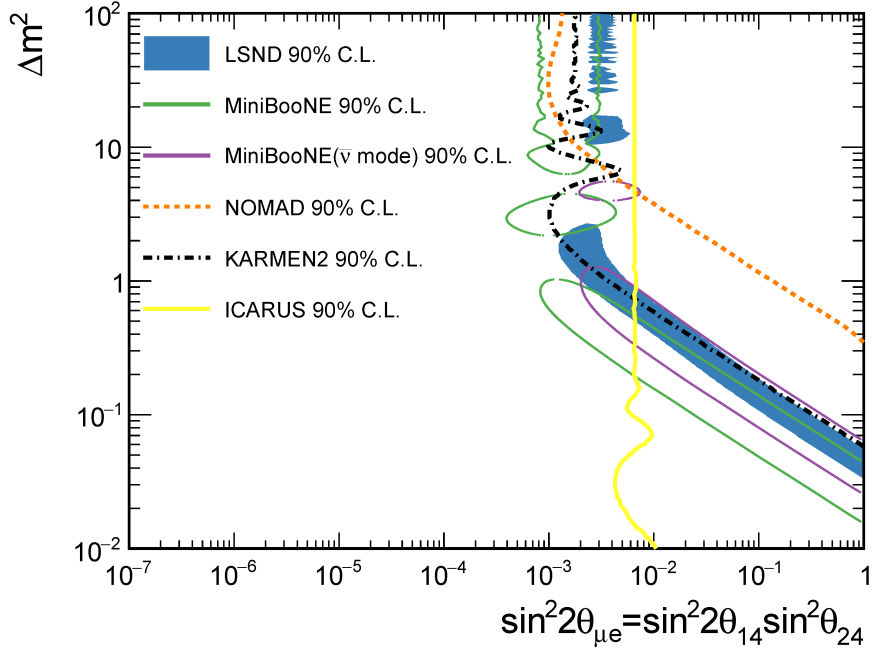
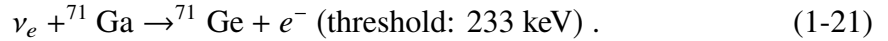


Figure 1.7 The allowed regions for the parameters of the anomaly oscillation with sterile neutrino observed by LSND^[49] and MiniBooNE^[50]. The excluded regions (right side of the lines) are plotted as well for the experiments of KARMEN^[51], ICARUS^[52], and NOMAD^[53]. The x axis is $\sin^2 2\theta_{14} \sin^2 \theta_{24}$ for the extra mixing angles. The y axis is approximately the extra mass splitting of Δm_{41}^2 . Figure from reference^[54].

1.3.2 Gallium Anomaly

The deficit of measured neutrino flux with respect to the prediction in the Gallium-based solar neutrino experiments is also called as the Gallium anomaly. The two experiments of SAGE^[55] and GALLEX^[56] measured the solar neutrinos with gallium via the charged current interaction of



They employed the intense artificial radioactive sources of ${}^{51}\text{Cr}$ and ${}^{37}\text{Ar}$ to conduct the neutrino calibration, with electron neutrinos produced by the electron capture reactions of the nuclei as



With a combined analysis of four data-sets from the two experiments, the average

ratio of the measured to predicted flux was determined to be $R = 0.84 \pm 0.05$ ^[57], as shown in Fig. 1.8. Considering the geometry lengths of the two detectors ($L_{\text{GALLEX}} = 1.9$ m, $L_{\text{SAGE}} = 0.6$ m), a sterile neutrino with mass ~ 0.5 MeV was favored to cause such a deficit^[58]. Even after some corrections in the cross-section calculation for the predictions, the deficit was reduced as $R = 0.90 \pm 0.05$, leaving the anomaly about 1.8σ ^[59].

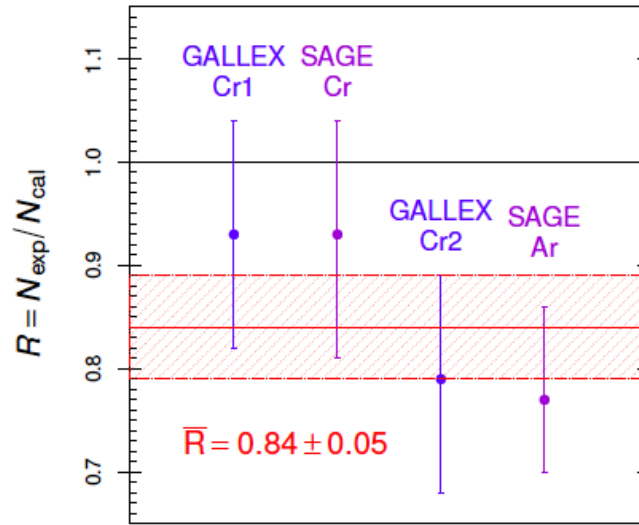


Figure 1.8 The ratios of measured neutrino rates from the radioactive sources to the prediction, in the two gallium experiments.

1.3.3 Reactor Antineutrino Anomaly

The so-called reactor antineutrino anomaly is the discrepancies in the reactor antineutrino flux and spectrum between the experimental measurements and the theoretical model prediction even after the correction with three-flavor neutrino oscillations^[60,61]. The reactor antineutrino flux model will be introduced firstly.

1.3.3.1 Reactor Antineutrino Flux Models

Since the 1950s, the nuclear physicists have attempted to model the antineutrino flux produced by the reactors and make accurate predictions^[62]. These predictions are vitally important for various fields, from nuclear applications to neutrino physics. As introduced in the Section 1.2.2.1, generally the reactor antineutrinos are produced primarily by the beta decays of the fission fragments from the four fissionable isotopes of ^{235}U , ^{238}U , ^{239}Pu ,

and ^{241}Pu , with the total antineutrino flux $S(E)$ as the sum of contribution from each isotope as

$$S(E) = \frac{W_{\text{th}}}{\sum_i f_i E_i} \sum_{i=^{235}\text{U}, ^{238}\text{U}, ^{239}\text{Pu}, ^{241}\text{Pu}} f_i S_i(E), \quad (1-23)$$

where i loops for the four isotopes, W_{th} is the thermal power of the reactor, E_i is the energy released per fission for the i -th isotope on average, f_i is the fission fraction with a sum to unity ($\sum_i f_i = 1$), and $S_i(E)$ is the antineutrino flux produced by the i -th isotope.

Despite the complicated decay chains of the fissionable isotopes (more than 1,000 daughter isotopes with more than 6,000 decay branches), the reactor antineutrino spectra had been determined preliminarily in the 1980s. The antineutrino spectra from ^{235}U , ^{239}Pu and ^{241}Pu were determined by several measurements of β spectra at the Institut Laue-Langevin (ILL) reactor, conducted by Schreckenbach *et al.*^[63–65]. As ^{238}U is a fertile isotope whose fission is induced only by the fast neutron, the antineutrino spectrum of ^{238}U is not easy (at least at that time) to be directly measured at a reactor; instead, it was calculated by P. Vogel *et al.* in 1981^[66]. Combined together, this set of the antineutrino flux from all the four primary isotopes was called as the ILL-Vogel model. The prediction of the ILL-Vogel model was validated by the measurement result at Bugey-3^[67] within 5-10% in 1996, as shown in Fig. 1.9.

Along with the improving precision of experimental measurements for reactor antineutrino flux, a more precise theoretical flux model is imperative for the present and future researches, to probe the nuclear physics and to investigate physics beyond the standard model related to neutrinos. Historically, two alternative approaches are adopted to calculate the reactor antineutrino spectra $S_i(E)$: the *ab initio* summation and the β spectrum conversion methods^[30,68]. Generally, the conversion method is considered to have a more precise prediction.

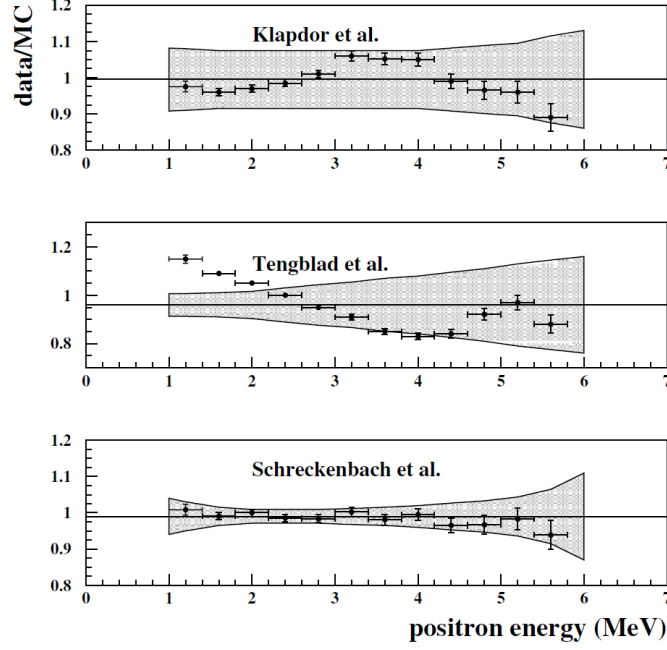


Figure 1.9 Ratio of the Bugey-3 antineutrino spectrum measurement with respect to the predictions from three models. The ILL-Vogel model (labeled as Schreckenbach *et al.*) is most consistent with the measurement, within 5-10%. Figure from reference^[29,67].

ab initio Summation Method

In the *ab initio* method, the antineutrino spectrum for each fissionable isotope is obtained by the summation of the spectra from all the beta decay branches of all fission fragments as

$$\frac{dN}{dE_{\bar{\nu}}} = \sum_n Y_n(Z, A, t) \sum_i b_{n,i}(E_0^i) P_{\bar{\nu}}(E_{\bar{\nu}}, E_0^i, Z), \quad (1-24)$$

where i is one beta decay branch of the fission fragment n with nucleus composition as (Z, A) , $Y_n(Z, A, t)$ is the fission yield for the fission fragment n (the number of the beta decays from the fragment, depending on time t , and independent of time if in the equilibrium state), E_0^i is the endpoint energy of β spectrum (maximal electron energy) for each decay branch, $b_{n,i}(E_0^i)$ is the i -th branch ratio with all branch ratios summation to unit as $\sum_i b_{n,i}(E_0^i) = 1$, $P_{\bar{\nu}}(E_{\bar{\nu}}, E_0^i, Z)$ is the normalized antineutrino spectrum for the branch. To calculate the antineutrino spectrum $P_{\bar{\nu}}(E_{\bar{\nu}}, E_0^i, Z)$, the β spectrum $S_{\beta}(E_{\beta}, E_0^i, Z)$ is calculated firstly with a connection to the antineutrino energy by the endpoint energy as

$$E_{\bar{\nu}} = E_0^i - E_{\beta}. \quad (1-25)$$

Based on the well-established beta decay theory, the β spectrum is provided by

$$S_{\beta}(E_{\beta}, E_0^i, Z) = p_{\beta} E_{\beta} (E_0^i - E_{\beta})^2 F(E_{\beta}, Z) C(E_{\beta}, Z) (1 + \delta_{\text{FS}} + \delta_{\text{WM}} + \delta_{\text{rad}} + \delta_{\text{recoil}}), \quad (1-26)$$

where $p_{\beta} E_{\beta} (E_0^i - E_{\beta})^2$ is the phase space factor, $F(E_{\beta}, Z)$ is the Fermi function with the correction for the effect of the electron in the Coulomb field of the daughter nucleus, the shape factor $C(E_{\beta}, Z)$ is the energy dependent correction for the so-called “forbidden transitions” which requires more complicated theoretical treatment than the allowed transitions. For the allowed decays, $C(E_{\beta}, Z) = 1$. The last term $(1 + \delta_{\text{FS}} + \delta_{\text{WM}} + \delta_{\text{QED}} + \delta_{\text{recoil}})$ in Equation (1-26) are the four leading order corrections^[68].

- (1) δ_{FS} is the “finite size” correction that accounts for the non-point-like charge distribution in the calculation of the Fermi function;
- (2) δ_{WM} is the “weak magnetism” correction due to the interaction between the electron and the magnetic momentum of the daughter nucleus;
- (3) δ_{QED} is the “QED radiation” correction for the QED radiation of photons emitted by the charged fermions,
- (4) δ_{recoil} is the “recoil energy” correction as the daughter nucleus does have a small kinetic energy.

The weakness of this *ab initio* summation method is the incomplete information of the fission yields Y_n and the branching ratios $b_{n,i}$ from so many fission fragments and branches. Even in the state-of-art nuclear databases, *e.g.*, JEFF-3.1^[69] and ENDF/B-VII.1^[70], these information for many of the fission fragments have big uncertainties. For the antineutrino energy range of interest above 1.8 MeV in the reactor neutrino detection, the predictions calculated with the two nuclear databases are consistent within 6%^[71]. However, about 5% of the unstable nuclei in the fission fragments are still lack of experimental data. As a result, the antineutrino spectrum calculated by this method is of limited precision^[32,72], but in some cases, such as ²³⁸U, it is the only available way.

Electron Spectrum Conversion Method

The alternative method of electron spectrum conversion uses the measurement of integral electron spectrum from all fission fragments associated with each fission isotope, and subsequently converts it to the corresponding antineutrino energy spectrum. The electron spectra from ²³⁵U, ²³⁹Pu and ²⁴¹Pu were measured at the ILL reactor in the 1980s^[63–65], while the electron spectrum from ²³⁸U was not available at that time because

the fission of ^{238}U is only induced by the fast neutron, leading to difficulty in the measurement. It was until 2014 that the electron spectrum from ^{238}U got measured with improved neutron source at the research reactor FRM II in Germany^[73]. This may lead to a new prediction of antineutrino spectrum of ^{238}U via the electron spectrum conversion method in the future.

To obtain the antineutrino spectrum, the total integral electron spectrum was fitted with 30 (or more) hypothesized (virtual) beta decay branches,

$$\frac{dN}{dE_e} = \sum_{i=1}^{30} a_i S^i(E, E_0^i, Z), \quad (1-27)$$

where the coefficients a_i 's and the virtual beta decay endpoint energies E_0^i are free parameters. The virtual beta decay branches are treated the same as real decays, and the electron spectrum $S^i(E, E_0^i, Z)$ has the same meaning as in equation (1-26) with the corrections applied as well. The virtual nucleus charge in each virtual beta decay branch is modeled by a quadratic polynomial function of the free parameter E_0^i effectively as $Z_{\text{eff}} = a + bE_0^i + c(E_0^i)^2$. After the electron spectrum for each virtual branch is obtained by the fit, the corresponding antineutrino spectrum can be calculated by the constraint of equation (1-25), and subsequently summation of all virtual branches leads to the total antineutrino spectrum for the given fissionable isotope.

Compared with the *ab initio* summation method, the conversion method is less dependent on the detailed information of the fission yields and branching ratios, and thus largely avoids the systematic uncertainties from the unknown fission fragments in the nuclear databases. However, this does not mean that the conversion method is entirely free from uncertainties related to the nuclear structure. As pointed out by the reference^[74], the forbidden decays can significantly affect the antineutrino spectrum predictions. The ILL-Vogel model, which has been introduced in Section 1.3.3.1, was considered as the gold standard for the reactor antineutrino spectrum prediction, until 2011. In that year, Mueller *et al.*^[32] revisited the previous results in the attempt to reduce the uncertainties, in the preparation for the Double Chooz experiment. With the new calculation, the prediction of antineutrino flux had a upward shift of approximately 3% while the uncertainty was not largely reduced unexpectedly. The upward shift of 3% in antineutrino flux was confirmed by the work of Huber^[31] in the same year. The combination of these new calculations were called as the Huber-Mueller model. The prediction shift was mainly

due to the improvements in the theoretical treatments: the δ_{FS} and δ_{WM} correction in the beta decay theory (mentioned in equation (1-26)), and the modeling of nucleus charge distribution $Z_{\text{eff}}(E)$ for the virtual beta decays. The uncertainty of the Huber-Mueller model is mainly contributed from the uncertainty in the corrections of δ_{FS} and δ_{WM} , leading to an uncertainty in the reactor antineutrino flux approximately 2.4%.

Together with the flux corrections from the non-equilibrium effect (arising from the relative long-lifetime fission fragments) and the updated IBD cross-section with new value of the neutron lifetime^[75], the upward shift of 3% in the new prediction of antineutrino flux resulted in a deficit of about 6% for detected antineutrino number via IBD reactions by the previous reactor neutrino experiments, which used to be somehow consistent with the ILL-Vogel model prediction (see Fig. 1.9). This is the so-called “reactor antineutrino anomaly” and it was first discussed in the reference^[60].

1.3.3.2 Reactor Flux Anomaly

Despite that the neutrino rate deficit and spectral distortion observed in the near-far relative measurement of the new-generation short-baseline reactor neutrino experiments (Double Chooz, RENO, and Daya Bay) are successfully interpreted in the framework of three-flavor neutrino oscillation, as shown in Fig. 1.4(a), the new-generation reactor neutrino experiments have also observed a deficit in the overall absolute neutrino flux at the near detectors with respect to the prediction by the Huber-Mueller model even after the three-flavor neutrino oscillation correction^[76-78]. This deficit is not unique for the new-generation experiments; on the contrary, it has been observed by most of the previous short-baseline ($L \sim 1$ km) and very-short-baseline ($L < 100$ m) reactor neutrino experiments conducted over the past three decades at different distances, as shown in Fig. 1.10.

At present, a global fit with all past reactor neutrino experiments before the Daya Bay experiment gets the ratio of the measured reactor antineutrino flux to the Huber-Mueller model prediction as $R_g = 0.942 \pm 0.009(\text{exp.}) \pm 0.023(\text{theo.})$ ^[76], while the ratio from Daya Bay is $R = 0.946 \pm 0.020(\text{exp.})$ ^[76], with the three-flavor neutrino oscillation correction. The experimental uncertainty in the global best fit has been determined to be less than 1%, significantly smaller than the model uncertainty (2.4%). Moreover, this common deficit may be caused by the incorrect reactor antineutrino flux prediction. To address the reactor flux anomaly, it has been suggested that the electron spectrum conversion

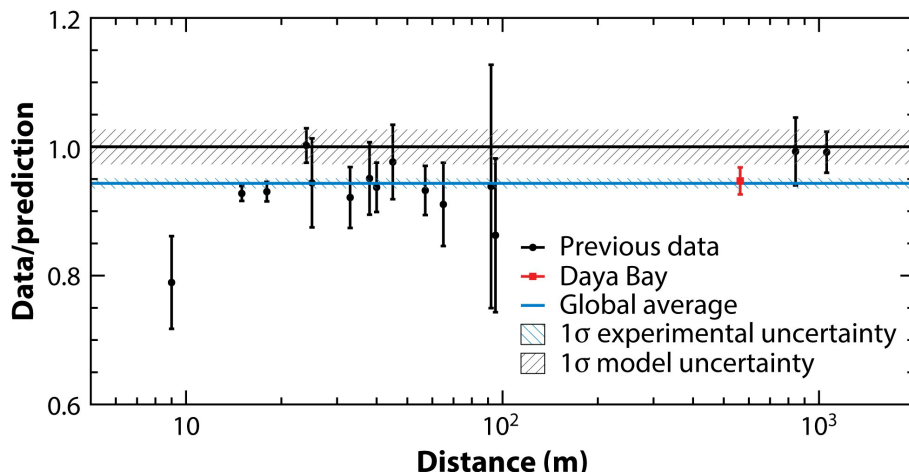


Figure 1.10 The measurements of the reactor flux at different baselines from the previous reactor neutrino experiments (black points), normalized to the prediction of the Huber-Mueller model^[31,32]; the red point is the new measurement by Daya Bay near detectors. All the points have been corrected by the three-flavor neutrino oscillations. A common deficit is observed by most of the measurements with respect to the model prediction. Figure from reference^[76].

predictions and their uncertainty estimations need more corrections. The type of nuclear decays (forbidden vs. allowed) can lead to significant variations in the antineutrino flux and spectrum^[74]. In the forbidden decays, the antineutrino spectrum depends on details of the underlying nuclear structure, for which generally the information at this level of detail is not available at present. At the same time, because of the big uncertainty arising from the limit of incomplete nuclear database, the huge number of contributing beta decay branches and highly uncertain fission yields, the *ab initio* calculation method is unlikely to be able to address the reactor flux anomaly conclusively. Besides the possible incorrect model prediction, the reactor flux anomaly may come from the existence of one (or more) light sterile neutrino with eV-scale mass, providing extra oscillation mode for the short baselines. Probing the sterile neutrino in the reactor antineutrino study is important as a discovery of sterile neutrinos will be the first-ever direct detection of a new particle beyond the Standard Model and require a fundamental extension in theory to explain this new state of matter.

1.3.3.3 Reactor Spectrum Anomaly

In addition to the reactor flux anomaly, recent antineutrino spectrum measurements of the reactor neutrino experiments of Daya Bay, Double Chooz, and RENO have also uncovered an intriguing spectral anomaly^[76,79,80]. An excess of events in the form of

a spectral distortion (or called as “bump”) have been detected in the 4-6 MeV reconstructed energy for the positron signals in the IBD reactions with respect to predictions, corresponding to a bump in the 5-7 MeV region for the unfolded antineutrino spectrum. Fig. 1.11 shows the positron spectrum from IBD reactions measured in Daya Bay, in which the statistical significance for the excess to mismatch with the prediction of Huber-Mueller model is 4.4σ in 4-6 MeV region and 2σ for the full energy range. The bump is unlikely

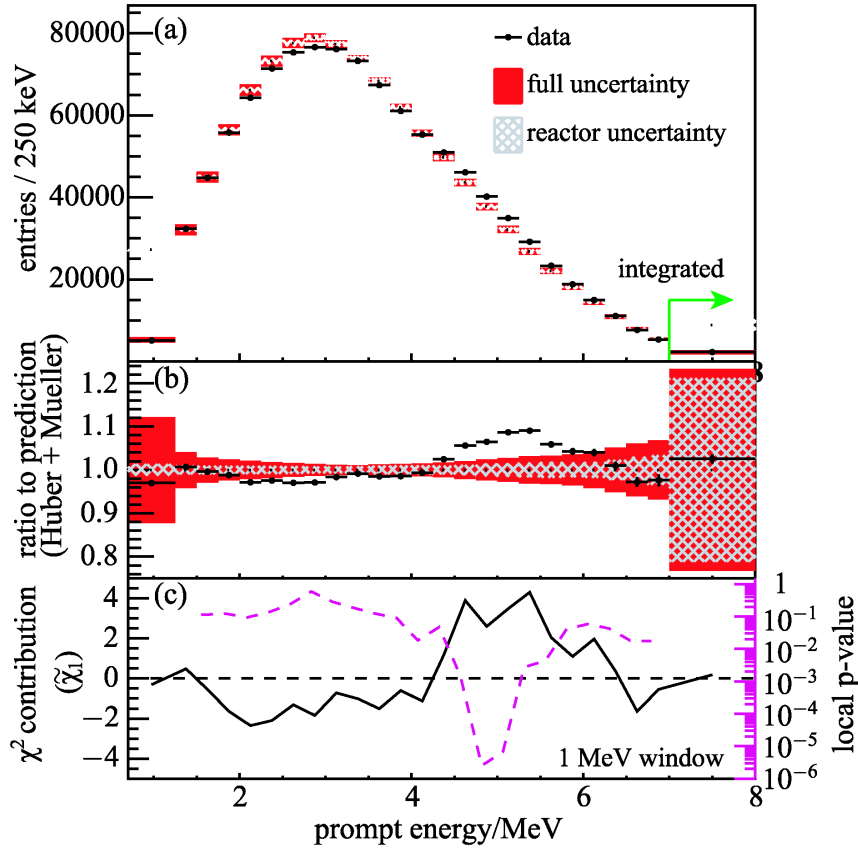


Figure 1.11 Top: The measured positron spectrum from the IBD reaction in Daya Bay, overlaid with the normalized spectrum from to the prediction of the Huber-Mueller model. The normalization is due to flux deficit of reactor antineutrino anomaly. Middle: The ratio of measurement to prediction, showing a bump in 4-5 MeV region. Bottom: the χ^2 (black solid line) and local p -value (magenta dashed line) for 1 MeV energy windows to show the significance of the excess. Figure from reference^[76].

to be an unexpected background since the events within the energy region of the bump have been carefully examined for the energy, space and time information, all found to match the general IBD characteristics.

After the observation of such a bump, many possible origins of it have been pro-

posed^[81], such as the uncertainties of the electron spectrum measurements, the forbidden decays and the beta decay daughters of one or more of the four primary fissionable isotopes. The extra oscillation mode provided by the hypothesis of sterile neutrino can not lead to such a feature in spectrum, thus it is excluded from the causes of the bump. As the Huber-Mueller model is based on the measurements at ILL reactor with thermal neutrons while the new-generation reactor neutrino experiments who observed the bump all use the pressurized water reactor (PWR), the feature may be due to the harder neutron spectrum in PWR than the thermal neutron spectrum in ILL^[61]. Moreover, the work by Dwyer *et al.*^[82] shows that, with the beta decay corrections applied, an *ab initio* calculation method predicts an analogous bump with ENDF database, indicating underlying errors in the ILL reference data. However, the calculation with JEFF data does not have such a feature^[71,81] and after the correction of a mistake in ENDF for fission yields at mass $Z=86$, the bump disappears. Actually this is not that surprising since the size of the bump is very small relative to the uncertainties in the databases. In addition, the forbidden decay can only provide excess up to 1%^[68], thus it is not significant enough to reproduce the current observations of 1.5-2.5%.

The isotopes of ^{239}Pu and ^{241}Pu are disfavored as the single source to cause the bump by the recent work in reference^[83]. The isotope ^{238}U may be one of the origins, since the RENO experiment observed the most significant bump (2.5%) among the three experiments with the highest fission fraction of ^{238}U in the reactors^[68]. However, it is unlikely to address this reactor spectrum anomaly conclusively without additional data from precise reactor experiments. The near future highlights are the very short-baseline reactor neutrino experiments with highly enriched uranium-235 (HEU) fuels, which has very tiny antineutrino yields from ^{238}U and other plutonium isotopes^[84,85].

Chapter 2 The Daya Bay Reactor Neutrino Experiment

The Daya Bay reactor neutrino experiment^[86] was designed to measure the small neutrino mixing angle θ_{13} precisely (sensitivity for $\sin^2 2\theta_{13}$ better than 0.01). Since publishing the first result in 2012 for non-zero θ_{13} at a confidence level of 5.2σ ^[24], Daya Bay experiment has been leading the measurements on θ_{13} and Δm_{32}^2 at state-of-the-art level^[40,87], and a few other physics topics, such as searching the light sterile neutrino in reactor^[88–90], measuring the reactor antineutrino spectrum^[76,91], the IBD yields for the primary fissionable isotopes in reactor fuel^[92], and studying the decoherence effect in the treatment of neutrino wave packets^[93].

I will describe the Daya Bay Experiment in this section, including the experiment site, detector sub-systems, and data taking.

2.1 The Experiment Site

The Daya Bay reactor neutrino experiment is built in the vicinity of the Daya Bay Nuclear Power Station, located in Shenzhen city of southern China. This nuclear power station is among the world's top five most powerful nuclear-power complexes, with totally 17.4 GW thermal power from six reactor cores (two from Daya Bay Nuclear Power Plant, two from Ling Ao NPP phase I, and two from Ling Ao NPP phase II). To measure the abundant antineutrinos from these reactor cores, the Daya Bay experiment employed eight functionally identical antineutrino detectors (ADs) in three experimental halls (one near the Daya Bay NPP, one near the Ling Ao Phase I and Phase II, and one far hall with about the same distance to each reactor core). This near-far hall design with identical detectors was first proposed by Mikaelyan and Sinev^[36], to reduce the uncertainties from reactor flux and detectors and achieve a sub percentage precision, as shown in equation (1-20). Though the situation with multiple reactor cores and multiple detectors at Daya Bay is much more complicated than the initial proposal, the proposal basis of near-far relative measurement remains. Fig. 2.1 gives the layout of the experiment and the reactor cores.

In addition, the baselines were also optimized according to the reactor antineutrino survival probability illustrated in Fig.1.2. Since the baseline is defined as the distance from an AD to a reactor core, each AD should have six different baselines. All of them were derived from the surveyed coordinates determined by a combination of GPS and

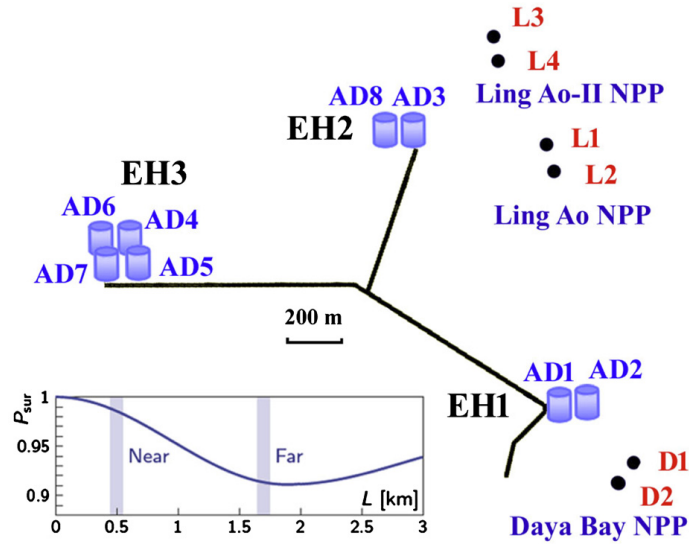


Figure 2.1 Layout of the Daya Bay experiment. The six black dots are for the reactor cores (labeled as D1, D2, and L1 to L4) in three NPPs. The eight blue cylinders correspond to the eight identical ADs (labeled from AD1 to AD8, according to the assembly and installation order), which were installed separately in three halls (referred to as EH1, EH2 and EH3). AD7 and AD8 were installed in 2012 summer. The other ADs were installed in the beginning of data taking. The black lines represent the tunnels connecting the EHs and to the ground. The bottom sub-panel illustrates the survival probability *versus* the effective baseline assuming $\sin^2 2\theta_{13} = 0.1$ [86].

total station electronic theodolite measurements with a precision of 18 mm. Table 2.1 gives the baselines for each AD from the geometric center of each reactor core.

An unique feature of the Daya Bay experiment is that all the experimental halls are situated under a mountain. The overburden in each hall provides a good shielding for the cosmic ray background as demonstrated in Fig. 2.2. The muon-induced spallation neutrons and short-lived isotopes with cascade decays are two of the most prominent backgrounds for the IBD events detection. The overburden in the unit of meter water equivalent, the rate and mean energy of the residual cosmic muons for each experimental hall are summarized in Table 2.2, from which we can see that the muon rates have been greatly reduced to 1 Hz/m² level for the near halls and 0.05 Hz/m² level for the far hall. These rates are much smaller than the general muon flux ~ 167 Hz/m² at sea level.

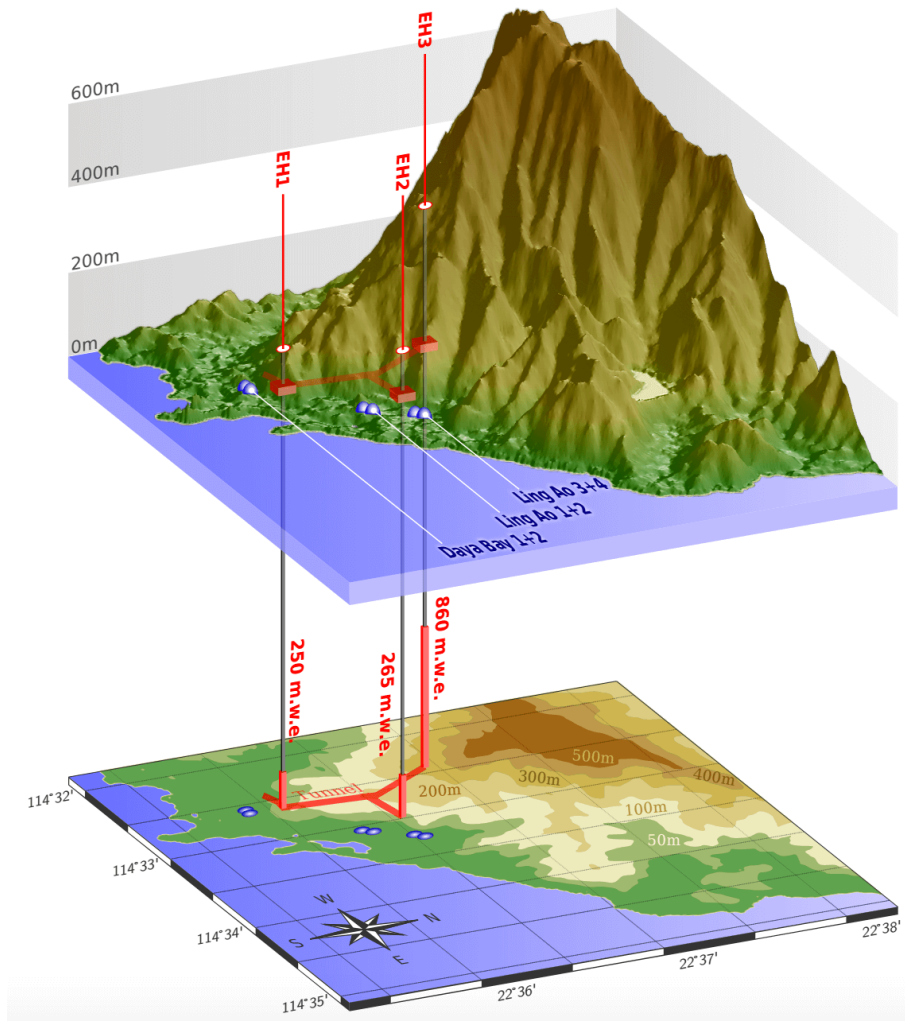


Figure 2.2 The 3D landscape and elevation profile of the Daya Bay experiment, to show the overburden (figure from reference^[94]).

Table 2.1 The mass of the Gd-loaded liquid scintillator (GdLS) antineutrino target for each AD and the baselines from each reactor core (D1, D2, and L1 to L4) to each AD. Table from reference^[40]

Hall	Detector	Target [kg]	Baseline [m]					
			D1	D2	L1	L2	L3	L4
EH1	AD1	19941±3	362.38	371.76	903.47	817.16	1353.62	1265.32
	AD2	19967±3	357.94	368.41	903.35	816.90	1354.23	1265.89
EH2	AD3	19891±4	1332.48	1358.15	467.57	489.58	557.58	499.21
	AD8	19944±5	1337.43	1362.88	472.97	495.35	558.71	501.07
EH3	AD4	19917±4	1919.63	1894.34	1533.18	1533.63	1551.38	1524.94
	AD5	19989±3	1917.52	1891.98	1534.92	1535.03	1554.77	1528.05
	AD6	19892±3	1925.26	1899.86	1538.93	1539.47	1556.34	1530.08
	AD7	19931±3	1923.15	1897.51	1540.67	1540.87	1559.72	1533.18

Table 2.2 The overburden (in unit of meter water equivalent), the rate and mean energy of cosmic muons for each experimental hall.

Hall	Overburden [m.w.e.]	R_μ [Hz/m ²]	\bar{E}_μ [GeV]
EH1	250	1.27	57
EH2	265	0.95	58
EH3	860	0.056	137

2.2 Antineutrino Detector

The antineutrino detectors (ADs) played the key role in the discovery of non-zero θ_{13} . The eight ADs of Daya Bay experiment were designed to be functionally identical, in order to limit the potential variations of the target proton number, the detector response and efficiency among all the ADs. Every modular AD has a nested three-layer structure, held by three coaxial cylindrical tanks, as shown in Fig. 2.3. The three coaxial cylindrical tanks from inside to outside are: the inner acrylic vessel (IAV, size $\Phi 3 \text{ m} \times 3 \text{ m}$), the outer acrylic vessel (OAV, size $\Phi 4 \text{ m} \times 4 \text{ m}$), and the stainless steel vessel (SSV, size $\Phi 5 \text{ m} \times 5 \text{ m}$). The IAV holds 20 tons of Gd-doped liquid scintillator (GdLS) with 0.1% Gd by weight as the target material (detailed weight for all ADs are summarized in Table 2.1). The volume between the IAV and OAV is filled with about 22 tons of undoped liquid scintillator (LS), serving as the “ γ catcher” to detect the γ 's escaping from the target volume. Outside the OAV is 37 tons of mineral oil (MO) held by the SSV, to shield the inner volumes against the natural radiations from the SSV and the photomultiplier tubes (PMTs). Each AD has in total 192 20-cm PMTs (Hamamatsu R5912), mounted around the inner circumference of the SSV by 24 columns \times 8 rings, inside the MO volume. The minimum distance from the PMT photocathode to the OAV surface was optimized in design as 20 cm, to provide a relative uniform detector response. The top and bottom surfaces above and below the OAV are not covered by PMTs; instead, two highly reflective panels were installed separately to redirect the light to PMTs. The two reflectors are made of ESR (Enhanced Specular Reflector, 3M[®]) material with spectral reflectivity $> 98.5\%$. This helps to increase the photocathode coverage by about 12% and reduce the required minimum number of PMTs by 50% without significantly degrading the position or energy resolution^[95].

Besides, there are three automated calibration units (ACUs) on the lid of the SSV. Through the three calibration pipes, they can deploy calibration sources into the AD, to do the calibrations for the energy and position reconstruction. The calibration system will be introduced in detail in Section 2.4.

2.2.1 AD Liquids

The Daya Bay experiment produced in total 185 tons of GdLS and 200 tons of LS, and then piped them into the eight ADs to ensure the uniformity of liquids in all ADs. The LS was produced with linear alkylbenzene (LAB) as the solvent, 2,5-di-

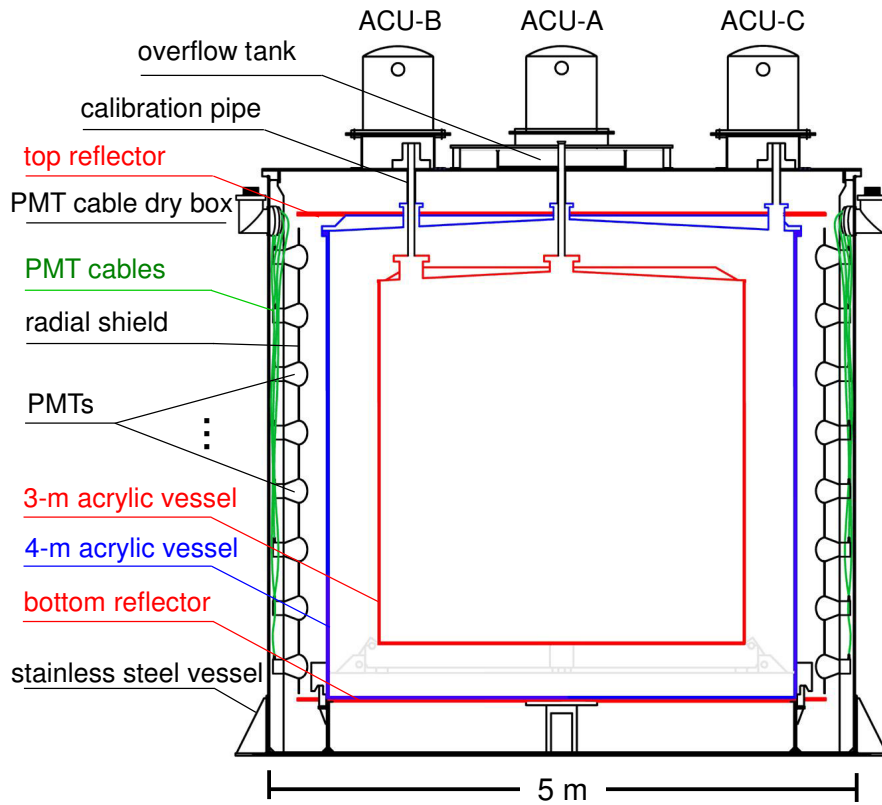


Figure 2.3 Side-view schematic diagram of a modular antineutrino detector at the Daya Bay experiment^[96].

phenyloxazole (PPO, 3g/L) as the fluor, and p-bis-(*o*-methylstyryl)-benzene (bis-MSB, 15mg/L) as the wavelength shifter^[97]. The GdLS is produced based on the same LS with gadolinium doped. Since the salts of gadolinium are difficult to be dissolved into the organic solution of LAB-based scintillator, THMA (3,5,5-tri-methylhexanoic acid) was used as the chelating ligand to complex with gadolinium (in GdCl_3 solution), forming the complex of $\text{Gd}[\text{THMA}]_3$ easily dissolved in LAB. Both the GdLS and LS were strictly purified by the manufacturer to remove the colored contaminants, such as cobalt (Co) and iron (Fe), as they can degrade the optical transparency of the scintillator and also affect the chemical stability. The other contaminants of radioactive daughters from the natural U/Th decay chains were controlled to be < 1 ppb (parts per billion) as well.

2.2.2 Signal Detection

The charged particle propagating in the liquid scintillator can deposit its kinetic energy via ionization and emit the scintillation photons. Generally, a fluor (PPO for Daya Bay) was added into the liquid scintillator base to improve the scintillation efficiency. The

scintillation photons can scatter with the liquid scintillator themselves by the absorption and re-emission processes^[98,99]. Therefore, a second solute of the wavelength shifter (bis-MSB for Daya Bay) was utilized to effectively increase the wavelength of the fluorescence emission spectrum (from ultraviolet to visible), to minimize the self-absorption of liquid scintillator and to have a better spectral acceptance by the PMTs^[100]. Another type of optical photons produced by the charged particles in the liquid scintillator is the Cherenkov radiation^[101], when charged particles travel faster than the phase velocity of light in the medium. Both the scintillation photons and Cherenkov light can be converted into photoelectrons (PEs) when hitting the Photocathode of PMTs via the photoelectric effect with a quantum efficiency. These photoelectrons are then amplified by the strong electric field step-by-step in the PMT, and finally form an electronic pulse. The gain (amplification factor) of Daya Bay PMT (Hamamatsu R5912) can reach 1×10^7 under the high voltage ~ 1600 volts. The PMT readout is then digitalized by the flash ADC (Analog to Digital Converter). The energy and position of the particle were both reconstructed by the ADC counts and hit time information of the fired PMTs. The neutral particles, such as the γ rays and neutrons, can also deposit energy and produce optical photons in the liquid scintillator, by the secondary electrons/positrons or recoiling the protons.

Because of the scintillation quenching effect^[98,99] (very dense ionization within short path leads to reduction of scintillation photons than expected) and Cherenkov radiation, the photoelectrons number N_{PE} is not proportional to the deposited energy E_{dep} , and the scale factor $N_{\text{PE}}/E_{\text{dep}}$ also varies for different kinds of particles. This is referred to as the energy non-linearity effect. Another energy non-linear effect comes from the electronics as the slow component of scintillation photons can exceed the time window for charge read out from a single PMT. The Daya Bay experiment energy non-linearity model will be discussed and formulated in Chapter 3. There is also a so-called energy non-uniformity effect that the energy scale at different positions inside the detector is not uniform, since the PMTs coverage and optical photon attenuation depend on the positions. To have a precise and reliable energy reconstruction for all the events, we need a good calibration system to obtain accurate calibrations for many locations in the detector.

2.3 Muon Veto System

The muon veto system, consisting of a water Cherenkov detector and an array of the resistive plate chamber (RPC) detectors for each experimental hall, was used to reject

the cosmogenic backgrounds induced by the high energy muons, as shown in Fig. 2.4. The water Cherenkov detector can significantly attenuate the ambient radiations from the surrounding rocks by a factor of 10^6 [95] as well.

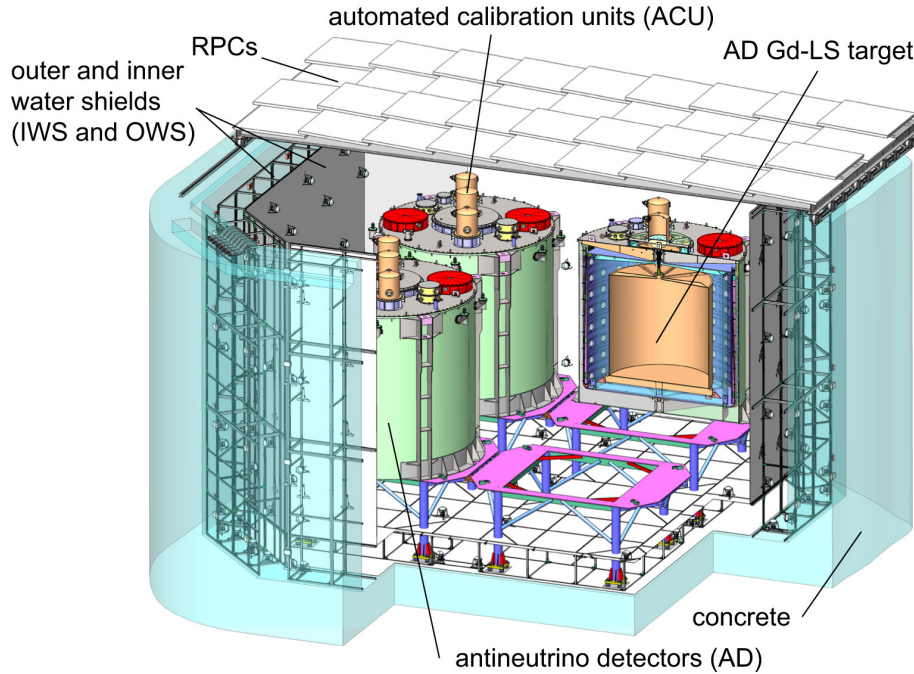


Figure 2.4 The schematic diagram of Daya Bay EH3 ADs and muon veto system. Figure from reference [95].

At each experimental hall, the ADs were submerged in the ultra-pure water pool, which was divided into two regions, the inner water shield (IWS) and outer water shield (OWS), by the White Tyvek[®] sheets and stainless steel frames. The OWS is 1-m thick while the IWS is 1.5-m thick. Both the two regions are equipped with 20-cm PMTs, serving as independent water Cherenkov detectors for the passing through cosmic muons. In total, there are 288 PMTs installed in the water pool in EH1 and EH2 separately, and 384 PMTs for the bigger water pool in EH3 [102]. The highly purified water used in Daya Bay has an attenuation length of 40 m for 420 nm photons, with an electrical resistivity of 18 M Ω -cm and dissolved oxygen < 10 ppb. The biological contaminants are sterilized by passing through the 1 and 0.1 μ m filters and being exposed to ultraviolet at 185 and 254 nm. The measured radon level in the water after polishing is between 30 and 50 Bq/m³. The water temperature is maintained around $22.7 \pm 1^\circ\text{C}$, balancing between the noise rate in PMTs and cost of cooling capacity [102].

The water pool was covered by an array of RPC modules as an additional muon detector. Each tile of RPC module had a size of 2.20 m \times 2.17 m \times 8 cm, consisting of four

layers of RPC made from non-oiled Bakelite sheets^[103,104]. The position resolution of cosmic muon detection was about 10 cm, achieved by eight readout strips installed on each module. The space around the RPC layers inside the module was filled with a gas mixture of Argon, freon (R134a), isobutane and SF₆ in the fraction of 65.5 : 30 : 4 : 0.5^[105].

The muon detection efficiency of the water Cherenkov detectors was designed as 95%, and 90% for the RPCs, with a combined efficiency aiming to be (99.5±0.25)%. After the experiment operation, the muon detection efficiency of IWS was measured to be as good as 99.98 ± 0.01% while that for OWS was greater than 97%^[102]. This muon veto system of multiple detectors provided a reliable tagging for the cosmic muons, helping to reject the backgrounds induced by the muons.

2.4 Automatic Calibration Units

Experiences from previous reactor neutrino experiments of Chooz and Palo Verde showed the degrading of the liquid scintillator properties over time^[36], which would lead to the change of detector response. Though the ADs in Daya Bay experiment were designed to be functionally identical, to measure the mixing angle θ_{13} in a sensitivity better than 0.01 for $\sin^2 2\theta_{13}$, it is needed to understand the AD performance differences and to identify the change of a particular modular AD over time both at the 0.1% level^[106]. This requires a detailed characterization of the AD response and frequent monitoring of all the AD performances, which can only be achieved by the complete and regular calibrations of the ADs. The detector calibration mainly includes two aspects: the PMT gain calibration (scale of PMT readout after ADC convention to the initial PE number) and the energy scale calibration (the energy scale of true energy to PE number, the energy non-linearity, and the energy non-uniformity). The PMT gain can be obtained by the study of the single photoelectron (SPE) pulses offered by a low-intensity LED (light-emitting diode) or the dark noise by PMT itself. The energy calibration can only be done by deploying proper radioactive sources into the AD at multiple typical positions.

These requirements guided the design and construction of the calibration system in Daya Bay experiment^[107], which consisted of three automated calibration units (ACUs, labeled as ACU-A/B/C separately) for every AD module. The ACUs were installed on the lid of the SSV in the top part of the AD, and each ACU was an independent and complete robotic system, which was able to deploy the calibration source through the calibration pipe into the AD along a given vertical axis with a precision of 7 mm, as shown in Fig. 2.6.

The vertical axis for ACU-A was at the AD center ($R = 0$ mm), while that for ACU-B was close to the boundary of GdLS volume ($R = 1350$ mm, measured from AD central axis) and that for ACU-C was in the LS volume ($R = 1772.5$ mm). Each ACU was enclosed in a stainless steel bell jar, to protect it when the ADs were submerged in the water pool.

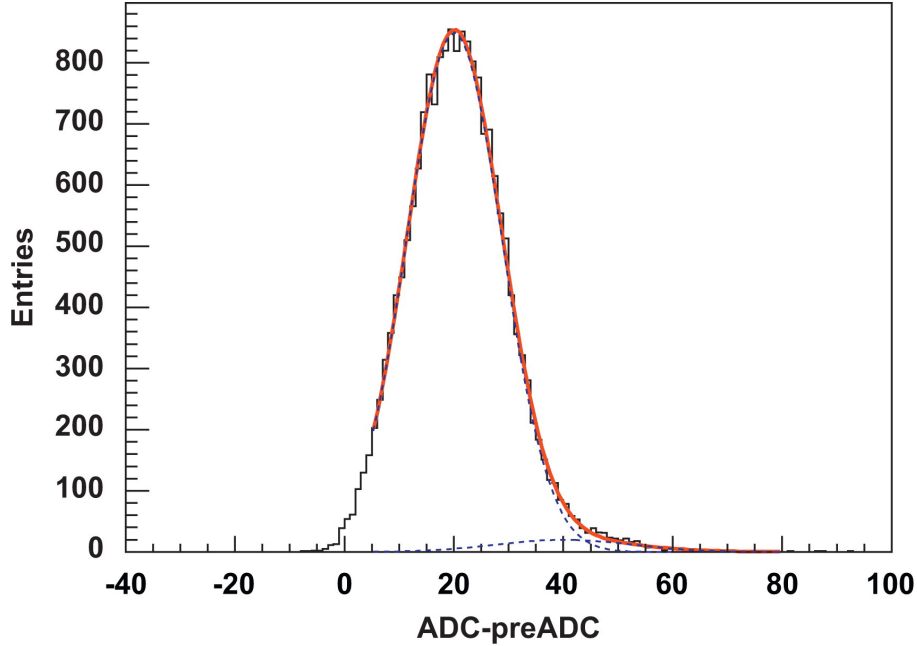
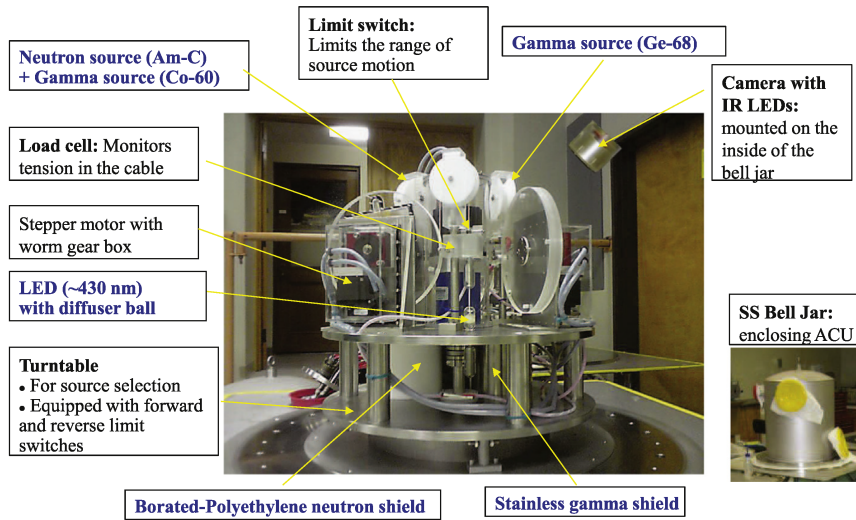
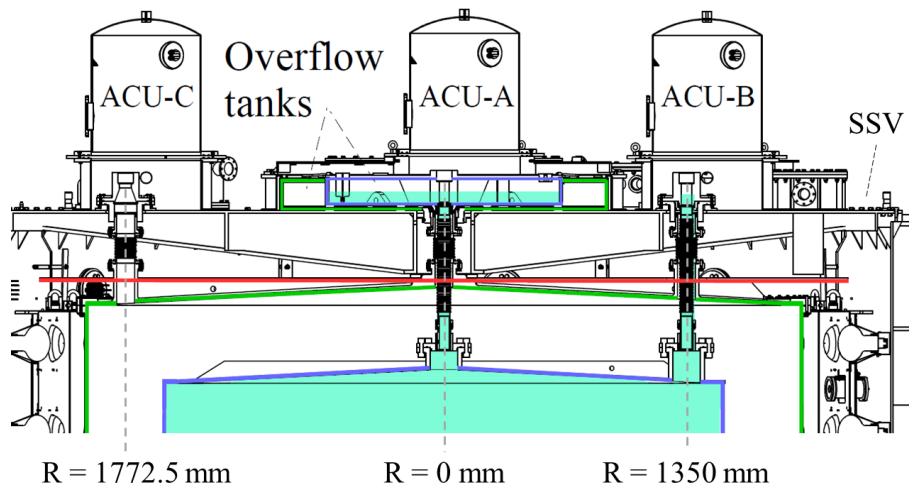


Figure 2.5 Example of the SPE distribution, with a small fraction of double photoelectrons. The main part of the overlaid fitting function is a Gaussian distribution. The x axis is the peak ADC subtracting the baseline of the ADC average before the pulse. Figure from reference^[95].

The weekly/monthly calibrations were performed simultaneously for all ADs with three calibration sources in every ACU^[95]. Since the Daya Bay experiment identified the electron antineutrino by detecting the positron and neutron signals from IBD reactions, the calibration sources include a positron source of ^{68}Ge , a combined source of ^{60}Co (γ source) and ^{241}Am - ^{13}C (neutron source), and a low-intensity LED source for PMT gain calibration. The cascade decays of $^{68}\text{Ge} \rightarrow ^{68}\text{Ga} \rightarrow ^{68}\text{Zn}$ (electron capture + positron emission) produce a positron, which typically annihilates inside the source enclosure, yielding two back-to-back 0.511 MeV γ 's. Therefore the ^{68}Ge source is effectively a γ source (~ 10 Hz in Daya Bay). The ^{60}Co is a widely used γ source, emitting two γ 's of 1.17 MeV and 1.33 MeV, while the Daya Bay ^{60}Co source rate is ~ 100 Hz. The 28 μCi ^{241}Am source produces alphas, which interact with the ^{13}C source and emit neutrons at a low rate of 0.7 Hz^[108]. The low-intensity LED source was used to generate single photoelectron (SPE) and study the PMT gain^[95], as shown in Fig. 2.5, with 19 ADC



(a) ACU structure



(b) Three ACUs installed on the lid of the SSV

Figure 2.6 Top: Photos of one ACU to show the internal structures and the outside stainless steel bell jar enclosing ACU to protect it from water pool^[95]. Bottom: side-view schematic diagram of the top part of the AD to show the three ACUs (labeled as ACU-A/B/C) installed on the lid of the SSV. Through the three calibration pipes, the calibration sources can be employed into the AD along three vertical axes ($R = 0/1350/1772.5 \text{ mm}$ for ACU-A/B/C separately from the AD central axis). The turquoise colored region is the volume filled with GdLS.

counts for SPE in average.

To investigate the energy response and construct the energy non-linearity model, two special calibration campaigns were conducted with more calibration sources during the summer of 2012 and at the end of 2016. Table 2.3 summarizes the additional neutron and γ sources used in Daya Bay experiment, and the energy information of the neutron

kinetic energy and γ energy. The neutrons are produced via $A(\alpha, n)B$ scattering in the source, while the recoiled nuclei B can be in ground/excited state, leading to high/low neutron kinetic energy. The neutron kinetic energy is one of the key factors in the neutron propagation process, and will affect the detector efficiency. This will be discussed in detail in Chapter 4 of the absolute efficiency study. The general Am-C neutron source used in weekly calibration has no ^{16}O in excited state after $^{13}\text{C}(\alpha, n)^{16}\text{O}$ scattering as the α s in the sources are moderated with a thin gold foil^[109]. The new Am-C neutron source used in the calibration campaign in 2016 had no such gold foil, and thus produced low kinetic energy neutrons with a signature similar to the IBD neutrons.

From the data analysis of the 6-AD period (before the 2012 summer), the Am-C source in ACU-B/C was found to produce IBD-like events (~ 0.2 Hz) in the detector, even when the source was parked above the SSV lid. Consequently, the Am-C source in ACU-B/C for the EH3 ADs were later removed to reduce the background level as the IBD rate in EH3 AD was relatively low (~ 74 Hz)^[95]. This made a difference in the background estimation for the 6-AD period and 8-AD period, which will be discussed in Chapter 2.6.

Table 2.3 The neutron and γ sources and their energy information of neutron kinetic energy or γ energy. Am-C and Pu-C ground/excited state means that ^{16}O after $^{13}\text{C}(\alpha, n)^{16}\text{O}$ scattering is in the ground/excited state. Similar for ^{12}C after $^9\text{Be}(\alpha, n)^{12}\text{C}$ scattering in Am-Be ground/excited state. The state of the recoiled nuclei will determine the neutron kinetic energy. The entry ‘‘Am-C, excited state’’ is only available for Am-C neutron source used in 2016 calibration campaign. The neutron from IBD is also listed here for a comparison. The fast neutrons from cosmic muons can have kinetic energy more than 100 MeV. The mean energy of the several γ 's emitted by neutron captured on Gd is about 2.1 MeV, with a total energy about 8 MeV.

Source type	Source	Neutron Kinetic Energy/ γ Energy [MeV]
Neutron source	Am-C, ground state	2.5-7.5
	Am-C, excited state	< 0.8
	Am-Be, ground state	4-10
	Am-Be, excited state	0-5
	Pu-C, ground state	3-7.5
	Pu-C, excited state	< 0.6
	(IBD)	< 0.1
	(fast neutron)	0-100+
γ source	^{68}Ge	2×0.511
	^{137}Cs	0.622
	^{54}Mn	0.8335
	^{60}Co	1.173+1.333
	^{40}K	1.461
	neutron captured on H (nH)	2.223
	neutron captured on Gd (nGd)	~ 8
	^{208}Tl	2.615
	neutron inelastic scattering on C	4.439
	neutron captured on C	4.945
	^{16}O 2 nd excited state (Am-C, Pu-C)	6.13
neutron captured on Fe	7.630	

2.5 Data Taking

In the Daya Bay experiment, the primary data came from 17 independent readout crates (8 ADs, three IWS, three OWS, and three RPC detectors). Based on a global timing system, the synchronized and configurable data acquisition (DAQ) system collected and coordinated the readouts from the same experimental hall in time series and stored them in the same data stream. The readout system of RPC detectors was documented in reference^[110]. The other detectors used the PMT-based readout system^[95,111]. The event

trigger was authorized by the number of over-threshold PMTs (NHIT) or the simple sum of all PMT charges (ESUM) within a specified time window satisfying the requirements. The accumulated charge and time information from all PMTs for the event were then recorded by the DAQ system, with a time interval between two events greater than $1 \mu\text{s}$ for one specific detector. During the data acquisition process, the situations of all the detectors were monitored by the DCS (detector control system) and the DAQ monitoring system. If there was any possible problem of the detectors, actions would then be taken to fix the problem and ensure the data quality.

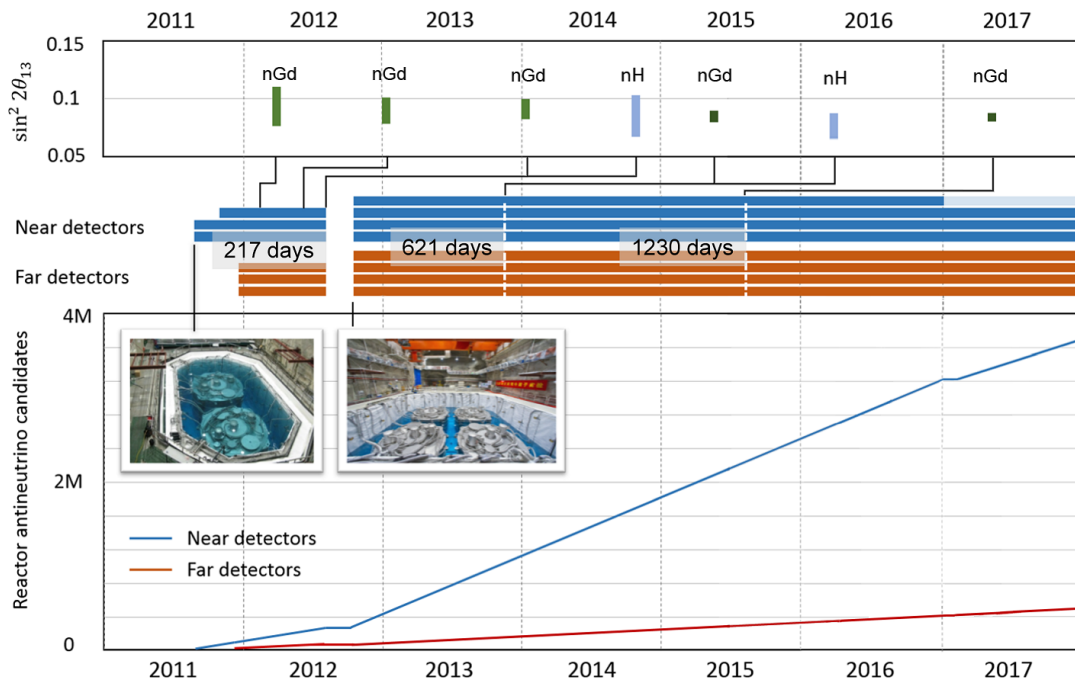


Figure 2.7 Daya Bay experiment operation timeline. The stripes in blue and orange colors represent the AD configuration along the timeline. The bottom panel shows the number of collected reactor antineutrino candidates increasing over time. In the top panel is the published measurements of $\sin^2 2\theta_{13}$ based on different data samples with both nGd and nH signals, which explicitly shows the decrease of measurement uncertainty along with the accumulated data sample.

The data taking of Daya Bay experiment began since December 24, 2011, with two ADs in EH1, one AD in EH2, and three ADs in EH3, until the pause in 2012 summer to install the last two ADs. A special calibration campaign was carried out during the maintenance as well. The data taking with full 8-AD configuration resumed on October 19, 2012 and continued until the calibration campaign in the end of 2016. Since then, the AD1 in EH1 has been used for test of the JUNO experiment, and the Daya Bay data

taking has been going on with 7-AD configuration, funded until the year of 2020. The operational efficiency of data acquisition was better than 97% with occasional pauses caused by maintenance and power outages. Each AD in EH1 and EH2 collected about 600 antineutrino candidates per day while that in EH3 about 74 antineutrino candidates per day. Fig. 2.7 shows the experimental operation, the approximate number of collected antineutrino candidates, and the published measurements of $\sin^2 2\theta_{13}$ based on different data samples with both nGd^[40,112,113] (IBD neutron captured on gadolinium) and nH^[87,114] (IBD neutron captured on hydrogen) signals. The most recent measurement used the data sample of 1230 days with more than 2.5 million reactor antineutrinos, which is the biggest cluster of antineutrinos ever observed by any experiment.

2.6 IBD Event Selection

The Daya Bay ADs identify the reactor antineutrinos via the IBD reaction of $\bar{\nu}_e + p \rightarrow e^+ + n$. The GdLS volume is the neutrino target in the analysis. Most of the energy released in reaction is carried away by the positron, with the neutron kinetic energy only about 10 keV. The positron deposits its kinetic energy in the liquid scintillator and annihilates with an electron, emitting two back-to-back 0.511 MeV γ 's. The positron may also have a small probability to annihilate during the flight. The deposited kinetic energy and the γ energies form the first signal, with the total energy $E \sim E_{\bar{\nu}_e} - 0.78$ MeV. The second signal of an IBD event is from the neutron. The neutrons are thermalized in the scintillator and then captured on the nuclei of various isotopes. Gadolinium is doped into the liquid scintillator to largely shorten the neutron capture time by increasing the neutron capture cross-section and increasing the released energy. The neutrons captured on ¹⁵⁵Gd and ¹⁵⁷Gd (two main gadolinium isotopes used in Daya Bay) will emit several γ 's with a total energy of 8.5 MeV and 7.9 MeV separately. This coincidence events with positron signal and neutron capture signal from IBD reactions help to identify the antineutrinos from the backgrounds.

We selected the coincident events with a prompt signal and a delayed signal from the data collected by the near ADs. The selection criteria were exactly the same as those given in reference^[40]. The details of the selections will be discussed in Section 4. The candidate events for each near AD are summarized in Table 2.4.

A number of background estimations have been performed as detailed in reference^[40]. The main backgrounds include the accidental background, the ⁹Li/⁸He and fast neutron

Table 2.4 Summary of IBD event candidates and backgrounds in each AD in the two near experimental halls^[40]. The $\bar{\nu}_e$ raw candidates are the numbers of IBD event candidates in each AD before background subtraction. The $\bar{\nu}_e$ numbers in the last row are the numbers of IBD events with all backgrounds subtracted.

	EH1-AD1	EH1-AD2	EH2-AD1	EH2-AD2
$\bar{\nu}_e$ raw candidates	597616	606349	567196	466013
DAQ livetime [days]	1117.178	1117.178	1114.337	924.933
ϵ_μ	0.8255	0.8221	0.8573	0.8571
$\bar{\epsilon}_m$	0.9744	0.9747	0.9757	0.9757
Accidentals [day^{-1}]	8.46 ± 0.09	8.46 ± 0.09	6.29 ± 0.06	6.18 ± 0.06
Fast neutron [day^{-1}]	0.79 ± 0.10		0.57 ± 0.07	
${}^9\text{Li}/{}^8\text{He}$ [day^{-1}]	2.46 ± 1.06		1.72 ± 0.77	
Am-C, 6-AD [day^{-1}]	0.27 ± 0.12	0.25 ± 0.11	0.28 ± 0.13	
Am-C, 8-AD [day^{-1}]	0.15 ± 0.07	0.16 ± 0.07	0.13 ± 0.06	0.15 ± 0.07
${}^{13}\text{C}(\alpha, n){}^{16}\text{O}$ [day^{-1}]	0.08 ± 0.04	0.07 ± 0.04	0.05 ± 0.03	0.07 ± 0.04
$\bar{\nu}_e$ rate [day^{-1}]	653.03 ± 1.37	665.42 ± 1.38	599.71 ± 1.12	593.82 ± 1.18
$\bar{\nu}_e$ number	586827	595681	558994	459317

backgrounds from cosmic muons, the Am-C background from our calibration sources, and the ${}^{13}\text{C}(\alpha, n){}^{16}\text{O}$ background in natural radioactivity. The evaluations of these backgrounds are also listed in Table 2.4. It is noted that the background contaminations account for only about 1.5% in the total event candidates. This is due to the fact that all the near detectors are close to the reactor cores and the neutrino flux is significantly large.

Our study to the reactor antineutrino anomaly were based on these IBD candidates. We investigated the systematic effects especially the IBD detection efficiency, including those from the energy response and the neutron related processes of propagation and nuclei de-excitation after capturing neutrons, in order to significantly improve the IBD detection efficiency and the energy spectrum measurement. To study the correlations between the reactor antineutrino flux/spectra and the reactor fuel fission cycle, we need to group the data from different runs according to the fission fractions of the fissionable isotopes. In this study we grouped the data into 8 fission fraction groups and estimate the candidate events and backgrounds inside these time periods separately.

Chapter 3 The Energy Non-linearity Model

Because of the scintillation quenching effect, Cherenkov radiation and the electronics, the detector response for the positrons from IBD reaction with different energies is non-linear. We need a reliable energy non-linearity model since it can affect the energy spectra for all particles and thus affect the efficiency estimations. In this chapter, I will present the modeling of the energy nonlinearity for the AD in Daya Bay, mainly based on the gamma calibrations. I will also present the implementation of the non-linear energy model in the Daya Bay simulation, which is used in the absolute efficiency study.

3.1 Gamma Calibrations

To model the energy non-linearity and measure the energy resolution of the detector, Daya Bay has done a lot of gamma calibrations, including the weekly calibrations with ^{60}Co and ^{69}Ge for monitoring the detector energy response stability, and special calibration campaigns in 2012 summer and 2016 winter with high energy γ sources. The γ sources used in energy calibration and the corresponding characteristic γ energies have been summarized in Table 3.1.

Table 3.1 The γ sources and γ energy used in energy calibration. The ^{40}K is from natural radioactivity. The mean energy of the several γ 's emitted by neutron captured on Gd is about 2.1 MeV, with a total energy about 8 MeV.

Source	γ Energy [MeV]
^{68}Ge	2×0.511
^{137}Cs	0.622
^{54}Mn	0.8335
^{60}Co	1.173+1.333
^{40}K	1.461
neutron captured on Gd (nGd)	~ 8
neutron captured on H (nH)	2.223
^{208}Tl	2.615
neutron inelastic scattering on C	4.439
neutron captured on C	4.945
^{16}O 2 nd excited state (Am-C, Pu-C)	6.13
neutron captured on Fe	7.630

The energy range of the γ 's varies from 0.6 MeV to 7.6 MeV, covering the possible γ energy from the real IBD signals. The γ sources are packaged inside small stainless steel capsules coated with acrylic (for weekly calibration, size Φ 20 mm \times 50 mm) or greenish Teflon (for 2012 summer calibration, size Φ 20 mm \times 66 mm). Although the source packages are small, a tiny fraction of scintillation photons will be absorbed by the source surface, which is called as the optical shadowing effect. The 1% level bias for the energy scale and resolution has been well studied by simulations and validated with measurement by special γ sources with high-reflective coating^[40].

3.2 Energy Non-linearity Model

The energy non-linearity is the non-linear relationship between the particle true energy and the energy after detector response with event reconstruction. For different types of particles, the energy non-linearity can also be different. The positron non-linearity is what we need to get the positron spectrum from IBD events. For Daya Bay detector, the energy non-linearity can be divided into 2 parts by the physics process: the scintillator non-linearity and the electronics non-linearity.

The charged particle propagating in the liquid scintillator can deposit its kinetic energy via ionization and produce the scintillation photons. Not all the energy of the particle are deposited in the detector, as the particle and its secondaries may escape from the detector. This is called as the energy leakage. In the energy non-linearity study, the sources were deployed in the detector center, thus the leakage was very limited. Because of the quenching effect that very dense ionization within short path leads to reduction of scintillation photons than expected, not all the deposited energy are converted into optical photons during the scintillation. An empirical equation named Birks' Law^[98,99] is widely used to evaluate the relationship between the deposited energy E_{dep} and the light yield in scintillator, as shown in equation (3-1),

$$\frac{dL}{dx} \propto \frac{-dE/dx}{1 + k_B(-dE/dx)}, \quad (3-1)$$

where dL/dx is the scintillator light yield per unit length; k_B is called the Birks' constant depending on a specific material; $-dE/dx$ is the energy loss per unit length (stopping power) with a negative sign due to the decreasing of energy. Another type of optical photons produced by the charged particles in the liquid scintillator is the Cherenkov

radiation^[101], when the charged particles travel faster than the phase velocity of light in the medium. The scintillation photons and Cherenkov radiation propagate in the detector and are then collected by the PMTs. Not all the optical photons are collected because of their attenuation in the liquid scintillator and the PMT coverage. This is the optical non-uniformity of the detector. The PMT photocathode converts the optical photons into photoelectrons (PEs) by probability (quantum efficiency, QE for short). The dynodes amplify the photoelectrons by a huge magnification and form the electronics signal. The slow component of scintillation photons can exceed the limited time window (< 400 ns) for charge readout from a single PMT, introducing extra non-linear effect, called as the electronics non-linearity. The signals in multiple triggered PMTs are then reconstructed into energy for later analysis. The neutral particle, such as γ and neutron, can also deposit energy and produce optical photons in the liquid scintillator, by the secondary electrons/positrons or recoiling the protons. The whole flowchart of all processes can be expressed as:

$$\begin{aligned}
 E_{\text{true}} &\xrightarrow{\text{scintillator NL}} E_{\text{dep}} \xrightarrow{\text{Optical non-uniformity} \times \text{QE}} qE_{\text{dep}} + E_{\text{Cherenkov}} \\
 &\xrightarrow{\text{electronics NL}} PE(E_{\text{vis}}) \xrightarrow{\text{electronics NL}} E_{\text{rec}},
 \end{aligned}$$

where E_{true} is the true energy of the particle at the beginning; E_{dep} is the deposited energy including by scintillation and by Cherenkov radiation; qE_{dep} is the effective deposited energy carried by the scintillation photons after quenching effect (note that no quenching effect for Cherenkov light); $E_{\text{Cherenkov}}$ is the energy deposited by Cherenkov radiation; E_{vis} is the visible energy seen by the detector (for simplicity, I think the visible energy is proportional to PE number, $E_{\text{vis}} = PE/S$); E_{rec} is the energy after reconstruction. The energy non-linearity (NL) is the relationship between the reconstructed energy and the true energy as equation 3-2,

$$\begin{aligned}
 NL &= \frac{E_{\text{rec}}}{E_{\text{true}}} \\
 &= \frac{E_{\text{vis}}}{E_{\text{true}}} \cdot \frac{E_{\text{rec}}}{E_{\text{vis}}} \\
 &= f_{\text{scintillator}} \cdot f_{\text{electronics}},
 \end{aligned} \tag{3-2}$$

where $f_{\text{scintillator}}$ and $f_{\text{electronics}}$ are the scintillator and electronics non-linearity separately.

In Daya Bay experiment, the modeling of energy non-linearity for a positron is equiv-

alent to a combination of an electron non-linearity with same kinetic energy (regardless of the charge) and the two annihilation γ non-linearity (also depends on the energy non-linearity of the secondary electrons/positrons) as $E_{\text{vis},e^+} = E_{\text{vis},e^-} + 2 \times E_{\text{vis},\gamma}$ (0.511 MeV). So the first step of modeling the positron energy non-linearity is to formulate that for an electron in the detector.

Based on the Birks' Law in equation (3-1), in a big detector as the Daya Bay AD, the electron scintillator non-linearity caused by the quenching effect can be expressed as

$$f_q(E_{\text{true}}, k_B) = \frac{qE_{\text{dep}}}{E_{\text{true}}} = \frac{1}{E_{\text{true}}} \int_{E_{\text{true}}}^0 \frac{1}{1 + k_B \cdot (-dE/dx)} dE, \quad (3-3)$$

without any leakage. The stopping-power $-dE/dx$ is obtained from the NIST (National Institute of Standards and Technology) database (ESTAR)^[115] and also from Geant4^[116–118]-based simulations. The curves of $f_q(E_{\text{true}}, k_B)$ calculated with different k_B (from 2 to 25.5 with step 0.1, in unit of 10^{-3} cm/MeV) are stored in files, prepared as input for the model fit. The ratio $f_C(E_{\text{true}})$ between the average number of emitted Cherenkov photons and the electron true energy was subtracted from a Geant4-based simulation, and confirmed by the independent analytic calculation^[1] as

$$f_C(E_{\text{true}}) \propto \frac{1}{E_{\text{true}}} \int_{\omega_1}^{\omega_2} \int_{E_{\text{true}}}^{E_{\text{threshold}}} \frac{\alpha}{-dE/dx} \left(1 - \frac{1}{\beta^2(E) \cdot n^2(\omega)}\right) \text{QE}(\omega) dE d\omega, \quad (3-4)$$

where α here is the fine structure constant; $E_{\text{threshold}}$ is the energy threshold to generate Cherenkov radiation in liquid scintillator; ω_1 and ω_2 are the acceptable frequency range of the PMTs; β is the ratio of velocity to speed of light; $n(\omega)$ is the refractive index depending on frequency; $\text{QE}(\omega)$ is the quantum efficiency of the PMT depending on frequency. The curve of $f_C(E_{\text{true}})$ is self-normalized and then recorded in file. Because of the discrepancy in detection efficiency between scintillation photons and Cherenkov light, an additional parameter k_C is introduced as the ratio of the Cherenkov radiation and scintillation photons for 1 MeV electrons. Therefore, the electron energy non-linearity in scintillator can be formulated as

$$f_{\text{scintillator}} = \frac{E_{\text{vis}}}{E_{\text{true}}} = f_q(E_{\text{true}}, k_B) + k_C \times f_C(E_{\text{true}}). \quad (3-5)$$

In essence, the γ 's deposit energy in liquid scintillator by imparting energy to electrons (via Compton scattering and photoelectric effect), and by producing electron-

positron pairs. The secondary γ 's energy are then imparted to electrons as well. As a result, all the γ energy are converted to the kinetic energy of the scattered electrons and positrons (effective to electrons), with a PDF (probability distribution function) of the electron kinetic energy for the $\gamma - e^-$ convention, as shown in Fig. 3.1. Then the γ non-

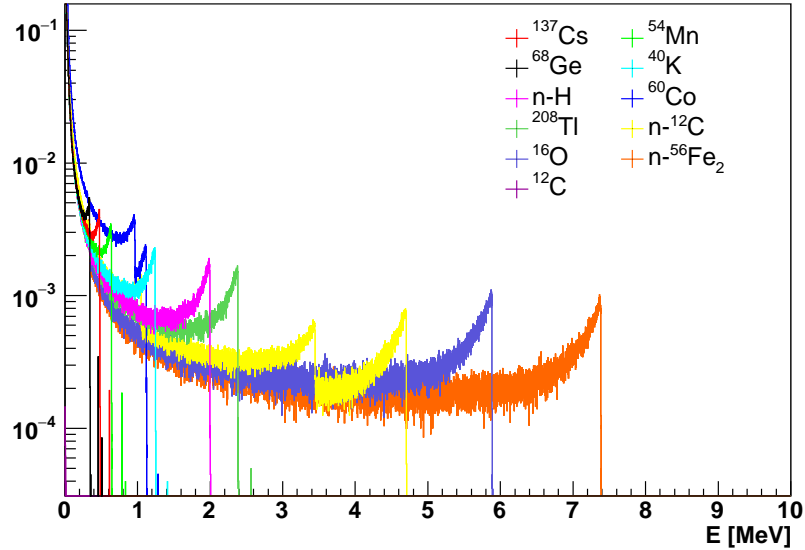


Figure 3.1 The $\gamma - e^-$ convention PDF for the γ sources used in gamma calibration in Daya Bay listed in Table 2.3. The x axis is the electron/positron kinetic energy.

linearity in scintillator can be obtained as the convolution of the electron non-linearity in scintillator in equation (3-5) and the convention PDF,

$$f_{\text{scintillator}}^{\gamma} = (\gamma - e^- \text{ convention PDF}) \otimes f_{\text{scintillator}}^{e^-} \quad (3-6)$$

The overall electronics non-linearity of the whole detector is almost the same for signals from different particles, suggested by the Monte Carlo (MC) simulation, with a form of an exponential function as

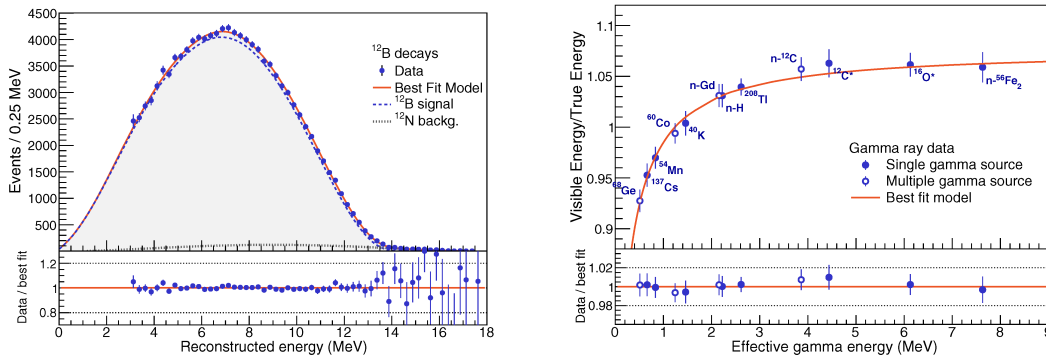
$$f_{\text{electronics}} = \frac{E_{\text{rec}}}{E_{\text{vis}}} = A \cdot (1 + \alpha \times e^{-E_{\text{vis}}/\tau}), \quad (3-7)$$

where A is the absolute energy scale, α and τ are parameters to characterize the exponential function. The functional form of equation (3-7) has been confirmed by dedicated tests^[40].

Thus in total, the energy non-linearity for an electron is parameterized using a semi-empirical physics-driven model with 5 parameters:

- (1) Birks' constant (k_B) and Cherenkov fractional contribution at 1 MeV (k_C) in the scintillator non-linearity in equation (3-5);
- (2) Absolute energy scale (A), amplitude (α) and decay constant (τ) in the electronics non-linearity in equation (3-7).

In the analysis of reference^[40], this semi-empirical model was applied to the measured ^{12}B β spectrum (induced by cosmic muons) and 12 γ peaks (listed in Table 2.3) with an unconstrained χ^2 fit, as shown in Fig. 3.2. The best-fit model gave the parameter values as: $k_B = 15\text{cm/MeV}$, $k_C = 0.5\%$, $\alpha = 0.078$ and $\tau = 2.55$ MeV.


 (a) ^{12}B β spectrum fit

 (b) γ peaks fit

Figure 3.2 Left: the measured ^{12}B β spectrum (with limited ^{12}N background) overlaid with the prediction from best-fit model. Right: the best-fit model prediction overlaid with the γ peaks in calibrations. Both of the figures show a very good agreement. Figures from reference^[40].

Based on the best-fit model for the electron energy non-linearity of $E_{\text{rec}}/E_{\text{true}}$, the positron energy non-linearity can be obtained by adding the energy non-linearity of the 2×0.511 MeV annihilation γ 's, as shown in Fig. 3.3. The 1σ allowed region from model variations constrains the non-linearity to better than 1% above 2 MeV. This model is used in the non-linearity correction for the positron spectra in the data analysis, referred to as the **nominal model**. An independent fitted model, from the Michel electron spectrum and the $\beta + \gamma$ spectra of bismuth (Bi) and thallium (Th) decays, provides a well consistent result, which is also shown as the cross-validation in Fig. 3.3.

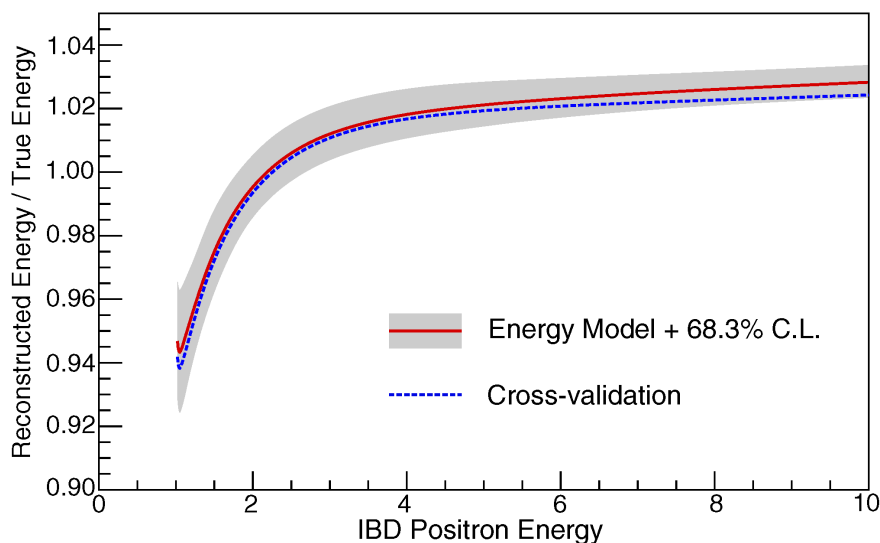


Figure 3.3 The positron energy non-linearity of $E_{\text{rec}}/E_{\text{true}}$ based on the best-fit model (red solid line). The IBD positron energy on x axis includes the 2×0.511 MeV annihilation γ 's. The cross-validation (blue dashed line) is an independent estimation from the fit applied to the Michel electron spectrum and the $\beta + \gamma$ spectra of bismuth (Bi) and thallium (Th) decays, showing a consistent result. Figure from reference^[40].

3.3 Energy Non-linearity Model in Simulation

The well-established energy non-linearity model showed very good agreement with the measurements in Section 3.2, however it varies a lot from the previous Monte Carlo (MC) simulation in the Daya Bay experiment. The Daya Bay MC simulation is based on the Geant4 tool, with a lot of user-defined modules. The physics processes of scintillation and Cherenkov radiation were implemented by private codes, mainly following the mechanism presented in Section 3.2. The MC simulation can provide us with the truth information and some invisible events, which are very useful for investigating the detector response. A precise estimation of the detector absolute efficiency requires a reliable MC simulation, which had better to be consistent with the real detector as well as possible. The author of this thesis did a lot of work to tune the related parameters for energy non-linearity in the MC simulation, making it agree with the nominal model much better. In this section, I will refer to the previous version of MC in Daya Bay as the **default MC**, and refer to the new version of MC as the **tuned MC**.

To check the difference between the simulation and the nominal model from data measurement, electron/ γ /positron samples with uniform spectra from 0 MeV to 10 MeV were generated with their initial vertices uniformly distributed in the detector by the default

MC. The scintillator non-linearity (including the scintillation and Cherenkov radiation) in nominal model and the default MC are found to be quite different, as shown in Fig. 3.4. From Fig. 3.4(a) we can see that the contribution from Cherenkov radiation in the

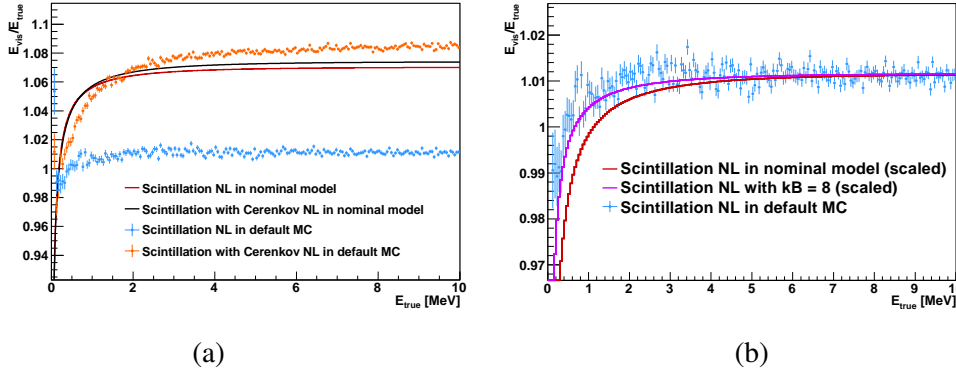


Figure 3.4 Left: scintillator non-linearity (scintillation+Cerekov) comparison between the nominal model and the default MC. The scintillation NL here presents the non-linearity caused by the quenching effect. The contribution of Cherenkov radiation in the default MC (about 5% at 1 MeV) is much bigger than that in the nominal model (0.5% at 1MeV). Right: scintillation NL comparison among curves with different values of Birks' constant (the lines are scaled to the same height, to focus on the shape difference).

nominal model (discrepancy between the black line and red line, 0.5% at 1 MeV from best-fit) is much smaller than the default MC (discrepancy between the orange dotted line and the blue dotted line, about 5% at 1 MeV). Thus I need to reduce the Cherenkov light yield in the MC.

The Birks' constant would change the shape and the absolute amplitude (due to less scintillation photons generated) of scintillator non-linearity curve at the same time. To compare the shapes of the non-linearity curves with different values of the Birks' constant, extra scaling have bee applied to some of the curves in Fig. 3.4(b) to get all curves in the same height. From this comparison, we can clearly see that the effective Birks' constant in default MC is obvious smaller than the Birks' constant in nominal model (15×10^{-3} cm/MeV), as the line with $k_B = 8 \times 10^{-3}$ cm/MeV is in the middle of them. This indicates that I should increase the value of Birks' constant in the MC. The default value of Birks' constant (6.5×10^{-3} g/(cm² · MeV), effective to 7.6×10^{-3} cm/MeV after considering the liquid scintillator density) in MC is from the measurement performed with neutrons using the Daya Bay liquid scintillator (Weili Zhong *et al.* in Daya Bay). This material density

independent Birks' constant is used in the Birks' Law a little different to equation (3-1) as

$$\frac{dL}{dx} \propto \frac{-dE/dx}{1 + k_B \cdot \rho \cdot (-dE/dx)}, \quad (3-8)$$

where ρ is the medium density. This value of $6.5 \times 10^{-3} \text{g}/(\text{cm}^2 \cdot \text{MeV})$ from measurement is proper for neutron/proton quenching, but it is not suitable for the electron/ γ /positron cases. So I decided to increase the Birks' constant value for electron/ γ /positron while keep the default Birks' constant value if the particle is a proton, in the simulation.

Then I checked the electronics non-linearity of nominal model and default MC. With $E_{\text{vis}} = PE/S$ (S is the energy scale of PE per MeV), the electronics non-linearity equation can be expressed as

$$\begin{aligned} f_{\text{electronics}} &= \frac{E_{\text{rec}}}{E_{\text{vis}}} = \frac{E_{\text{rec}}}{PE/S} \\ f_{\text{electronics}}^{PE} &\equiv \frac{E_{\text{rec}}}{PE} \\ &= A/S \cdot (1 + \alpha \times e^{-PE/S\tau}) \\ &= 1/S' \cdot (1 + \alpha \times e^{-PE/S'\tau'}). \end{aligned} \quad (3-9)$$

The absolute energy scale can be absorbed in the energy scale of PE per MeV, as $S' = S/A$. To maintain the equation of $S'\tau' = S\tau$, we need $\tau' = \tau \cdot A$. Then I used this function to fit with the electron/ γ /positron electronics response, as shown in Fig. 3.5. The prime symbol of the parameters in equation (3-9) are ignored in the fit result box. The fit range of PE number is from 200 to 2000, as the form part of the distribution differs from our single exponential model. The fit results are summarized in Table 3.2. The weighted

Table 3.2 Electronics non-linearity fit results for electron/ γ /positron samples in MC, compared with those from the nominal model. A weighted average of the simulations is also given.

	S	α	τ
Electron	210.3±0.1	0.072±0.001	2.21±0.06
γ	210.5±0.1	0.070±0.001	2.21±0.07
Positron	210.5±0.1	0.073±0.003	2.21±0.13
Average	210.4±0.1	0.071±0.002	2.21±0.07
Data	~ 168	0.078±0.017	2.55±0.49

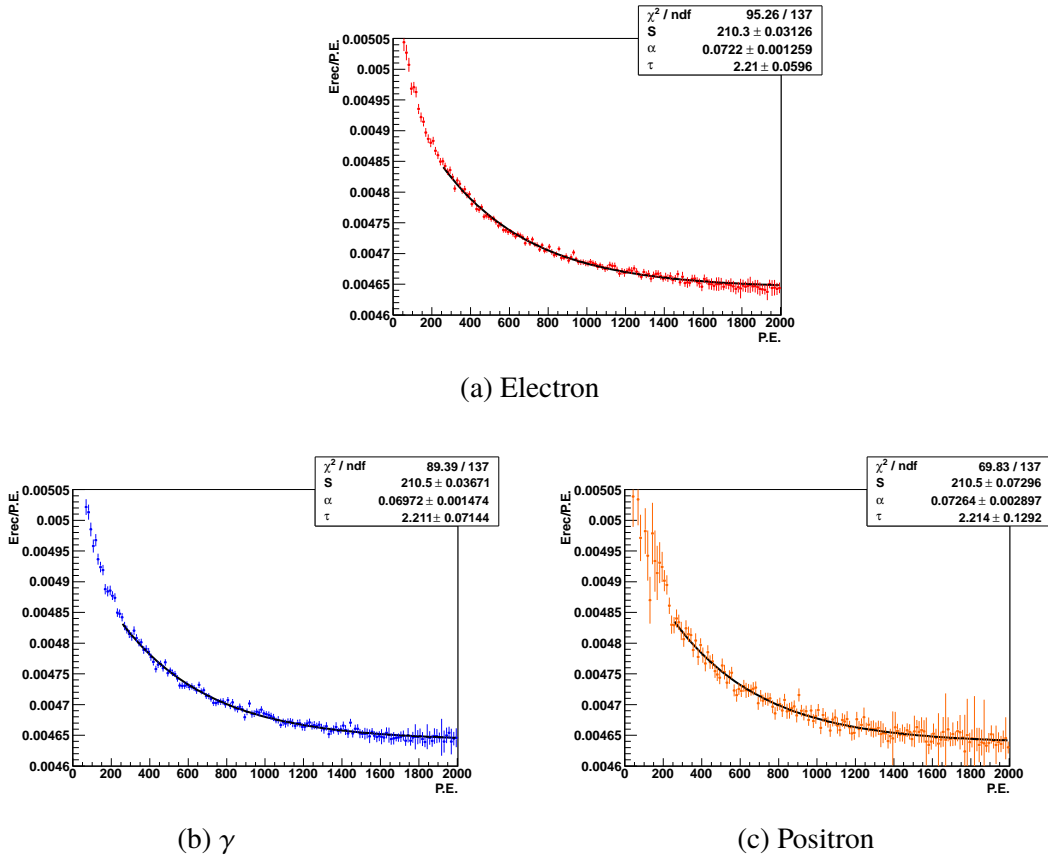


Figure 3.5 Electronics non-linearity for electron/ γ /positron samples in MC (the red/blue/orange points) overlaid with the best-fit with equation (3-9) (the black lines).

average of fit results from three samples is $S = 210.4$, $\alpha = 0.071$, $\tau = 2.21$. The energy scale of PE per MeV in MC (210) has some discrepancy with the measurement from data (~ 168). This may be caused by the differences of photon attenuation and PMT quantum efficiency between MC and real detector. The other two parameters of α and τ are consistent within uncertainty. I overlaid the electronics non-linearity curves from the nominal model, the MC and the weighted average fit result in the same plot as shown in Fig. 3.6. The difference between the electronics non-linearity of nominal model and MC above 4 MeV is within 0.5%. The lower energy region below 1 MeV has big difference but this energy region is out of interest as it is not important in the prompt spectrum of positron signal in IBD events. Since the electronics response modification in MC is tough and the discrepancy between data and MC is small, I decided to keep it.

In conclusion, we should reduce the Cherenkov light yield and increase the Birks' constant for electron/ γ /positron in the MC to have a better agreement with the nominal model. After several trials, I found that when I changed the Birks' constant as $15.8 \times 10^{-3} \text{g}/(\text{cm}^2 \cdot \text{MeV})$ and reduced the Cherenkov light yield as 10% of the original yield,

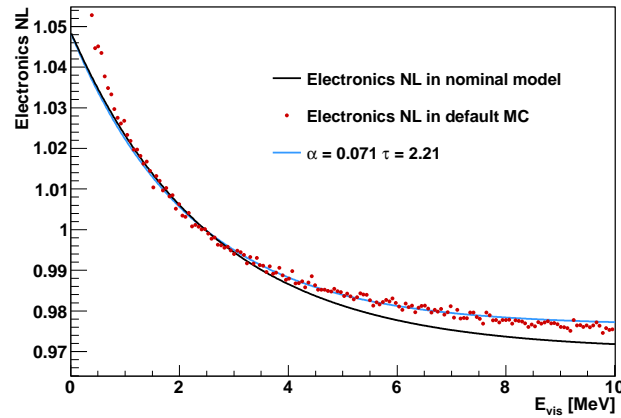


Figure 3.6 Electronics non-linearity comparison: black line for nominal model; red dot for default MC; blue line for the weighted average of fit results from MC samples. A discrepancy of 0.5% above 4 MeV between the nominal model and the MC could be seen.

the positron non-linearity in the tuned MC and nominal model were consistent within the allowed band, as shown in Fig. 3.7. The non-linearity of tuned MC after 4 MeV is

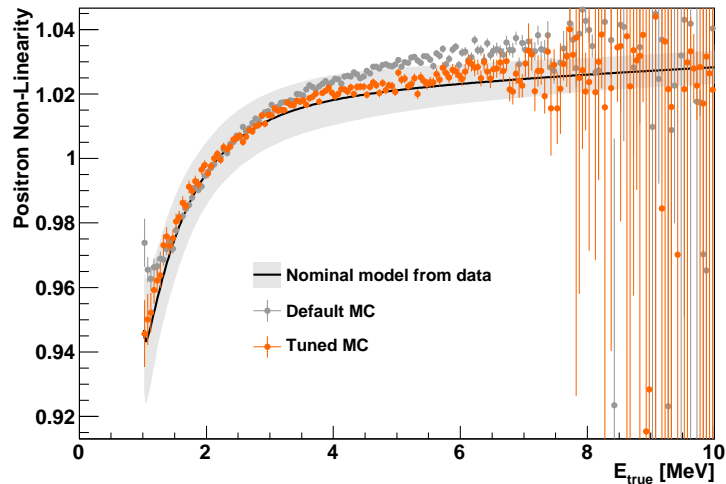
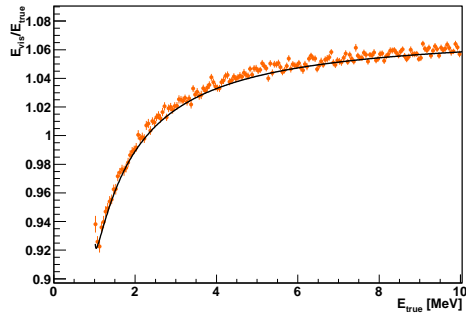


Figure 3.7 Positron non-linearity comparison: black line for the nominal model with 1σ allowed region (gray band), gray dots for default MC and orange dots for the tuned MC. The tuned MC is consistent with the nominal model within the 1σ allowed region, except for the region above 7 MeV with big statistic uncertainty.

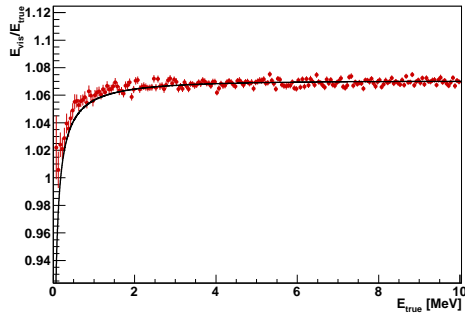
a little higher than nominal model but still within 1σ variation. This should be caused by the discrepancy in electronics non-linearity, where the MC is 0.5% higher than the nominal model as well. As a comparison, the default MC non-linearity curve gets out of the allowed band after 5 MeV, and it also has big discrepancy with the nominal model

below 2 MeV.

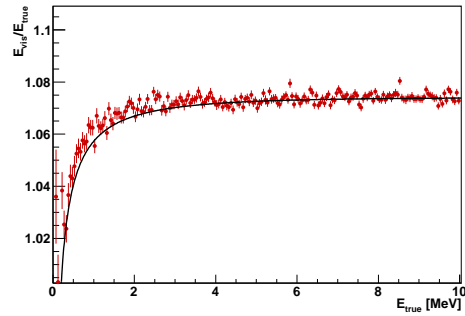
Besides, I have done more confirmations for this tuned MC as shown in Fig. 3.8. From the plots, for all samples with electron/ γ /positron, the scintillator non-linearity (scintillation+Cherenkov light) all have very good agreement with the nominal model. This indicates the tuning of the Birks' constant and Cherenkov light yield in MC is effective and reliable. Note that in MC, this tuning of Birks' constant is only applied to electron/ γ /positron while the Birks' constant for proton is still the same as before which is obtained from direct measurement.



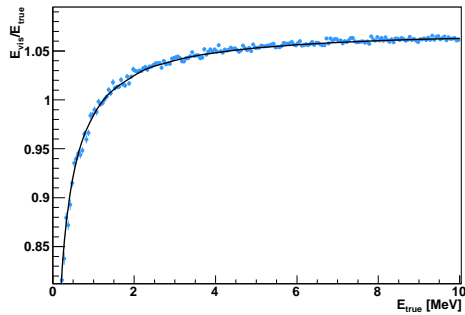
(a) Scintillator non-linearity for positron: black line for nominal model; orange dots for tuned MC.



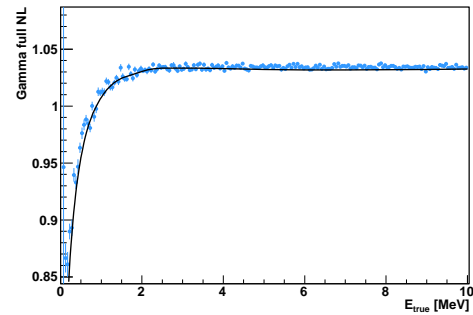
(b) Scintillation non-linearity (without Cherenkov light) for electron: black line for nominal model; red dots for tuned MC.



(c) Scintillator non-linearity (scintillation+Cherenkov) for electron: black line for nominal model; red dots for tuned MC.



(d) Scintillator non-linearity for γ : black line for nominal model; blue dots for tuned MC.



(e) Full non-linearity for γ : black line for nominal model; blue dots for tuned MC.

Figure 3.8 Non-linearity comparison of the nominal model (black lines) and the tuned MC with electron/ γ /positron sample (points in red/blue/orange). Good agreements can be seen in all plots.

Chapter 4 IBD Detection Efficiency Study

In this chapter I will present the new estimation of the IBD detection efficiency, with the uncertainty much improved than before by 40%. This improvement is based on the study of the correlated efficiencies related to neutron. With the help of neutron calibrations, I studied the correlations between the delayed spectrum and the neutron captures on various isotopes. This eventually enable me to obtain precision Monte Carlo simulation for the processes of neutron propagation in different detector materials and the de-excitation of nuclei after capturing the neutrons, improving the entire agreement between simulations and real detector performance.

4.1 Definition of Efficiency

By definition, the IBD detect efficiency is the ratio of the number of detected IBD events with the selections to the number of IBD events generated by the target volume. In the general Daya Bay analysis, we used the GdLS region as the neutrino target volume and only select the nGd events to have a good signal/background ratio.

The IBD events generated in the GdLS region is written as

$$N_{\text{gen}} = \phi\sigma N_{\text{proton}}, \quad (4-1)$$

where $\phi\sigma$ is the integral for the product of the reactor antineutrino flux and IBD cross-section over the full energy region, N_{proton} is the number of target protons in the GdLS region. Meanwhile, the detected IBD events with selections in an AD can be expressed as

$$N_{\text{det}} = \phi\sigma N_{\text{proton}} \epsilon_{\mu \text{ veto}} \epsilon_{\text{multiplicity}} \epsilon_{\text{flasher}} \epsilon_{\text{Gd}} \epsilon_{\text{spill-in}} \epsilon_{\text{tail}} \epsilon_{\text{prompt}} \epsilon_{\text{time}}, \quad (4-2)$$

where

1. $\epsilon_{\mu \text{ veto}}$ is the efficiency of muon veto,
2. $\epsilon_{\text{multiplicity}}$ is the efficiency to reject events with multiplicity > 2 ,
3. $\epsilon_{\text{flasher}}$ is the efficiency to remove the flasher events in PMTs,
4. ϵ_{Gd} is the neutron capture fraction on the gadolinium for the IBD events generated within the GdLS region,

5. $\epsilon_{\text{spill-in}}$ is effectively an overall correction for the target proton number since the neutrons from IBD events generated in the other materials (LS and acrylic) of the detector may travel into the GdLS region and get captured on gadolinium while the neutrons from IBD events generated in the GdLS region may also escape from the region.
6. ϵ_{tail} is the delayed energy cut efficiency of 6 MeV to exclude the tail events, or called as the nGd detection efficiency,
7. ϵ_{prompt} is the energy cut efficiency for the prompt signals,
8. ϵ_{time} is the efficiency for the nGd IBD events having a neutron capture time smaller than the given coincidence window T_C .

The three efficiencies of Gd capture fraction (ϵ_{Gd}), spill-in correction ($\epsilon_{\text{Spill-in}}$) and nGd detection efficiency (ϵ_{tail}) related to the neutron signal can be explicitly written as

$$\begin{aligned}
 \epsilon_{\text{Gd}} &= \frac{N(\text{IBD generated in GdLS, neutron captured on Gd})}{N(\text{IBD generated in GdLS})} \\
 \epsilon_{\text{Spill-in}} &= \frac{N(\text{IBD generated in GdLS+LS+acrylic, neutron captured on Gd})}{N(\text{IBD generated in GdLS, neutron captured on Gd})} \\
 \epsilon_{\text{tail}} &= \frac{N(\text{IBD generated in GdLS+LS+acrylic, neutron captured on Gd, } E_{\text{delayed}} > 6 \text{ MeV})}{N(\text{IBD generated in GdLS+LS+acrylic, neutron captured on Gd})},
 \end{aligned} \tag{4-3}$$

where the acrylic stands for the acrylic vessels holding the GdLS and LS.

The IBD detection efficiency is then the product of all the efficiencies as

$$\epsilon_{\text{IBD}} = \epsilon_{\mu \text{ veto}} \epsilon_{\text{multiplicity}} \epsilon_{\text{flasher}} \epsilon_{\text{Gd}} \epsilon_{\text{spill-in}} \epsilon_{\text{tail}} \epsilon_{\text{prompt}} \epsilon_{\text{time}}. \tag{4-4}$$

4.2 Study of Correlated Efficiencies

In previous Daya Bay analysis^[40], the IBD detection efficiency had contributions from all the cuts as shown in Table 4.1.

Besides the target protons number term, most of the uncertainty come from the three terms related to neutrons: Gd capture fraction (ϵ_{Gd}), nGd detection efficiency (ϵ_{tail}), and spill-in correction ($\epsilon_{\text{Spill-in}}$). The total IBD detection efficiency can be presented as:

$$\epsilon_{\text{IBD}} = \epsilon_{\text{other cuts}} \epsilon_{\text{Gd}} \epsilon_{\text{tail}} \epsilon_{\text{Spill-in}} \tag{4-5}$$

The neutrons from IBD reactions have a kinetic energy of 10 keV scale, and the

Table 4.1 Summary of contributions to the total IBD detection efficiency and systematic uncertainties. Dominating terms are in bold. Muon veto and multiplicity cut efficiencies vary among sites and have negligible uncertainty, hence they are not listed here.

Source	ϵ	$\delta\epsilon/\epsilon$
Target protons	-	0.92%
Flasher cut	99.98%	0.01%
Capture time cut	98.70%	0.12%
Prompt energy cut	99.81%	0.10%
Gd capture fraction	84.17%	0.95%
nGd detection efficiency	92.71%	0.97%
Spill-in correction	104.86%	1.00%
Combined	80.60%	1.93%

typical neutron propagation path from the birth place is tens of centimeters. A neutron from IBD at the boundary of GdLS region can easily go through the 5-cm thick inner acrylic vessel (IAV), propagate into the LS region and eventually get captured on hydrogen. The contrary direction of propagation process can also happen. The overall effect is the spill-in correction. Then I can know that the neutron propagation process in the detector determines where it is captured (capture position), thus directly determines the Gd capture fraction and spill-in correction. The de-excitation gamma spectrum from nGd capture, the nGd capture position and gamma propagation process in the detector determine the nGd detection efficiency. As a consequence, these three terms are highly related to the neutron propagation process and detector geometry, thus correlated to each other. The basic idea to improve the IBD detection efficiency precision is to combine them together as a IBD delayed efficiency (ϵ_D). The total uncertainty may shrink compared with previous isolated uncertainties because of the correlations between the three terms. Combined with equation (4-4) and the efficiency definitions, the IBD detection efficiency can be presented as:

$$\begin{aligned}
 \epsilon_{\text{IBD}} &= \epsilon_{\text{other}} \epsilon_D \\
 \epsilon_D &= \epsilon_{\text{Gd}} \epsilon_{\text{tail}} \epsilon_{\text{Spill-in}} \\
 &= N_{\text{Total,Gd,E}>6 \text{ MeV}} / N_{\text{GenInGdLS}}
 \end{aligned}
 \tag{4-6}$$

The term $N_{\text{Total,Gd,E}>6}$ is the number of all the nGd IBD events with delayed-energy greater

than 6 MeV; $N_{\text{GenInGdLS}}$ is the number of IBD events generated in the GdLS volume. the IBD delayed efficiency is studied directly from the MC simulations.

From the definition I can know that estimation of this IBD delayed efficiency highly relies on the good knowledge of neutron propagation process and nGd de-excitation process in the detector. A comprehensive understanding of these neutron related physics is urgent for the IBD delayed efficiency study. Although the Daya Bay experiment had the weekly neutron calibration and a special calibration in 2012 summer with high rate neutron sources, the already existing neutron calibration data are not enough for a well understand of the full detector response for the neutrons, due to the reasons of source intensity and background levels. Therefore, at the end of 2016, a new neutron calibration was conducted with well designed neutron sources of AmC ($^{241}\text{Am}-^{13}\text{C}$) and AmBe ($^{241}\text{Am}-^9\text{Be}$) for multiple positions in the detector. The estimation of the IBD delayed efficiency and uncertainty was studied with Monte Carlo (MC) simulations, and the MC was validated by data and MC comparison in many aspects with the new neutron calibration.

4.3 Neutron Propagation and nGd De-excitation Study via Neutron Calibration

New AmC source (neutron rate about 120 Hz) and AmBe source (neutron rate about 30 Hz) were ordered from CIAE (China Institute of Atomic Energy). They were used to do the neutron calibration in the detector of EH1-AD1. AmBe source was deployed in ACU-A/ACU-B/ACU-C, while AmC source was only deployed in ACU-B/ACU-C. The detailed position and duration are summarized in Table 4.2. The new AmC and AmBe sources don't have the golden foil to attenuate the α particle energy as the previous used neutron sources, leading to higher neutron energy and the possible transitions to the excited state for the recoiled nuclei. This feature was also implemented in the simulations for the new calibration.

4.3.1 Mechanism of the AmC and AmBe Neutron Source

In this section, I would introduce the mechanism and observed signals for the AmC and AmBe neutron sources. This is related to the event selection in the Section 4.3.3.

Table 4.2 Summary of neutron calibration position and duration. The radii of ACU-A/B/C are their horizontal distance to the central vertical axis.

	ACU-A ($R = 0$ mm)	ACU-B ($R = 1350$ mm)	ACU-C ($R = 1772.5$ mm)
position [m]	1.5	1.5	1.6
		1.35	1.35
	0.75	0.75	0.75
	0	0	0
	-0.75	-0.75	-0.75
	-1.45	-1.35	-1.35
		-1.45	-1.6
duration [hours]		AmC ~ 5	AmC ~ 5
	AmBe ~ 3.5	AmBe ~ 2.5	AmBe ~ 1.5

4.3.1.1 AmC Neutron Source

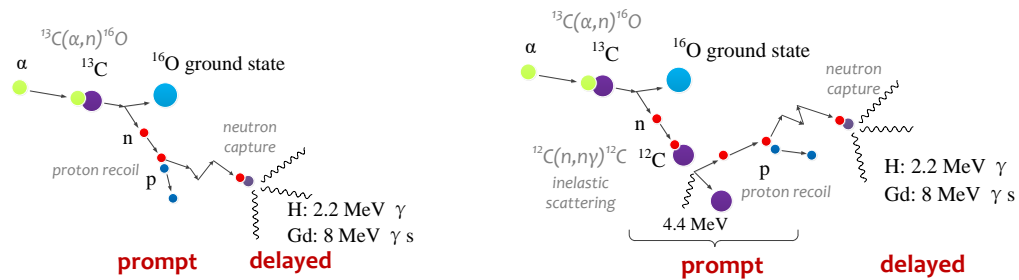
The basis of AmC neutron source is that the α from ^{241}Am decay scatters with ^{13}C by $^{13}\text{C}(\alpha, n)^{16}\text{O}$. The ^{16}O after scattering can be in either ground state (GS) or excited state (ES).

- (1) For the case of ^{16}O in ground state, the emitted neutron after scattering has high kinetic energy. It can propagate in the detector for a long path during the process of thermalization^①. In liquid scintillator, the thermalization process is carried out mainly by neutron scattering with protons. The recoiled protons form the first signal (prompt signal) in the detector. As the neutron initial kinetic energy can be as high as 7 MeV, the neutron may have an inelastic scattering with ^{12}C by $^{12}\text{C}(n, n)^{12}\text{C}^*$ (nC* scattering), emitting a characteristic 4.4 MeV γ . This γ and the recoiled protons together form the first signal (prompt signal). Then the thermal neutron gets captured by gadolinium (nGd, emitting γ 's with total energy about 8 MeV) or hydrogen (nH, emitting a 2.2 MeV γ). The de-excitation γ (s) form the second signal (delayed signal) in the detector. These two correlated signals are the coincidence signals I need from the detector. The whole event is illustrated in Fig. 4.1.
- (2) For the case of ^{16}O in excited state, the emitted neutron after scattering has low kinetic energy correspondingly, with a much shorter propagation path. The first

① The so-called thermalization process is that the neutron loses its kinetic energy and slows down by scattering with nuclei for many times until the neutron kinetic energy is less than eV-scale. These neutrons are referred to as thermal neutron, which are very easy to be captured by other nuclei.

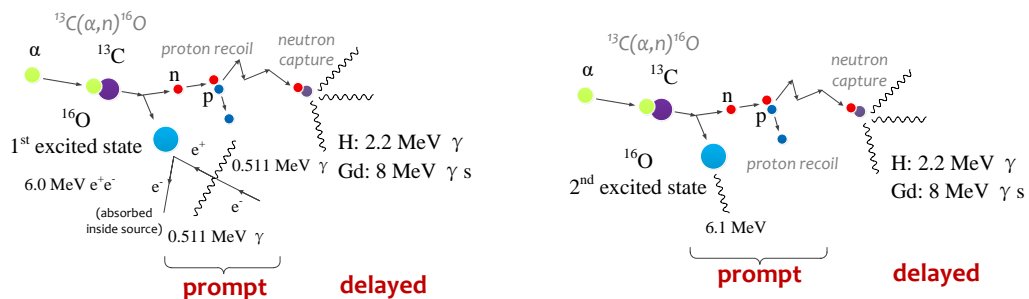
excited state of ^{16}O ($JP=0+$) decays via electron-positron pair (the $0+$ to $0+$ decay via γ channel is forbidden)^[119], but their kinetic energies are nearly all deposited inside the source package. Therefore, only the annihilation γ 's from the position can be detected, which forms the prompt signal together with the recoiled proton. The neutron capture forms the delayed signal. The second excited state of ^{16}O emits a 6.1 MeV γ . The prompt signal is from this high energy γ together with the recoiled protons. The delayed signal is from neutron capture as well. The whole event is illustrated in Fig. 4.2.

The kinetic energy of neutron from the sources have been summarized in Table 2.3. The neutron kinetic energy determines the neutron propagation path and capture position. This effect would be confirmed in the Section 4.3.2. It would affect the nH/nGd ratio and delayed spectrum, related to the IBD delayed efficiency. Thus I will categorize the events according the prompt energy (directly related to neutron kinetic energy) in the Section 4.3.3 of event selection.



(a) proton recoil only, E_{prompt} : 0-4 MeV (b) nC scattering and proton recoil, E_{prompt} : 4-5.5 MeV

Figure 4.1 Illustration for signals of AmC source with ^{16}O in ground state



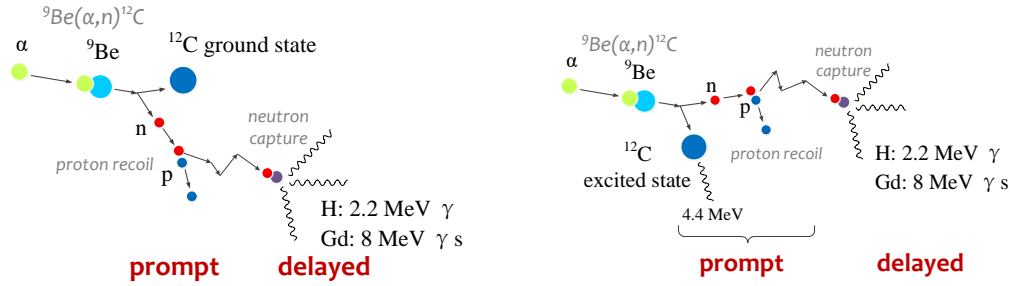
(a) ^{16}O in 1st excited state, E_{prompt} : 0-1 MeV (b) ^{16}O in 2nd excited state, E_{prompt} : 5.5-7 MeV

Figure 4.2 Illustration for signals of AmC source with ^{16}O in excited state

4.3.1.2 AmBe Neutron Source

The basis of AmBe neutron source is that the α from ^{241}Am decay scatters with ^9Be by $^9\text{Be}(\alpha,n)^{12}\text{C}$. The ^{12}C after scattering can be in either ground state or excited state.

- (1) For the case of ^{12}C in ground state, the emitted neutron after scattering has high kinetic energy, just like the case of ^{16}O in ground state in AmC source. The recoiled protons in neutron thermalization form the prompt signal in the detector. The neutron capture forms the delayed signal.
- (2) For the case of ^{12}C in excited state, the emitted neutron after scattering has low kinetic energy correspondingly, with a much shorter propagation path. The ^{12}C in excited state emits a 4.4 MeV γ , which together with the recoiled proton form the prompt signal. The neutron capture forms the delayed signal. These two cases of AmBe source events are illustrated in Fig. 4.3.



(a) ^{12}C in ground state, E_{prompt} : 1-4 MeV (b) ^{12}C in excited state, E_{prompt} : 4.2-7 MeV

Figure 4.3 Illustration for signals of AmBe source

4.3.2 Impact of Neutron Kinetic Energy on Neutron Propagation Process

We have emphasised that the kinetic energy of neutron determines the propagation path, thus I categorized the events into ground state events and excited state events. It's essential to validate it with data and MC simulation. The details about our neutron calibration MC simulations will be discussed in Section 4.4.

We know that our data and MC have very good agreement for distance distribution with reconstructed vertices. It indicates the MC has good simulation for the neutron scattering. It is reasonable to trust the true vertices information from MC truth. Fig. 4.4 show the prompt-delayed events true distance distribution comparison for ground state events and excited state events. In sub-figure (a) for AmBe source, I used 4 MeV cut to separate the ground state events and excited state events. In sub-figure (b) for AmC

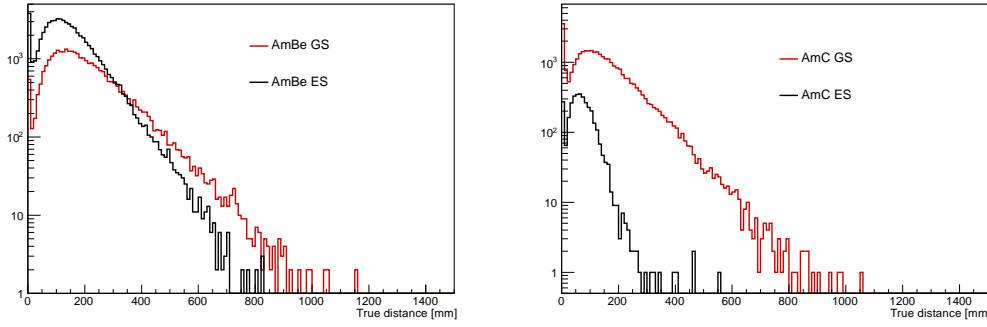
(a) AmBe source in ACU-A, $z = 0$ m.(b) AmC source in ACU-B, $z = 0$ m.

Figure 4.4 Prompt-delayed events true distance distribution comparison for ground state events (red line) and excited state events (black line).

source, the cut for ground state events is 1-5.5 MeV, to exclude some excited state events of 0-1 MeV energy region. This is different from the standard prompt energy cut, as the distance distribution is really sensitive to the neutron kinetic energy. From the figures we can clearly see that the neutrons in ground state events with higher kinetic energy have a longer propagation path than the neutrons in excited state events with lower kinetic energy. This is exactly what we expect.

This prompt-delayed events distance distribution check shows that our data and MC have good agreement, and the neutron propagation path is really sensitive to the kinetic energy, which is important for the neutron scattering.

4.3.3 Event Selection and Background Subtraction For Neutron Calibration

To get the neutron signals of two coincidence events from AmC and AmBe source as described in section 4.3.1, I applied some pre-selections on the data. The flasher cut and muon veto are the same as nH analysis. The veto window for pool muon, AD muon and shower muon are 400, 800, and 1000 ms separately. Both of the 2 sub-events of a 2-fold event have energy cut as $0.3 \text{ MeV} < E < 12 \text{ MeV}$. The coincidence time window is $T_C = 1200 \mu\text{s}$ and the detector has a hardware time cut as $1 \mu\text{s}$. So the time interval Δt between the prompt and delayed signals of good 2-fold event candidates are $1 \mu\text{s} < \Delta t < 1200 \mu\text{s}$. An isolation cut is applied as well, to get the 2-fold event candidates $1200 \mu\text{s}$ away from any other events, similar as the nGd IBD analysis but with a wider gap. Besides, in a parallel study of the neutron calibration data, the isolation cut is extended into the muon veto window as that any event inside the muon veto window should be more than $1200 \mu\text{s}$ away from a good 2-fold event candidate, as shown in Fig. 4.5. This helps

to reduce the possible backgrounds induced by the cosmic muons. As a consequence of stricter cuts, the statistic of candidates after the latter cut is smaller than the former one, but with better signal/background ratio. In the end, the analysis results with these two different isolation cuts (called as cut A and B) are compared with each other and then combined.

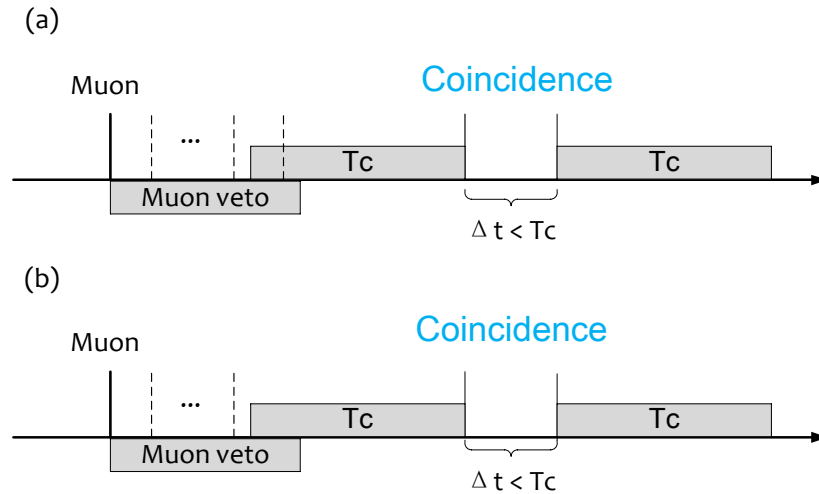


Figure 4.5 The isolation cut B is extended into the muon veto window. The dashed lines stand for vetoed events inside the muon veto window. By isolation cut B, case (a) is a bad candidate with a vetoed event less than $1200 \mu\text{s}$ to the first sub-event, which is abandoned; case (b) is a good candidate. If applying the isolation cut A, both case (a) and (b) would be kept as good candidates.

After the pre-selections above, the prompt energy cuts are applied to select specific group of events with high/low neutron kinetic energy, summarized in Table 4.3. For the AmC source, the prompt energy cut of 0.3-4 MeV will actually include some events with the ^{16}O in 1st excited state (E_{prompt} : 0-1 MeV) shown in Fig. 4.2(a), though most of the events come from the ground state. Since these two kinds of events are difficult to be separated by the prompt energy as shown in Fig. 4.7(d), I set this 0.3-4 MeV cut, to enlarge our statistic of the ground state events. It would not annoy our analysis too much if I applied the same cut to MC simulations, as our goal is to validate the data and MC agreement. The neutrons with different kinetic energy behave quite differently in the detector. Classifying the events into ground state events and excited state events can use more information about the neutron calibration, helping us to do the validation with more aspects. Mixing all events into one group (*i.e.*, no extra prompt energy cut) is also an option for validation, but less efficient.

Table 4.3 Prompt energy cut for events with different neutron kinetic energy. The energy of the possible γ produced in the events are also listed. The neutron kinetic energy transmitted to recoiled protons are heavily quenched, which determines the prompt energy range together with the γ rays.

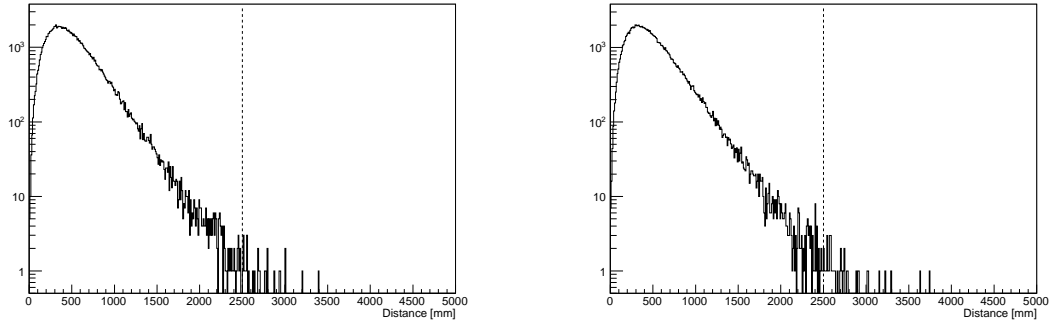
Events group	E_{prompt} cut [MeV]	Neutron kinetic energy [MeV]	γ energy [MeV]
AmC ground state	0.3-4	2.5-7.5 (small fraction < 0.8)	-
AmC excited state	5.5-7	< 0.8	6.1
AmBe ground state	1-4	4-10	-
AmBe excited state	4.2-7	0-5	4.4

The long coincidence time window of $1200 \mu\text{s}$ leads to an increase of the accidental backgrounds in the neutron signal candidates, as the main background. The reason to have such a long coincidence time window will be explained in Section 4.3.3.1. Some correlated backgrounds, such as IBD events, fast neutron events and ${}^9\text{Li}/{}^8\text{He}$ events, take very small fraction (less than 0.1%) in the total backgrounds.

4.3.3.1 Accidental Background Subtraction

The accidental backgrounds are made by the single radiation events and the neutron events with only one trigger within the coincidence time window by accident. The prompt and delayed spectra of accidental background should be symmetric, and very close to the spectrum of the singles (1-fold events). The main idea of accidental background subtraction (AccSub) is, using the singles spectrum to predict the accidental background spectra while using the prompt-delayed distance distributions for 2-fold events to predict the accidental background amount. The distribution of distance between the reconstructed vertices of the prompt and delayed signals from AmC and AmBe sources in MC are shown in Fig. 4.6. From MC simulations we knew that only very limited neutron events have distance above 2.5 m. So in the calibration data, nearly all the events with distance above 2.5 m are actually the accidental backgrounds. The whole process of accidental backgrounds subtraction is done as below:

- 1) Select the single events in calibration data and make pairs of the singles randomly;
- 2) Get distance distributions for 2-fold raw candidates (after pre-selections) and single pairs. Calculate a scale factor (A) for single pairs to subtract all the events with distance above 2.5 m in raw candidates;
- 3) Get prompt-delayed 2-dimensional spectra for raw candidates and single pairs. Use


 (a) AmC source in ACU-C, $z = -1.6$ m

 (b) AmBe source in ACU-C, $z = -1.6$ m

Figure 4.6 Distance distribution of neutron source in MC. The left figure is for the AmC source, in which only 0.03% of the events have distance greater than 2.5 m. The right figure is for the AmBe source, 0.04% of the events have distance greater than 2.5 m.

the same scale factor (A) to subtract the single pairs spectra from raw candidates spectra;

- 4) Apply the prompt energy cut in Table 4.3 and make projection of the 2-dimensional spectra along delayed energy axis to select specific groups of ground state events or excited state events.

Because of the existence of a common scale factor A for all energy bins, the uncertainties of the bins in the spectra are correlated to each other after the accident background subtraction. This feature is carefully handled in the later analysis.

Fig. 4.7 is an example of accidental background subtraction for AmC source calibration in ACU-B, $z = 0$ m. After accidental subtraction, the nC^* scattering peak (around 4.4 MeV) and ^{16}O second excited state peak (around 6.5 MeV) are obvious in the prompt spectrum. Only very limited accidental background residual from nGd events (around 8 MeV) can be seen. This indicates a good subtraction of the accidental backgrounds. The nH and nGd peaks are both very clear in the delayed spectrum. Similarly, Fig. 4.8 is an example of accidental background subtraction for AmBe source calibration at the same position of ACU-B, $z = 0$ m.

The purpose of setting such a long coincidence time window ($T_C = 1200 \mu s$, much longer than $200 \mu s$ in IBD selection) is to have a high enough selection efficiency for all the neutron events, including the nH events in liquid scintillator (LS) region (capture time constant about $210 \mu s$), as many of the calibration points are in ACU-B and ACU-C with a lot of LS nH events in data. A too short coincidence window would cut off more LS nH events than nGd events (about $30 \mu s$), biasing the nGd fraction. A lot of nH events would be separated by the coincidence window and mistaken as two single events, which are actually

correlated to each other. Under this condition, the accidental background spectrum would be not consistent with the singles' spectrum. Then the accidental background subtraction used in this study would fail. As shown in Fig. 4.9, in the center of the detector (ACU-A, $z = 0$ m), $T_C = 200 \mu s$ is enough for all events. Modification in coincidence window wouldn't change the singles' spectrum. At the boundary of the detector (ACU-C, $z = 0$ m), modification in coincidence window would obviously change the singles' spectrum. A long coincidence window $T_C = 1200 \mu s$ has a high enough selection efficiency for all neutron events. Then the single events are not correlated to each other, and our accidental background subtraction method works better.

4.3.3.2 Correlated Background Subtraction

Besides the events from neutron source, many other events such as IBD events and muon-induced events (fast neutron, ${}^9\text{Li}/{}^8\text{He}$ events) also make correlated 2-fold events in the detector. The delayed signal of IBD is also from the neutron capture, but they are nearly uniformly distributed in the detector, with a overall nGd/nH capture ratio about 1 : 1, learned from the IBD study. Nevertheless, the neutron source is deployed in a specific position in the detector with a localized nGd/nH ratio, which becomes very close to 0 when the source is put in ACU-C at the detector boundary. This difference leads the discrepancies of the delayed spectra between the IBD events and the neutron source events. Therefore, we do need to remove the IBD events to get rid of the bias in delayed spectra study. The fast neutron, ${}^9\text{Li}/{}^8\text{He}$ and other correlated background only take less than 0.1% of the IBD events, and are ignored in the background subtraction.

We can use the regular data (called as physics run, distinct from the calibration run) before and after the neutron calibration with the same pre-selections to estimate the amount of IBD backgrounds in the calibration data. The multiplicity efficiency caused by the isolation cut can be approximated as

$$\epsilon_{\text{multiplicity}} \sim e^{-(R_{\text{single}} + R_{\text{coincidence}}) \cdot (2T_C + \tau)}, \quad (4-7)$$

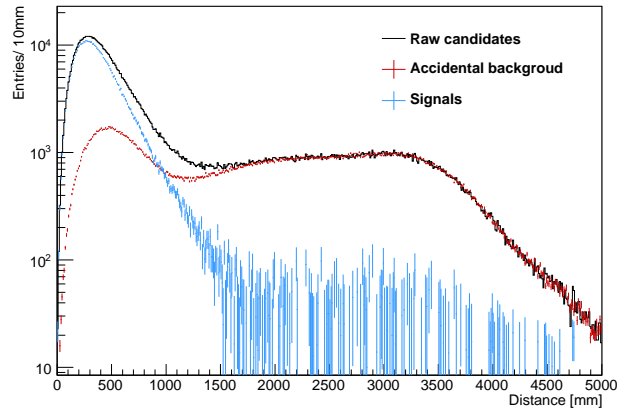
where $R_{\text{single}} + R_{\text{coincidence}}$ is the rate sum of single events and coincidence events, T_C is the coincidence time window (1200 μs), τ is the average neutron capture time. The events rates and average neutron capture time are both different for the physics run and calibration run. When we subtract the physics-run IBD spectra from the calibration-run neutron spectra, we need to do extra corrections for the multiplicity efficiency and livetime

(data taking time) , which reads as

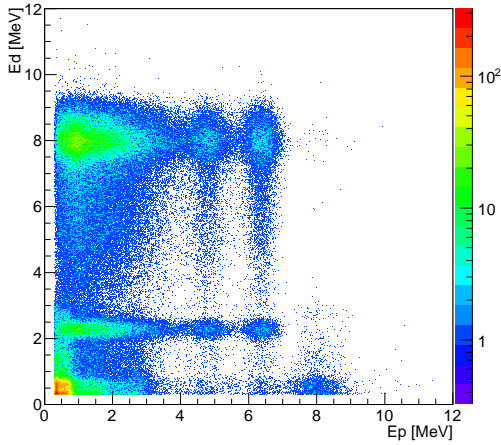
$$S_{IBDSub} = S_{AccSub} - S_{IBD} \frac{\text{livetime}_{\text{Calibration}} \cdot \epsilon_{\text{multiplicity}_{\text{Calibration}}}}{\text{livetime}_{\text{IBD}} \cdot \epsilon_{\text{multiplicity}_{\text{IBD}}}}, \quad (4-8)$$

where S_{AccSub} is the delayed spectrum after accidental background subtraction in calibration run; S_{IBD} is the delayed spectrum of nearby physics run after the same pre-selections, S_{IBDSub} is the delayed spectrum after correlated background (mainly IBD) subtraction. An example of the correlated background subtraction for AmC source in ACU-B, $z = 0$ m is illustrated in Fig. 4.10, which shows that the correlated backgrounds in the calibration neutron spectra is very limited. Thus I ignored the systematic uncertainty from the correlated backgrounds subtraction contributed to the neutron spectra.

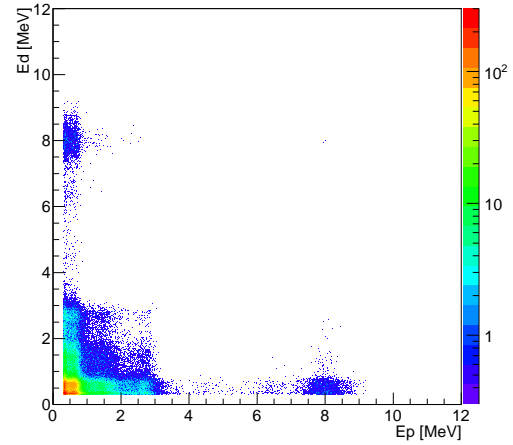
The neutron spectra with all the main backgrounds subtracted will be then used in the data and MC comparison.



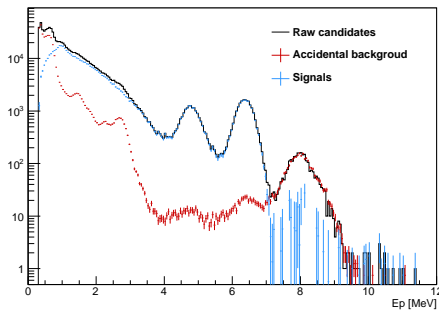
(a) prompt-delayed distance



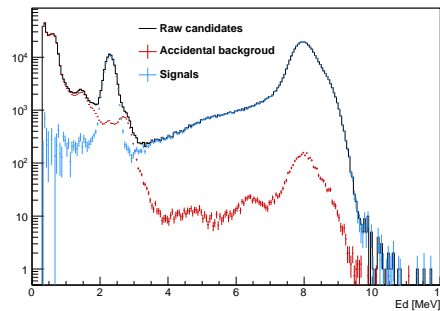
(b) prompt-delayed spectra of raw candidates



(c) prompt-delayed spectra of single pairs after scaling

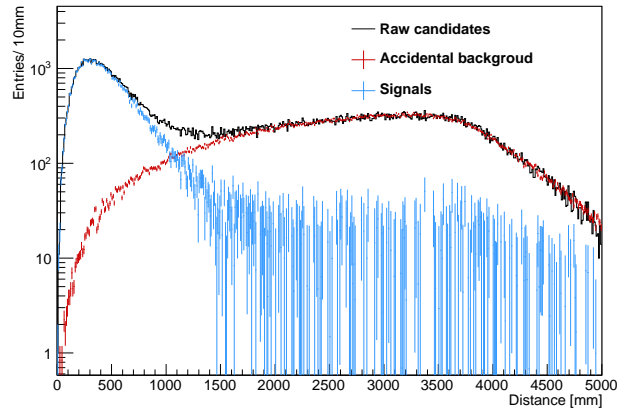


(d) prompt spectra

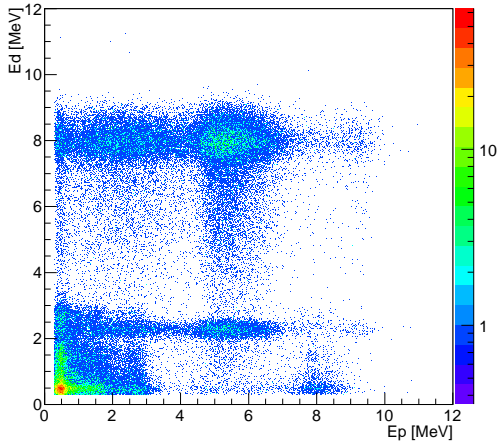


(e) delayed spectra

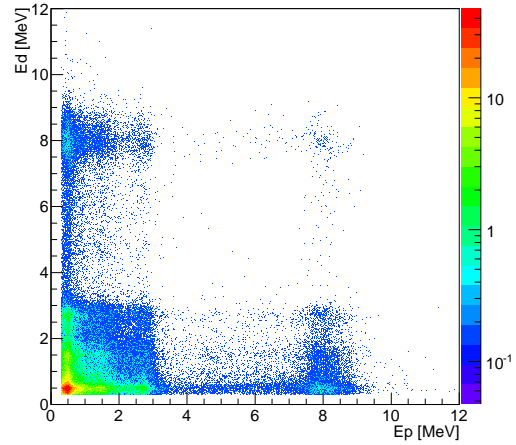
Figure 4.7 Accidental background subtraction of AmC in ACU-B, $Z=0$ m. The colored lines are for raw candidates (black), predicted accidental background (red) and signals (blue) respectively in (a) prompt-delayed distance distribution (d) prompt spectra and (e) delayed spectra. (b) and (c) are the 2-dimensional spectra of prompt and delayed energy for the raw candidates and accidental backgrounds.



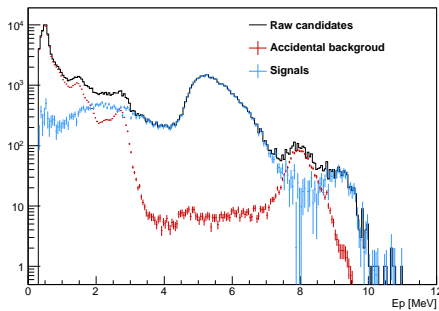
(a) prompt-delayed distance



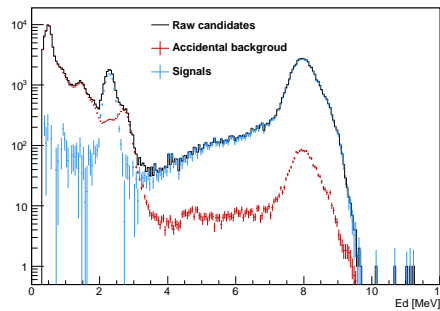
(b) prompt-delayed spectra of raw candidates



(c) prompt-delayed spectra of single pairs after scaling

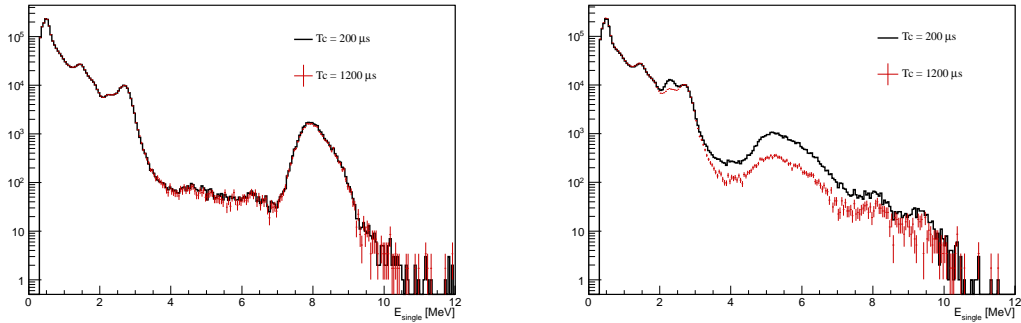


(d) prompt spectra



(e) delayed spectra

Figure 4.8 Accidental background subtraction of AmBe in ACU-B, $Z=0$ m. The colored lines are for raw candidates (black), predicted accidental background (red) and signals (blue) respectively in (a) prompt-delayed distance distribution (d) prompt spectra and (e) delayed spectra. (b) and (c) are the 2-dimensional spectra of prompt and delayed energy for the raw candidates and accidental backgrounds.



(a) Singles spectrum from AmBe source in ACU-A, $z = 0$ m.

(b) Singles spectrum from AmBe source in ACU-C, $z = 0$ m.

Figure 4.9 Comparison of singles spectra with long and short coincidence windows in the center/edge of the detector. The black solid lines stand for $T_C = 200\mu s$ and the red points stand for $T_C = 1200\mu s$. All spectra are normalized by total events number. The singles spectra with long and short coincidence window agree well in the center of the detector while an obvious discrepancy can be seen at the edge of the detector.

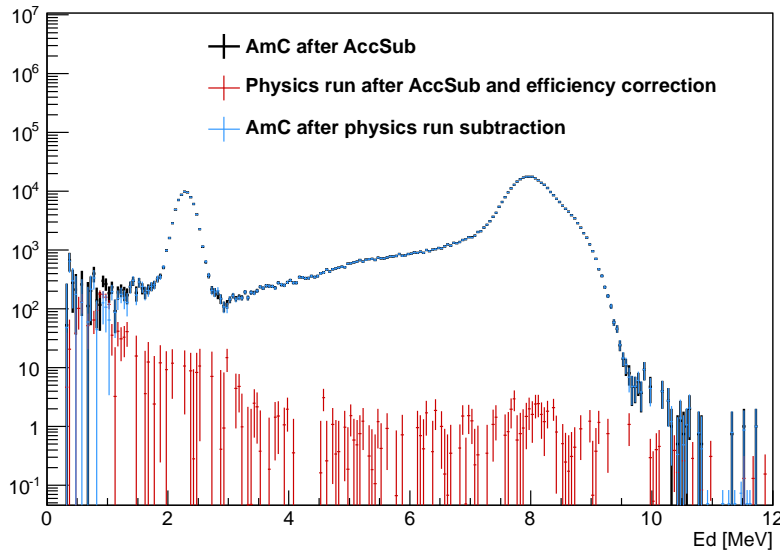


Figure 4.10 Correlated background (mainly IBD) subtraction for AmC in ACU-B, $z = 0$ m. The black points represent the neutron spectrum after accidental background subtraction; the red points are the small amount of effective IBD backgrounds, estimated from nearby physics run; the blue points show the neutron spectrum with all backgrounds subtracted.

4.4 Monte Carlo Simulation

4.4.1 Neutron Related Efficiency in MC

As I need to study the IBD delayed efficiency ϵ_D and its uncertainty with MC, a reliable MC is essential for the analysis. The MC simulation must be as close to real detector as possible. By definition of $\epsilon_D = N_{\text{Total,Gd,E}>6 \text{ MeV}}/N_{\text{GenInGdLS}}$, the IBD delayed efficiency is mostly sensitive to the physics processes of neutron propagation, de-excitation of nuclei after capturing neutrons, γ propagation and energy deposition in the detector. In the MC simulation, these processes depend on several factors:

Geometry The geometry is the basis of the detector, including the dimensions and materials. It would affect the propagation process of any particle in the detector, neutron, γ , optical photon, *etc.* In this way, it determines the nGd/nH ratio, the γ leakage and the spill-in effect.

Neutron scattering model What I call “neutron scattering model” is basically a model for the molecular bonds of the materials, which introduces extra effects for the scatterings as not only the target nucleus (*e.g.*, a proton) but also the molecule (*e.g.*, H₂ or H₂O) is recoiled. The neutron scattering model directly affects the neutron propagation process, including the neutron thermalization process and the neutron capture. This is related to the nGd/nH ratio and spill-in effect. The position where the neutron is captured is also the position where the γ starts. Then the neutron scattering model can somehow affect the γ leakage.

nGd de-excitation γ spectrum As the cross section depends on particle energy, the nGd de-excitation γ spectrum will strongly affect the γ propagation process and determine the γ leakage.

Energy model The energy reconstruction is a basic process of the signal analysis. It is related to everything about energy. So in our study of the IBD delayed efficiency which includes an energy cut, the energy model is very important. The energy model includes the energy non-linearity and energy non-uniformity. The energy non-linearity has been discussed in Chapter 3. The energy non-uniformity is studied with γ calibrations in different positions in the AD.

4.4.2 Implementation of MC

To have a precise simulation for the neutron physics processes, the new MC simulation is upgraded in the following five aspects compared with the previous version of Daya Bay MC:

- 1) Hydrogen mass fraction: The hydrogen mass fractions of the GdLS and LS were updated with three new measurements by different methods and groups. These would have some influence on the nGd/nH ratio. This modification in MC code is done by another Daya Bay collaborator of Liang Zhan.
- 2) Energy non-linearity (NL) and light yield: The nominal energy non-linearity model used in Daya Bay has been discussed in Chapter 3. The energy non-linearity model in the old MC had obvious differences from the nominal model. I changed the Birks' constant of electron/ γ /positron (from $6.5 \times 10^{-3} \text{g}/(\text{cm}^2 \cdot \text{MeV})$ to $15.8 \times 10^{-3} \text{g}/(\text{cm}^2 \cdot \text{MeV})$) for the scintillator quenching effect and reduced the Cerenkov light yield, to make the MC energy non-linearity model as consistent with data nominal model as possible. After changing the non-linearity model, I modified the total light yield correspondingly, to retain the same energy resolution.
- 3) Calibration pipe geometry: The calibration pipe is the part used to fill the IAV/OAV with scintillator, and to put the calibration sources in ACU-A/B/C into the detector, shown in Fig. 2.6(b). It connects the acrylic vessels and the overflow tank. Each calibration pipe is a Teflon bellows. To ensure the sealability, there are many small components, such as clamps and sleeves, fixing the Teflon bellows. In the old MC, many of these structures are simplified and the Teflon bellows uses the same optical properties of acrylic, making it transparent to optical photons. These make the neutron spectrum of calibration source deployed near the calibration pipe in MC quite different from data. I made the structures more realistic and changed the absorption length of optical photon in Teflon, making it translucent. The modification is only done for the central calibration pipe, ACU-A, at present.
- 4) More neutron scattering models: the neutron scatterings in the detector mainly come from the protons. I involved more molecular bonds models for the protons in the liquid scintillator and in the acrylic.
- 5) More nGd de-excitation γ spectrum models: the de-excitation after gadolinium capturing neutron can emit different numbers of γ 's with so many branches. I adopted more measured nGd spectrum models to investigate the overall detector

response for the nGd events.

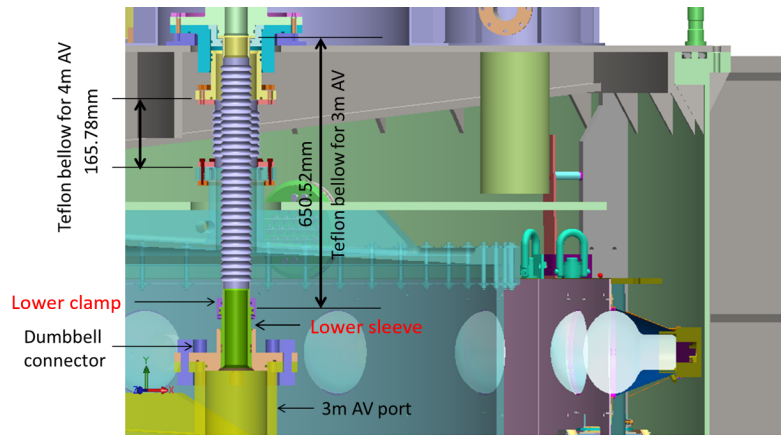
These five aspects are the common upgrade of the MC, applied for all simulations of IBD and radioactivities in the detector. For the new neutron calibration simulation, more modifications are done. I have new neutron sources generators and geometry implementations in MC, as I used new neutron sources in the new calibration campaign different from the previous ones.

The energy non-linearity model in Daya Bay and the implementation in simulation has been discussed in the Chapter 3 and now I have a good agreement between the nominal model from data and the MC simulation. In the following sections, I will present the details of the MC improvements of calibration pipe geometry, and the import of more neutron scattering models and gadolinium de-excitation γ spectra.

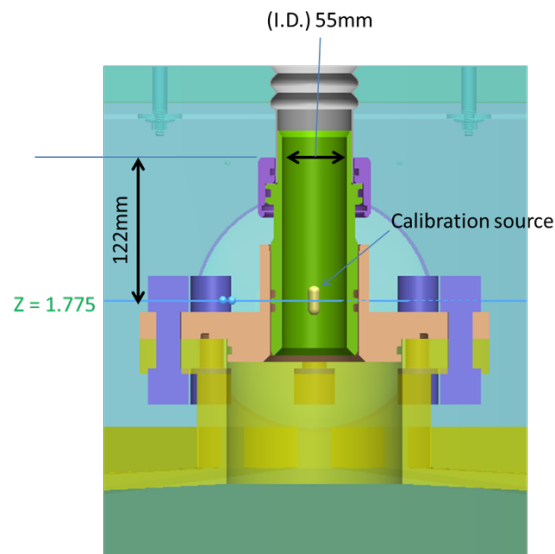
4.4.2.1 Calibration Pipe Geometry in MC

The calibration pipe geometry problem was first found in the PuC source delayed spectrum study. For the PuC source calibration in ACU-A at $z = 1.775$ m, the source is actually deployed in the calibration pipe. The technical design plot and a zoom-in for the calibration pipe are shown in Fig. 4.11. In the old MC, there are three main differences from the technical design. Firstly, many of the connecting structures, such as the lower clamp and lower sleeve, are simplified. Secondly, the Teflon bellows is longer than the design, and it uses the same optical properties of acrylic, making it transparent to optical photons. Thirdly, the IAV port is not fully filled with GdLS: some part inside the IAV port is empty. These make the delayed spectrum of PuC source calibration quite different from the old MC, as shown in Fig. 4.12. The nGd peak in the calibration data spectrum is much flatter than the old MC, with more leakage.

We changed the geometry of the calibration pipe in ACU-A strictly following the technical design. The simplified structures are back. The Teflon bellows are set to be translucent to the optical photon. The absorption length is set as 1 mm for all optical photons regardless of wavelength. The GdLS filled volume is corrected. I have 2 photos for the calibration pipe in Fig. 4.13. From these photos we can clearly see that the Teflon bellows is translucent, not as transparent as the acrylic. The absorption length of optical photon in Teflon is determined after a scan for the absorption length. I changed the absorption length of optical photon in Teflon from 0.001 mm to 8000 mm, as shown in Fig. 4.14. When the absorption length is smaller, more optical photon from scintillation



(a) Technical design of the calibration pipe.



(b) Zoom-in for the IAV port connecting with calibration pipe.

Figure 4.11 Technical design of the calibration pipe. Figures from Qiang Xiao in Daya Bay collaboration.

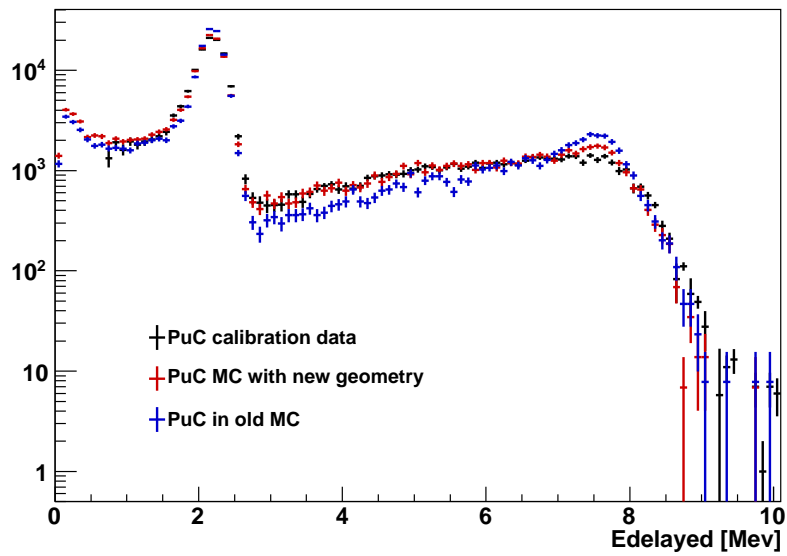
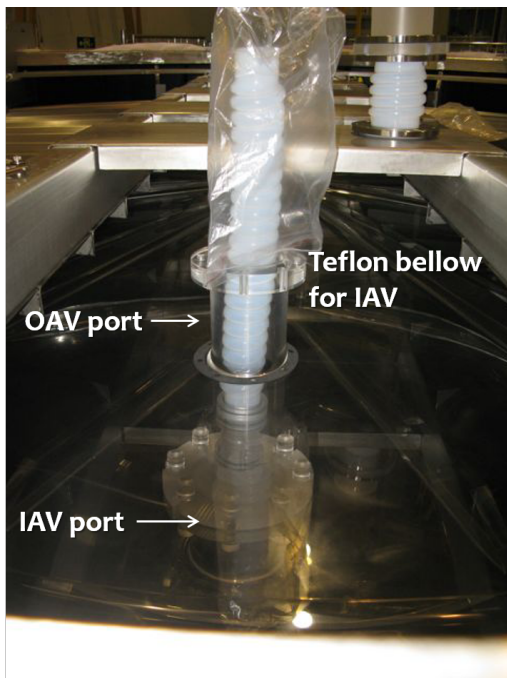
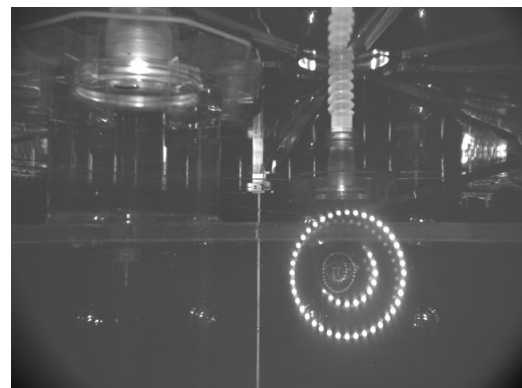


Figure 4.12 Delayed spectrum comparison for PuC in ACU-A, $z = 1.775$ m: black for data, blue for old MC and red for the MC with new geometry.



(a) Photo for the calibration pipe before installing the detector.



(b) Photo by camera inside the detector. The halo is from the LED light used in calibration.

Figure 4.13 Photos of the calibration pipe. Photos provided by Jeff Cherwinka in Daya Bay collaboration.

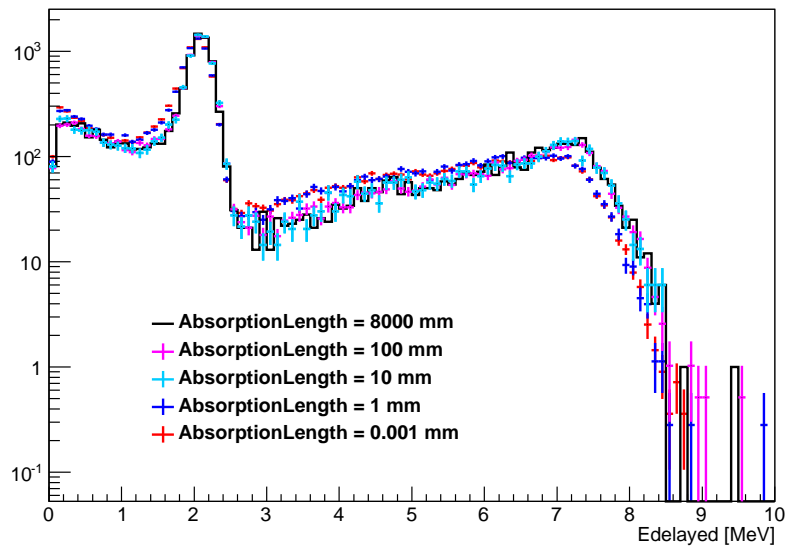


Figure 4.14 Delayed spectrum comparison for different absorption length of optical photon in Teflon.

or Cerenkov radiation would be absorbed inside Teflon. These energy are not visible to the detector as no optical photon reaches the PMT, leading to some leakage. The cases with absorption length smaller than 1 mm are much alike, and the tail shape is closer to the calibration data. The thickness of the Teflon bellows is 1 mm, comparable with the absorption length. So after this modification, the Teflon bellows is translucent in MC. The whole modification for geometry is shown in Fig. 4.15. The delayed spectrum in the upgraded MC agrees with calibration data much better than the old MC, as shown in Fig. 4.12.

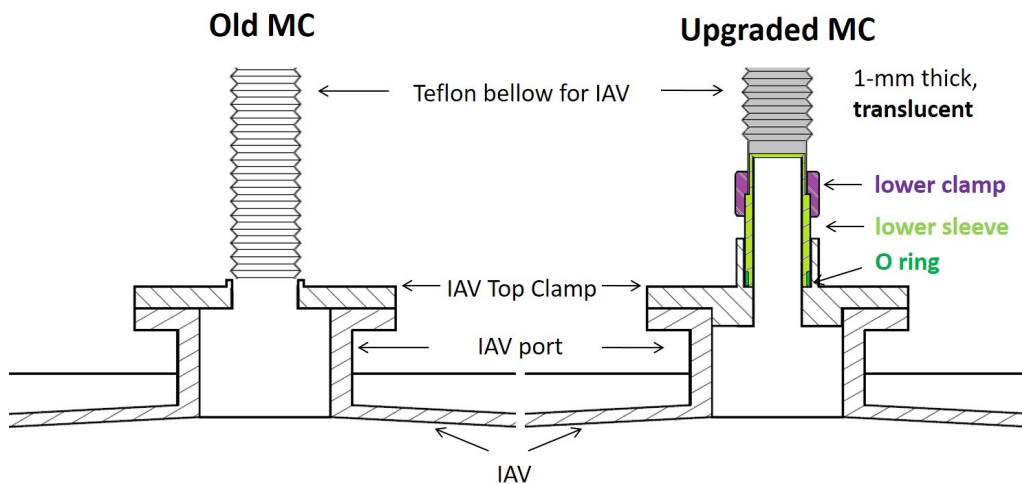


Figure 4.15 Calibration pipe geometry in old MC and upgraded MC.

We have several plots to confirm our modification in the MC. Fig. 4.16 shows the IAV port structure in the old MC and upgraded MC. After the modification, the structure of lower sleeve and lower clamp can be seen clearly. Fig. 4.17 shows the volume filled

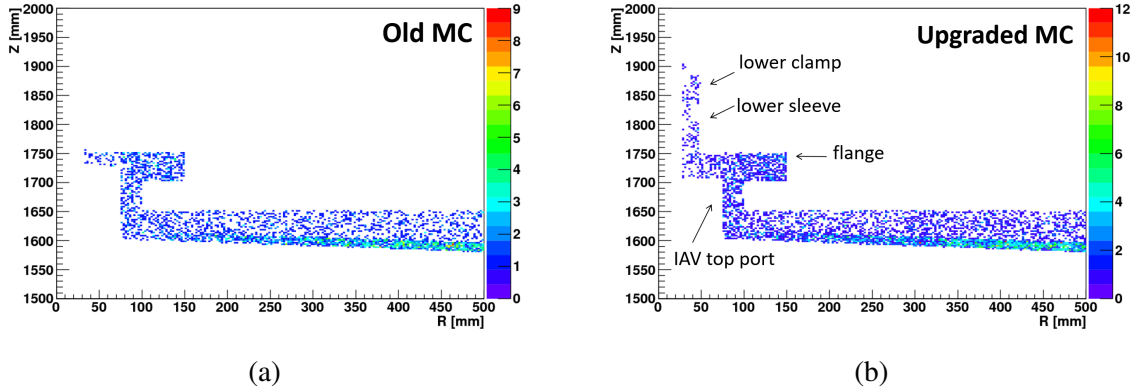


Figure 4.16 The IAV port structure in old MC (a) and upgraded MC (b). The plots show the true vertices of events generated in the acrylic material.

with GdLS in the old MC and upgraded MC. The modification can be seen by comparing the 2 figures, especially the bottom part of the IAV port connecting the calibration pipe. This modification is important for neutron calibration delayed spectrum study at the top of the detector as it would change the nGd/nH ratio.

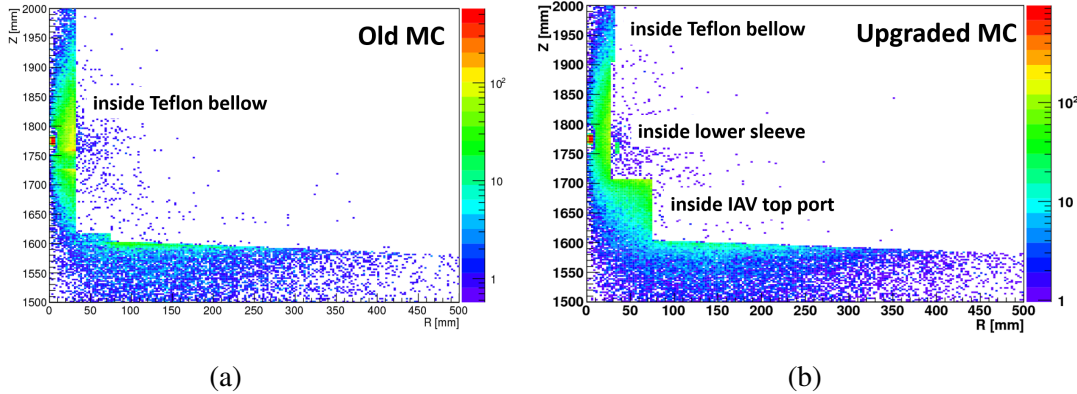


Figure 4.17 The volume filled with GdLS in old MC (a) and upgraded MC (b). The plots show the true vertices where the neutrons are captured for nGd events.

4.4.2.2 Neutron Scattering Models in MC

The IBD delayed efficiency is mostly sensitive to the neutron propagation process, nGd de-excitation γ spectra, γ propagation process in the detector. The neutron scattering models and nGd de-excitation γ models play important role in these processes. What I

call “neutron scattering model” is basically a model for the molecular bonds for hydrogen (proton) in the materials. The neutron is thermalized mainly via the scattering with protons, and these models provide scattering cross-section angular distribution including the impact from the molecular bonds for protons. Compared with the scattering of high energy neutron, the scattering of the thermal neutron ($E_K \lesssim 1$ eV) is more likely to be affected by the molecular bond.

In this study, I only discussed the models for the thermal neutron scattering. The thermal neutron models in Geant4 are adopted mainly from the ENDF database^[120]. However, for the materials in Daya Bay AD, such as the LAB-based liquid scintillator ($\text{CH}_{-1.7}$) and acrylic ($\text{C}_5\text{O}_2\text{H}_8$), the experimental data are incomplete. Thus I can only use the existing models of water (H_2O), polyethylene (CH_2 , poly for short) and hydrogen free-gas (H_2) to approximately simulate the thermal neutron scattering in the AD materials.

In the MC, we can set various kinds of neutron scattering model (water model, poly model, and free-gas model) for the neutron scattering in one material, and the neutron scattering model inside the liquid scintillator and acrylic could be different. In this study, our MC simulations covered five neutron scattering model combinations (neutron model in scintillator and neutron model in acrylic):

- a) water, free-gas (default in the old MC)
- b) water, poly
- c) poly, poly
- d) poly, free-gas
- e) free-gas, free-gas

4.4.2.3 nGd De-excitation γ Models in MC

After thermalization by scattering, the neutron is captured by gadolinium, hydrogen, or other nuclei, from both IBD and the neutron source. The nH events have a single 2.2 MeV γ , which is very simple. For the nGd events, the different isotopes of gadolinium (in our experiment, mainly ^{155}Gd and ^{157}Gd) have different total energy released. For a giving isotope of gadolinium, the nuclei after capturing neutron can emit several γ 's via various channels while the average γ energy is about 2.1 MeV. The different γ spectra would lead to totally different propagation processes and leakage, affecting the detected spectra. In the MC, we can set different nGd de-excitation γ spectrum models:

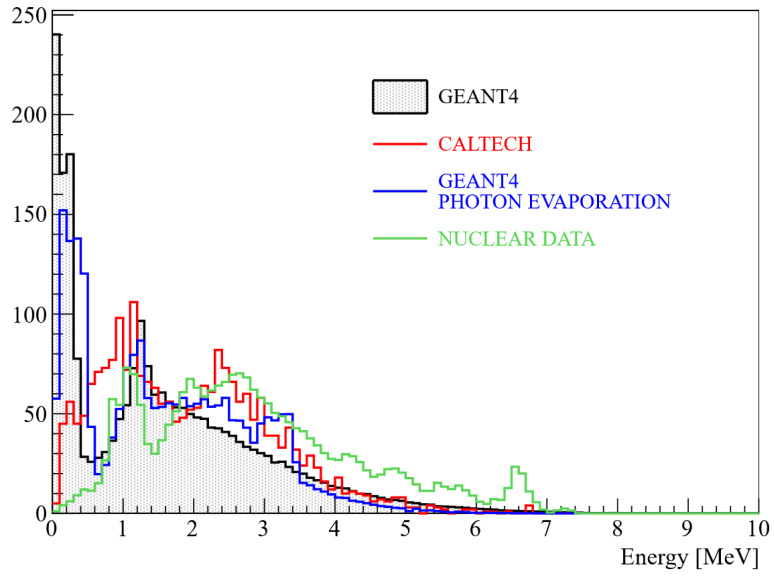
- 1) Geant4 model: the default spectrum in Geant4 (referred to as “g4”, also the default

- model in the old MC),
- 2) Caltech model: a spectrum from a measurement conducted at Caltech (referred to as “Caltech”)
 - 3) Geant4 default model with “photon evaporation” process: this is adopted from the ENSDF (Evaluated Nuclear Structure Data File) database^[121] (referred to as “g4eva”)
 - 4) Nuclear Data model: a model from 1968 Nuclear Data Sheets^[122] (used in the simulation for the first oscillation result of Daya Bay^[24], but replaced by Geant4 model in the later studies. In this study, I will directly abandon it due to the too bad performance).

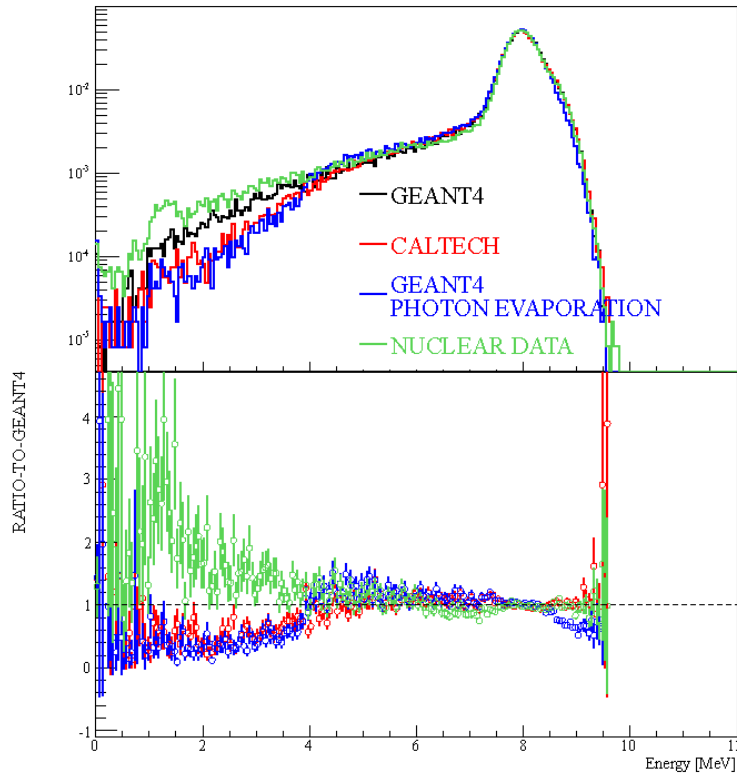
Fig. 4.18 shows the original γ spectra of neutron capture on ^{155}Gd and reconstructed nGd spectra ($^{155}\text{Gd}+^{157}\text{Gd}$) of IBD events for different nGd de-excitation γ models. From Fig. 4.18 we can see that the nGd de-excitation γ model from Nuclear Data Sheets have big discrepancy with other three models, especially in tail of the low energy region, which is very crucial for our IBD delayed efficiency study. So I decided to abandon it and only use the other three nGd de-excitation γ models.

After removing the nGd de-excitation γ model from Nuclear Data Sheets, I have 5 neutron scattering models \times 3 nGd de-excitation γ models (15 model combinations) in total. In the old MC, the “water_free-gas” model was used for neutron scattering and “g4” model was used for γ spectrum. In this section and hereafter, it would be denoted as the “g4_water_free-gas” model. Denotations of the other models are similar to this example. The delayed spectrum of all IBD events (nearly uniformly distributed in the detector) in new MC with the default models in old MC are shown in Fig. 4.19. The energy scale, non-linearity and non-uniformity are optimized for IBD of the default model in MC. For other models, an extra energy scale correction may be applied to align the nGd peaks with the true values (7.94 MeV for ^{157}Gd capture and 8.54 MeV for ^{155}Gd capture). I generated IBD samples with all these 15 set of MC models.

For the neutron calibration, I have simulations for AmC and AmBe sources at various positions, the same as the calibration data. Because of the energy non-uniformity, the calibration at different positions with different models all have their own energy scale to make the data and MC as consistent as possible. With these various kinds of neutron scattering models and nGd de-excitation γ models, I hope our MC simulations can successfully cover the real situation in the detector. This needs to be validated with data.



(a) De-excitation γ spectra of neutron capture on ^{155}Gd .



(b) Reconstructed nGd tail of IBD events.

Figure 4.18 Comparison of different de-excitation γ models. Figures from Wenqiang Gu in Daya Bay collaboration.

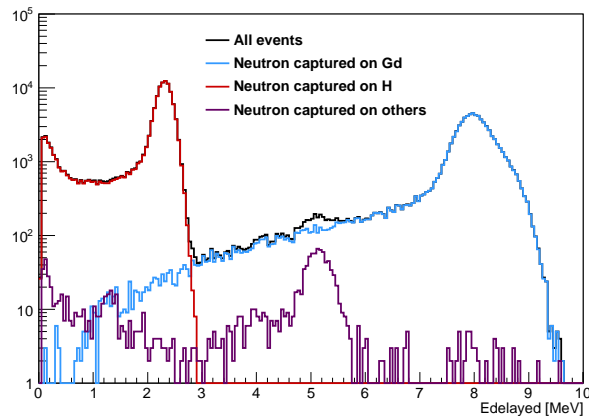


Figure 4.19 Delayed spectrum in new MC: black for all events; blue for nGd events; red for nH events; purple for the other events.

If the data and MC simulations have very good agreement, then I can study the IBD delayed efficiency with these reliable MC simulations and assign a reasonable uncertainty for it.

4.4.2.4 Comparison Between Data And MC

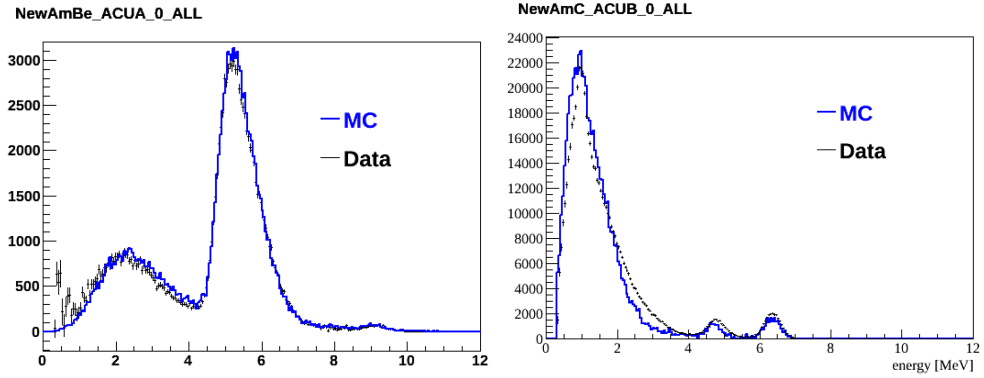
Once I had both the data and MC simulations, I compared them to check their agreement, from the following respects of energy spectra and distance distribution.

Prompt Energy Spectrum

First I checked the energy spectra of the prompt signal in data and MC for both neutron sources, as shown in Fig. 4.20. I changed the Birks' constant for electron/ γ /positron in MC while I kept that for proton as the value from direct measurement. The data and MC performance are almost consistent with some small mismatch for the tail. This indicates that our simulation for the proton quenching effect agrees with the real detector.

Delayed Energy Spectrum

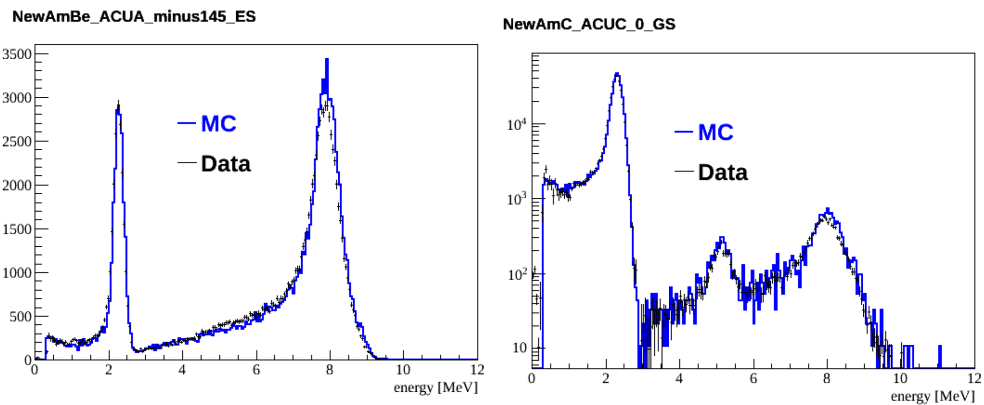
We also compared the energy spectra of the delayed signals from neutron. This is what I care about most. The result for two typical calibration points are show in Fig. 4.21, where good agreement can be seen. Actually the calibration point of ACU-A, $z = -1.45$ m is a relative bad point for the agreement between the data and MC, probably due to some possible geometry issue. The other calibration points have even better performance for the agreement check.



(a) AmBe GS+ES events in ACU-A,
 $z = 0$ m.

(b) AmC GS+ES events in ACU-B,
 $z = 0$ m.

Figure 4.20 Comparison of the prompt-energy spectra between data and “g4_water_poly” model MC. Left is for all AmBe events in the AD center. Right is for all AmC events in ACU-B, $z = 0$ m.



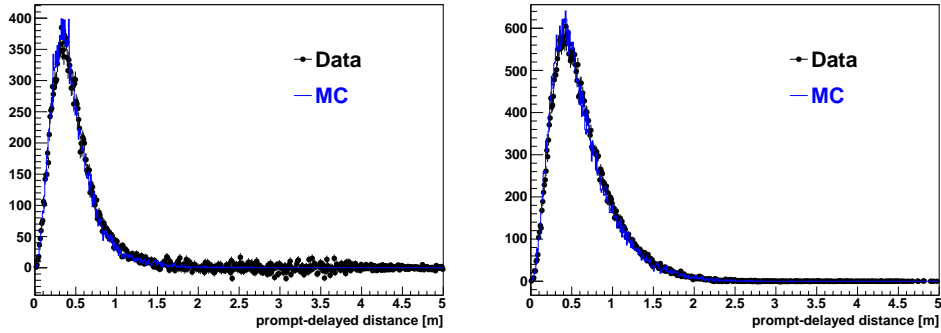
(a) AmBe GS+ES events in ACU-A,
 $z = 0$ m.

(b) AmC GS+ES events in ACU-B,
 $z = 0$ m.

Figure 4.21 Comparison of the delayed-energy spectra between data and “g4_water_poly” model MC. Left is for AmBe ES events in ACU-A, $z = -1.45$ m. Right is for AmC GS events in ACU-B, $z = 0$ m.

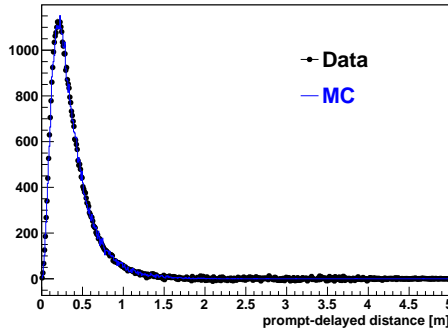
Prompt-Delayed Distance Distribution

Fig. 4.22 show the distance distribution comparison between data and MC for three typical calibration points. From the figures we can find that the data and MC have good agreement for the distance distribution. Comparing the Fig. 4.22 (a) and (b), we can



(a) AmBe GS events in ACU-A, $z = 0$ m.

(b) AmBe ES events in ACU-A, $z = 0$ m.

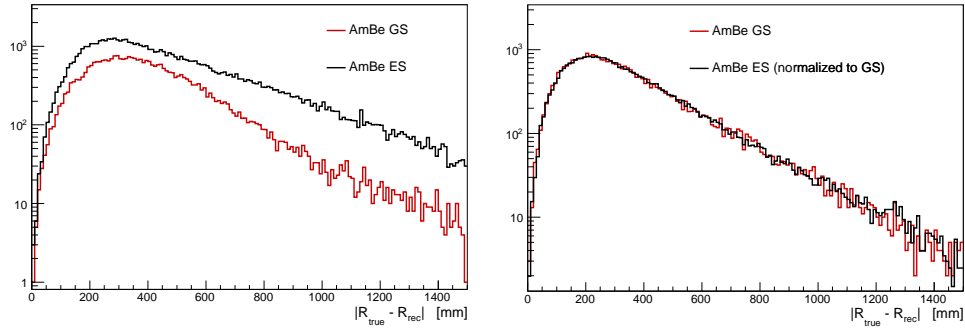


(c) AmC GS events in ACU-C, $z = 0$ m.

Figure 4.22 Prompt-delayed events distance distribution comparison between data and MC: the black points for data and the blue line for MC. Good agreement can be seen both for the AD center and AD boundary.

see that the excited state events even have a longer prompt-delayed distance than ground state events with the reconstructed vertices. This is contrary to our expectation, as I have emphasized that the neutrons in GS events will have larger kinetic energy thus travel further in the detector, compared with the neutrons in ES events. This anomaly is caused by the deviation of the reconstructed vertex from the true vertex, especially for the γ signals. The vertices reconstruction is highly smeared by the γ propagation process.

As shown in Fig. 4.23(a), the deviation of vertex reconstruction for the prompt signals of ES events with smaller neutron kinetic energy is bigger than the GS events.



(a) Prompt signals.

(b) Delayed signals.

Figure 4.23 Deviation of the reconstructed vertex from the true vertex for AmBe source in detector center: (a) for prompt signals and (b) for the delayed signals. The red line is for the GS events while the black line is for the ES events. The black line in (b) is normalized to the red line, to compare the shape. The areas under line are different due to the branch ratio difference of GS and ES.

This is because that the prompt signal of ES events are mainly from γ 's while that for GS events are mainly from proton recoil. In Fig. 4.23(b), as the delayed signals of GS events and ES events are both the same neutron capture signals, the vertex reconstruction deviation for delayed signals are consistent. So we can know that for AmBe source, the ES events have bigger vertices reconstruction smearing. This leads to the result in Fig. 4.22 for reconstructed vertices.

In conclusion, this prompt-delayed events distance distribution check shows that our data and MC have good agreement for the neutron propagation process.

4.5 IBD Detection Efficiency and Uncertainty

As introduced in Section 4.2, I combine the Gd capture fraction, nGd detection efficiency and spill-in correction as IBD delayed efficiency in the IBD detection efficiency calculation. The IBD delayed efficiency is highly sensitive to the neutron propagation process, nGd de-excitation γ spectra, γ propagation process in the detector. I need to estimate the IBD delayed efficiency from MC simulation, so I do need to ensure our MC simulation is reliable in these aspects.

4.5.1 Comparison Between Data and MC

To use the neutron calibration delayed spectrum as shown in Fig. 4.10, a fraction of nGd peak (FGd) is defined for the delayed spectrum as

$$\begin{aligned} \text{FGd} &= N_{6 \text{ MeV} < E < 12 \text{ MeV}} / N_{1.5 \text{ MeV} < E < 12 \text{ MeV}} \\ \epsilon_D &= N_{\text{Total, Gd, } E > 6 \text{ MeV}} / N_{\text{GenInGdLS}} . \end{aligned} \quad (4-9)$$

From definition, the FGd has some similarity to the IBD delayed efficiency (ϵ_D). The numerator of FGd is the nGd events number with a 6 MeV cut, while the denominator of FGd is the sum of nH events and nGd events, excluding some of the tails. The cutoff at 1.5 MeV is to remove the possible contamination of bismuth events, though they are very limited in the new neutron calibration with a high neutron rate. So we know that this FGd is sensitive to the Gd capture fraction, nGd detection efficiency (nGd peak to tail ratio) and also the spill-in correction, the same as the IBD delayed efficiency. We can first compare FGd for the calibration data and MC to check the agreement.

The FGd value for every neutron calibration point can be easily calculated with the delayed spectrum after background subtraction following the definition. The uncertainty calculation with the systematic uncertainty from background subtraction is a little tricky. Because I used a scale factor for the whole background spectrum in the accidental background subtraction (AccSub) for the neutron calibration data, as discussed in the Section 4.3.3.1, the uncertainties for the energy bins after AccSub are correlated to each other. When I calculate the integral of a given energy region of the spectrum after AccSub, this correlation should be carefully handled with. A precise calculation for this systematic uncertainty in the FGd evaluation is formulated in detail in the Appendix A.

For the correlated background (mainly IBD events) subtraction, the process is similar while the correlated background is much less than the accidental background. The systematic uncertainty for correlated background subtraction comes from the multiplicity efficiency correction and livetime correction (just like the scale factor in accidental background subtraction) in equation (4-8). The livetime was measured in a precision better than 1×10^{-6} , hence the systematic uncertainty from livetime is found to be negligible in the calculation. The multiplicity efficiency is related to the neutron source events rate as shown in equation (4-7). I changed the rate estimation for a wide range (as large as 100%) in the multiplicity efficiency correction calculation and regarded the variances in FGd as the systematic uncertainty for the correlated background subtraction, which should be

quite conservative.

Table 4.4 is an example of FGd and uncertainty calculation for AmBe ground state events at five positions in ACU-A. From the table we can find the systematic uncertainty from accidental background subtraction and correlated background subtraction are negligible compared with the statistic uncertainty. The correlated background has very limited impact on the FGd value. The situation of the other neutron calibration points are similar to this result. The statistic uncertainty dominates in the FGd total uncertainty.

Table 4.4 FGd and uncertainty calculation for AmBe ground state events in ACU-A. FGd_{AccSub} is the FGd value after accidental subtraction. FGd_{IBDSub} is the FGd value after correlated background subtraction. $\sigma_{AccSub}(syst.)$ is the systematic uncertainty from accidental subtraction. $\sigma_{IBDSub}(syst.)$ is the systematic uncertainty from correlated background subtraction.

z position [m]	FGd_{AccSub} [%]	FGd_{IBDSub} [%]	σ [%]	$\sigma(stat.)$ [%]	$\sigma_{AccSub}(syst.)$ [%]	$\sigma_{IBDSub}(syst.)$ [%]
-1.45	63.78	63.78	0.21	0.21	0.02	2×10^{-6}
-0.75	84.36	84.39	0.23	0.23	0.03	8×10^{-4}
0	84.82	84.84	0.27	0.27	0.04	8×10^{-4}
0.75	84.53	84.55	0.23	0.22	0.03	8×10^{-4}
1.5	68.56	68.56	0.24	0.24	0.02	2×10^{-4}

4.5.2 Neutron Detection Efficiency

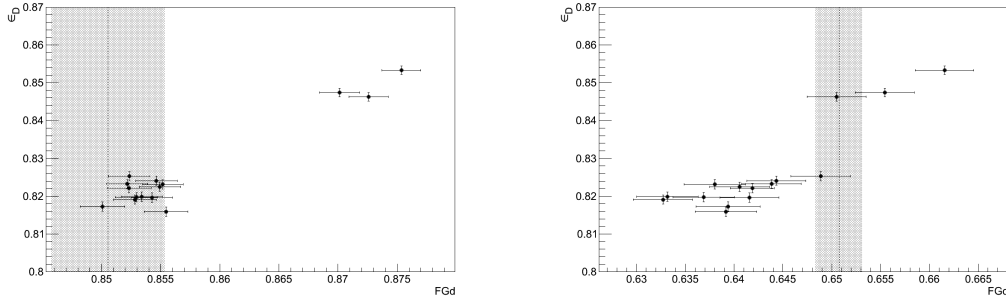
4.5.2.1 Constructing a χ^2 to find the best MC model

By now I have totally 59 calibrations of different position-source. I also have totally 15 different models of MC. I calculated the FGd value for data and MC simulations. The question is how I can estimate the IBD delayed efficiency and uncertainty from these FGd values. First I need to estimate the efficiency central value. A simple idea is to find the MC simulation which is the most consistent with data. So I constructed a χ^2 to evaluate the agreement of data and every version of MC as

$$\chi_j^2 = \sum_{i=1}^{59} \frac{(FGd_{Data,i} - FGd_{MC,i})^2}{\sigma_{Data,i}^2 + \sigma_{MC,i}^2}, \quad (4-10)$$

where j is the given version MC of one model. We can loop over the 15 different MC models and minimize the χ^2 to find the best version of MC. Then we can get the IBD

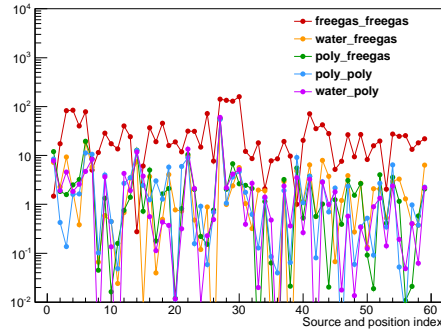
delayed efficiency from the best MC IBD simulation.



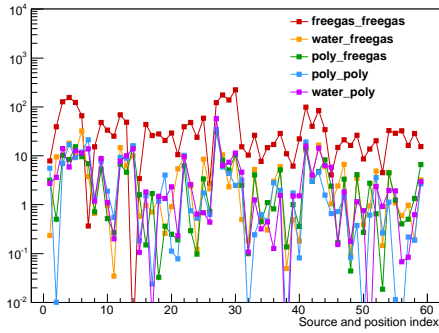
(a) AmBe ground state events at ACU-A, $z = 0$ m. (b) AmC ground state events at ACU-B, $z = -1.45$ m.

Figure 4.24 FGd and IBD delayed efficiency for data and different models. The x axis is the FGd value while the y axis is the IBD delayed efficiency ϵ_D . The gray region represents the FGd and uncertainty band obtained from calibration data.

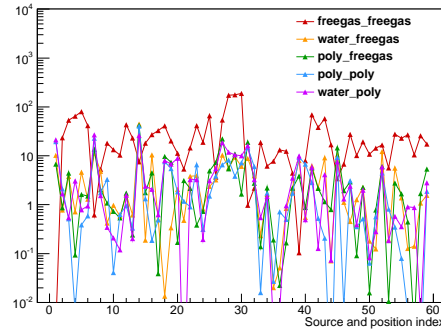
Fig. 4.24 are examples of two calibration points. The three data points with higher FGd and IBD delayed efficiency (ϵ_D) in the figure are from the three models with “free-gas_free-gas” model for neutron scattering. For total 59 calibrations, these three models always have bigger FGd values. For most of the calibrations, the data FGd value is closer to the rest 12 models, like the situation of AmBe ground state events at ACU-A, $z = 0$ m. In this case, the χ^2 for the three “free-gas_free-gas” models are very big, while other 12 models have small χ^2 . For some calibrations (especially in the bottom part of the detector, where our MC geometry may have some small issue), the data FGd value is closer to the three “free-gas_free-gas” models. In this case, the χ^2 for the three “free-gas_free-gas” models would be smaller than the rest 12 models. The χ^2 contribution from each calibration point and each MC version are shown in Fig. 4.25. Generally, the “free-gas_free-gas” models have higher χ^2 than other models. The χ^2 for each model is shown in Table 4.5, together with the IBD delayed efficiency. In all MC simulations, the statistic uncertainties of IBD delayed efficiency are all about 0.12%. From Table 4.5, the χ^2 of the three “free-gas_free-gas” models are much larger than the rest models. They are greater than 1500 for 59 calibration points, indicating that the discrepancies between data and these models are too big. Besides, the IBD delayed efficiencies from these models are about 2% larger than others. So I would abandon these models when considering the MC parameter space as they are too far away from the real situation. The best MC model is the “g4_water_poly” model with the smallest χ^2 of 176. The central value of IBD delayed efficiency from this best MC is 81.75%. For all 12 good MC models, the IBD delayed



(a) χ^2 for five models with g4 neutron model γ model.



(b) χ^2 for five models with caltech neutron model γ model.



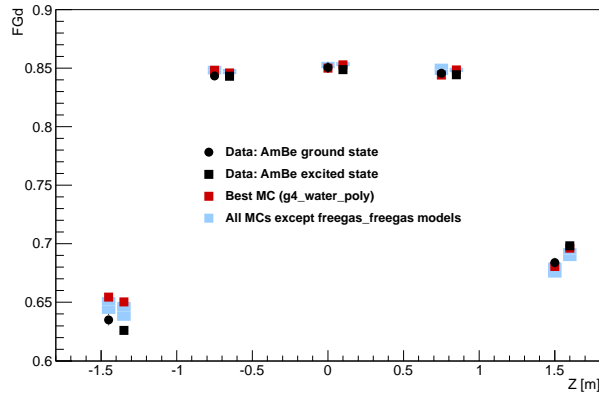
(c) χ^2 for five models with g4eva neutron modely model.

Figure 4.25 χ^2 contribution from each calibration point and each MC version.

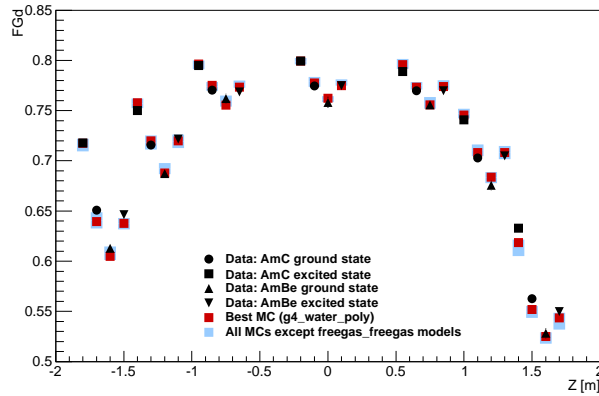
efficiency varies from 81.61% to 82.55%, and the MC fluctuation is 0.12%.

4.5.2.2 Estimation for IBD Delayed Efficiency Central Value

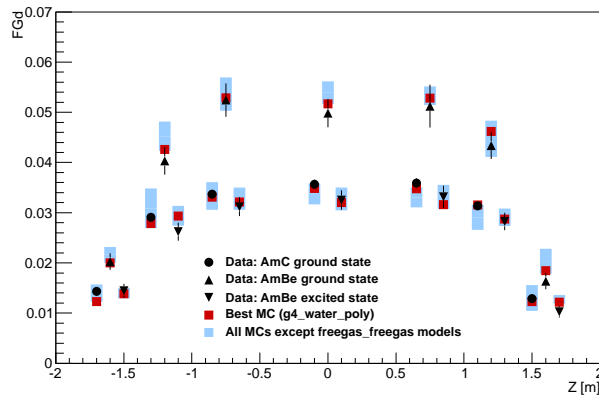
After removing the three “free-gas_free-gas” models, I compared the FGd of calibration data and the rest 12 MC models, as shown in Fig. 4.26. From Fig. 4.26 we can find that for most of the calibration points, the data value floats inside the MCs fluctuation, and the difference between data and the best MC is small compared with the spread of all MC values. From ACU-A to ACU-C, the FGd varies in a wide range, from 1% to 85%. Though the process of neutron propagation and capture change so much for different points, the data can still have a good agreement with the MCs. This indicates our data and MCs should also have a good agreement for the IBD delayed efficiency, as FGd and the IBD delayed efficiency are highly correlated to each other. Then we can use the central value from the best MC to estimate the IBD delayed efficiency. The FGd comparison between data and 12 good MC models in all calibration points are put together in the



(a) FGd comparison among data and MCs in ACU-A.



(b) FGd comparison among data and MCs in ACU-B.



(c) FGd comparison among data and MCs in ACU-C.

Figure 4.26 FGd comparison among data and 12 good MC models for the 59 calibration points. In each plot, the black markers are the data points; the red squares are the FGd values from the best MC; the blue rectangle shows the range of FGd values of all MCs.

Table 4.5 χ^2 and IBD delayed efficiency for each model. Statistic uncertainty for IBD delayed efficiency in MC is 0.12%.

MC model	χ^2	IBD delayed efficiency
g4_free-gas_free-gas	1858	84.76
g4_water_free-gas	205	82.23
g4_poly_free-gas	200	82.01
g4_poly_poly	195	81.61
g4_water_poly	176	81.75
caltech_free-gas_free-gas	2455	85.37
caltech_water_free-gas	299	82.55
caltech_poly_free-gas	231	82.36
caltech_poly_poly	238	82.00
caltech_water_poly	284	82.43
g4eva_free-gas_free-gas	1783	84.65
g4eva_water_free-gas	228	82.35
g4eva_poly_free-gas	242	82.28
g4eva_poly_poly	217	82.00
g4eva_water_poly	252	81.93

Fig. 4.27, and the differences are also illustrated. The calibration points of ACU-A, $z = -1.45$ m for AmBe GS and ES events have big discrepancy of 2% between data and MC, probably due to some geometry issue. Similar situation for the calibration points of ACU-B, $z = 1.5$ m for AmC GS and ES events. For all the other calibration points, very good agreement within 1% between the data and MC simulations can be seen.

Besides, the data deviate from the best MC model with fluctuations to both the positive and negative side. This indicates that our good MC models do not have an obvious bias for the neutron related events simulation. The best MC model still has some discrepancy with the calibration data, with a $\chi^2/NDF = 176/59$. The question is whether it is necessary to do some correction for the central value of IBD delayed efficiency. To evaluate the difference for the central value between real data and the best MC model, because of the similarity in definition, I assumed a linear relationship between FGd and IBD delayed efficiency (ϵ_D) as $\epsilon_D = c \cdot \text{FGd} + b$, and fit for each calibration point. This can be regarded as a Taylor's expansion of ϵ_D around the real FGd value within a small range.

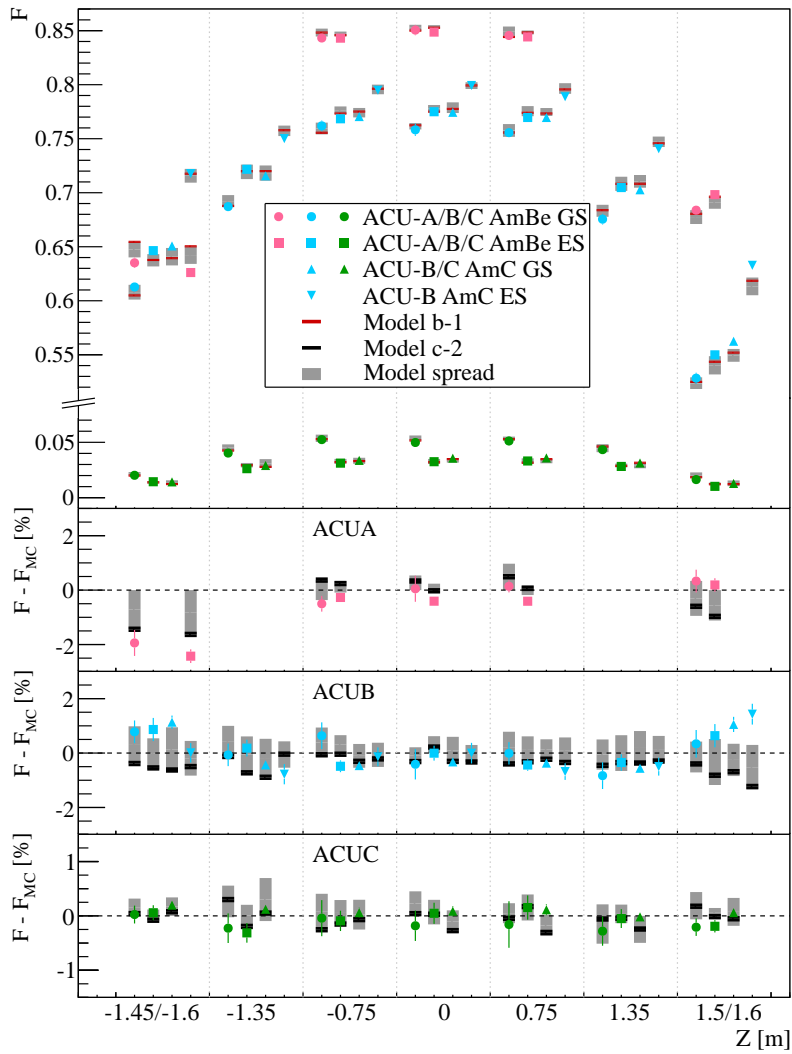
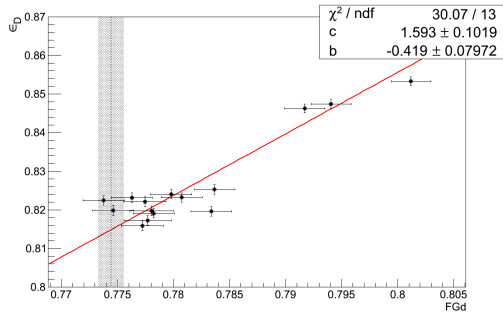
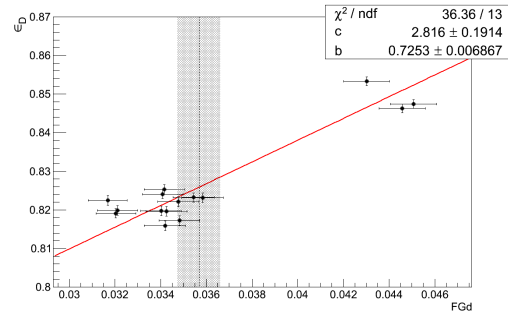


Figure 4.27 The top panel shows the FGd values of data and the 12 reasonable models as a spread, for all calibration points. The bottom three panels show the difference between the data and the best MC model (b-1) of “g4_water_poly” (red bar), for ACU-A/B/C respectively. The model of “Caltech_poly_poly” is also shown (black bar) as another reference.

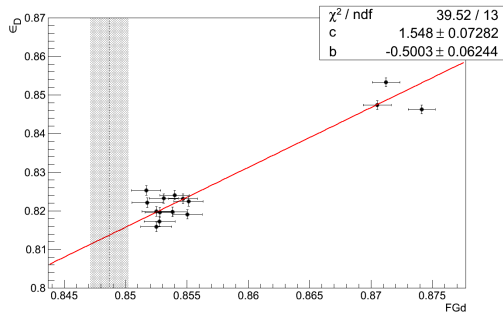
The high order terms are ignored. From the fit result, I can estimate the difference of IBD delayed efficiency between data and the best MC model, as $\Delta\epsilon_D = c \cdot \Delta\text{FGd}$. Fig. 4.28 are examples for the linear fit of the 59 calibration points. Though the three “freegas_freegas” models simulations are a little far away from the real detector, their results can present the detector performance with some small deviation. Thus these three MC simulations are also used in the fit for every calibration point.



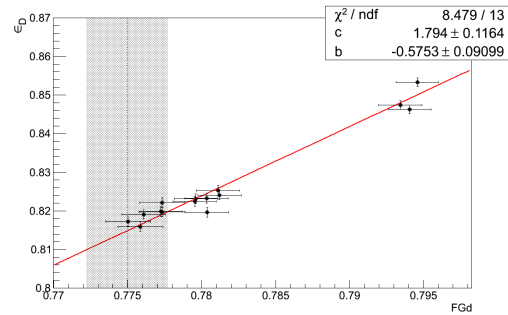
(a) Linear fit for AmC GS in ACU-B, $z = 0$ m. $\Delta\epsilon_D = 1.593 \cdot \Delta\text{FGd}$



(b) Linear fit for AmC GS in ACU-C, $z = 0$ m. $\Delta\epsilon_D = 2.816 \cdot \Delta\text{FGd}$



(c) Linear fit for AmBe ES in ACU-A, $z = 0$ m. $\Delta\epsilon_D = 1.548 \cdot \Delta\text{FGd}$



(d) Linear fit for AmBe ES in ACU-B, $z = 0$ m. $\Delta\epsilon_D = 1.794 \cdot \Delta\text{FGd}$

Figure 4.28 Examples of linear fit for the IBD delayed efficiency and the FGd from MC simulations in the calibration points.

After calculating the IBD delayed efficiency difference ($\Delta\epsilon_D = \epsilon_{D\text{predicted}} - \epsilon_{D\text{best MC}}$) for each calibration point, I made a statistic of them into a histogram. The histogram can be without weight or be weighted by the inverse of uncertainty square.

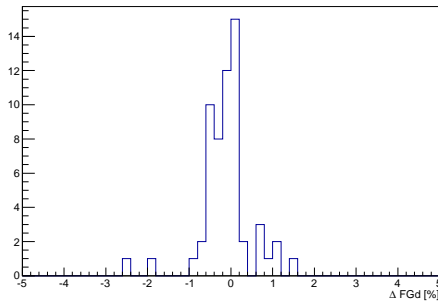
The idea of weight by uncertainty is straight forward as I do need to consider the measurement uncertainty at each calibration point, especially in the condition that relative uncertainties in detector center points and boundary points are quite different. The uncertainty here is the combination of the uncertainty of parameter c in the linear fit and

the uncertainty from FGd data and MC following uncertainty propagation. The weighted average correction is calculated with equation 4-11.

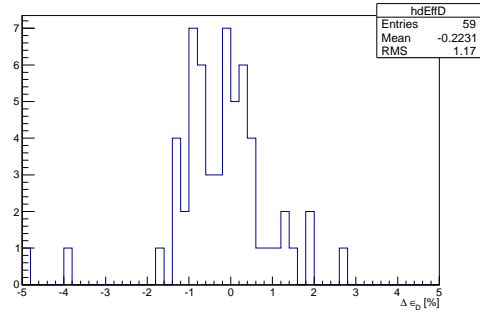
$$\sigma = \Delta\epsilon_D \cdot \sqrt{\frac{\sigma_c^2}{c^2} + \frac{\sigma_{FGdData}^2 + \sigma_{FGd_{best}MC}^2}{\Delta FGd^2}} \quad \text{for every calibration point} \quad (4-11)$$

$$\overline{\Delta\epsilon_D} = \frac{\sum \Delta\epsilon_{Di}/\sigma_i^2}{\sum 1/\sigma_i^2}$$

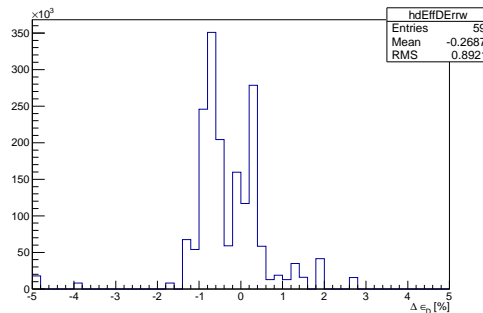
We do not know the relative weight between these two types of weights. So I applied both these two types of weights separately. The results are shown in Fig. 4.29. The mean correction in the no-weight histogram (-0.22%) and in the uncertainty-weighted histogram (-0.27%) are close to each other and within the ϵ_D fluctuation of MC. The IBD delayed efficiency central value was estimated from the best MC (“g4_water_poly” model) with a small correction as $\epsilon_D = 81.75\% - 0.27\% = 81.48\%$.



(a) ΔFGd histogram of 59 calibration points.



(b) $\Delta \epsilon_D$ histogram without weight.



(c) $\Delta \epsilon_D$ histogram weighted by uncertainty ($1/\sigma^2$).

Figure 4.29 ΔFGd and $\Delta \epsilon_D$ distributions.

4.5.2.3 IBD Delayed Efficiency Uncertainty

Our MC simulations with different neutron scattering models and nGd de-excitation γ models can well cover the real situation of neutron related processes in the detector. Basing on these good agreement between data and MC simulations, I used the half range of the MC spread (including the statistical uncertainty) of 0.6% as the uncertainty for the IBD delayed efficiency, equivalently a 0.74% relative uncertainty. Then the IBD delayed efficiency is evaluated as $\epsilon_D = (81.48 \pm 0.6)\%$. I will do more validation for our MC to confirm that this efficiency and uncertainty estimation is reliable.

4.5.3 MC Validation

The FGd comparison shows that the data and MC agrees well, even the FGd changes in a wide range in different position of the detector. Both FGd and the IBD delayed efficiency are sensitive to the neutron propagation, nGd de-excitation γ spectra, γ propagation in the detector. As I directly estimate the IBD delayed efficiency from MC, I do need to ensure that the MC is reliable for all these three aspects and consistent with the real situation inside the detector. Besides the FGd, I checked the other parameters related to these aspects to validate the agreement between true detector and MC.

4.5.3.1 nGd Tail to Peak Ratio (FGamma) Study

We defined a new parameter of the nGd tail to peak ratio, called as FGamma.

$$\text{FGamma} == \frac{N_{3 \text{ MeV} < E < 4.5 \text{ MeV}}}{N_{3 \text{ MeV} < E < 12 \text{ MeV}}} \quad (4-12)$$

This ratio describe the γ leakage of the nGd capture. The numerator of FGamma is the nGd tail events number with a energy cut from 3 MeV to 4.5 MeV. The cutoff at 4.5 MeV is to exclude the nC events, which is negligible compared with the full nGd peak but comparable to the small nGd tail. The cutoff at 3 MeV is to avoid the nH peak. The denominator of FGd is the nGd events above 3 MeV, with very limited nC events. Then we can know that FGamma is sensitive to the nGd de-excitation γ spectra and γ propagation, which determines the γ leakage. Compared with FGd, FGamma is less sensitive to the neutron propagation, as only the nGd events are included. The nGd tail below 3 MeV is hidden behind the significant nH peak as shown in Fig. 4.19. This part of the tail is invisible in data, but we still can get information about leakage from the 3 MeV to 4.5 MeV

tail. The whole tail shape is determined by the γ spectrum and detector geometry^[123]. Under the same mechanism, the tail parts of lower energy region and higher energy region are strongly correlated. I can study the invisible leakage with the visible tail. If part of the tail shows good agreement between data and MC, then it is promising that the whole tail shape should also be consistent.

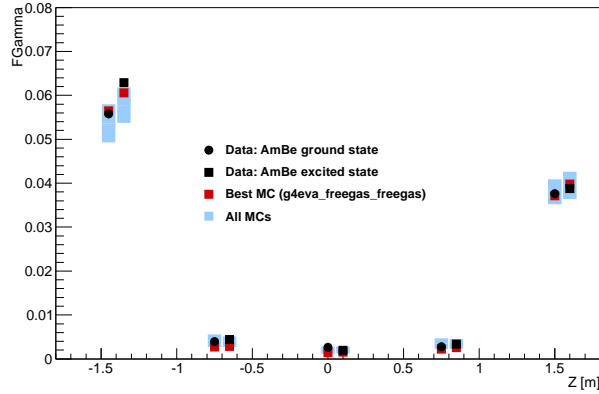
Similar to the FGd study, I calculated the FGamma for each calibration point and constructed a χ^2 as equation 4-13 to evaluate the data and MC difference.

$$\chi_j^2 = \sum_{i=1}^{59} \frac{(\text{FGamma}_{\text{Data},i} - \text{FGamma}_{\text{MC},i})^2}{\sigma_{\text{Data},i}^2 + \sigma_{\text{MC},i}^2} \quad (4-13)$$

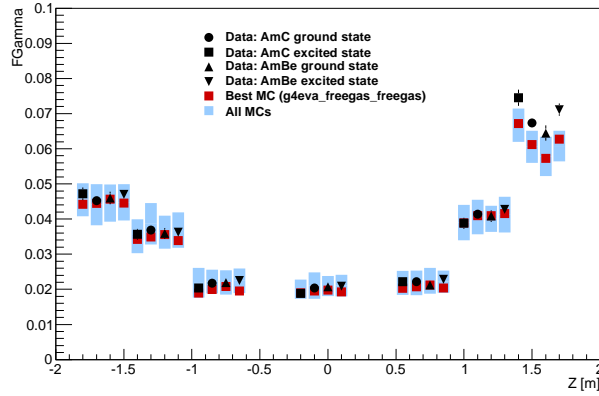
The results of the χ^2 calculation is listed in Table 4.6. The MC model most agrees with data is “g4eva_freegas_freegas” model with the smallest $\chi^2 = 158$. From the table we can find that the FGamma is sensitive to the γ model and less sensitive to the neutron scattering model. For different γ models, the χ^2 values change a lot, while for the same γ model with different neutron scattering models, the χ^2 do not change too much, even for the bad “freegas_freegas” models in FGd study. This is what we have expected. The FGamma comparison of 59 calibration point for data and all MCs are shown in Fig. 4.30. In ACU-A and ACU-B, the data and the best MC have very good agreement, except for the calibration at ACU-B, $z = 1.5$ m. The discrepancy may be caused by some geometry issue. In ACU-C, the nGd events are very limited in total events. The small statistic leads to big uncertainty for the FGamma calculation. For most of the calibration points, the data FGamma value floats inside the spread of all MCs, and have good agreement with the best MC model. From ACU-A to ACU-C, the γ leakage situation changes a lot. The FGamma values varies from 0,4% to as high as 12%. In such a wide range of FGamma changing, the data and MCs have good agreement. This give us confidence on the nGd tail shape and the γ leakage of the detector. In conclusion, the γ spectrum and γ propagation of MC are validated by this FGamma study.

4.5.3.2 Detector Material Density Modification

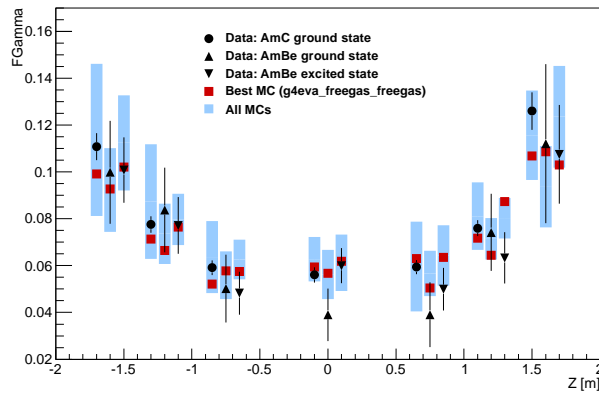
Both the neutron propagation and γ propagation in the detector depend on the detector geometry, cross-section, and target particle number density. The mean free path (mfp) describes the mean path between two scattering during the particle propagation. It is inversely proportional to the product of cross-section and material density (determining



(a) FGamma comparison among data and MCs in ACU-A.



(b) FGamma comparison among data and MCs in ACU-B.



(c) FGamma comparison among data and MCs in ACU-C.

Figure 4.30 FGamma comparison among data and all MC models for the 59 calibration points. In each plot, the black markers are the data points; the red squares are the FGamma values from the best MC; the blue rectangle shows the range of FGamma values of all MCs.

Table 4.6 χ^2 of FGamma for each model.

MC model	χ^2
g4_freegas_freegas	251
g4_water_freegas	245
g4_poly_freegas	218
g4_poly_poly	240
g4_water_poly	242
caltech_freegas_freegas	412
caltech_water_freegas	446
caltech_poly_freegas	399
caltech_poly_poly	470
caltech_water_poly	379
g4eva_freegas_freegas	158
g4eva_water_freegas	161
g4eva_poly_freegas	178
g4eva_poly_poly	164
g4eva_water_poly	174

the target particle number density) as $\text{mfp} \sim 1/\sigma\rho$. If I change the density of the detector material, I equivalently change the mean free path. In this way, I change the neutron and γ propagation in the detector.

In this study, I changed the densities of all the detector materials by $\pm 5\%$ in the best MC model (“g4_water_freegas” model), equivalently change the mean free path by $\pm 5\%$. For the real detector material density measurement at Daya Bay, the density uncertainty is actually smaller than 0.1%. The nGd delayed spectra of the normal density simulation and 2 simulations with modified density are shown in Fig. 4.31. From the plot we can know that the nGd γ leakage and the tail shape do not change too much. The IBD delayed efficiency before and after the density modification are listed in Table 4.7. If the density increases (mfp decreases), fewer γ s would escape from the detector. Then the leakage would be less, leading to a bigger IBD delayed efficiency. On the contrary, the IBD delayed efficiency would be smaller, with the density decreasing and more leakage. Even the density/mfp having a extreme changing by $\pm 5\%$, the IBD delayed efficiencies of the best MC model are still reliable, within the range of the 12 good MC models with the

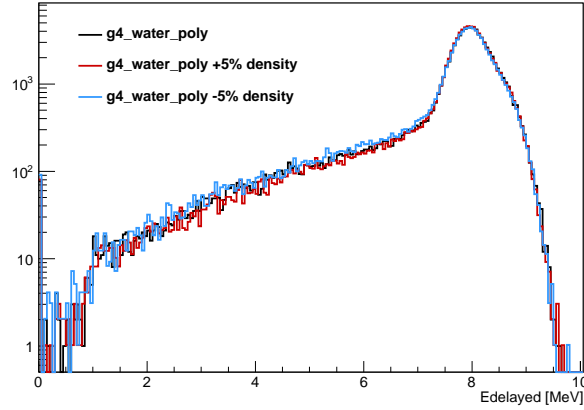


Figure 4.31 The nGd delayed spectra comparison before and after changing the material density: black for normal density sample; red for density increasing 5%; blue for density decreasing 5%.

normal density. This indicates that our MC have already covered a wide enough range of the γ leakage change.

Table 4.7 IBD delayed efficiencies before and after density modification for the best MC model.

Density	normal	normal+5%	normal-5%
ϵ_D	81.8%	82.3%	81.6%

4.5.3.3 Detector Dimension Modification

The neutron and γ propagation are directly related to the detector dimension. The leakage depends on the mean free path and the detector dimension. If I increase the detector material density and have a smaller mean free path, the neutron or γ can scatter for more times before escaping from the detector, just like that I have a bigger detector. So we can know that increasing detector material density is equivalent to increasing the detector dimension. The impact of density modification has been shown in section 4.5.3.2. The detector dimension measurement uncertainty and the detector deformation caused by stress pressure is less than 5%. So the impact of detector dimension modification can be covered by the density modification study.

4.5.3.4 MC Validation Summary

From these three aspects of study we can know that our MC is reliable and stable for all the main factors related to the IBD delayed efficiency: the neutron propagation,

nGd de-excitation γ spectra, γ propagation in the detector. Our MC simulations cover a wide enough range of the γ leakage change while the IBD delayed efficiency is stable. So we can set half of the MC fluctuation as a reasonable uncertainty for the IBD delayed efficiency.

4.5.4 IBD Detection Efficiency and Uncertainty

The IBD delayed efficiency studied with the new MC is $\epsilon_D = (81.48 \pm 0.6)\%$. Combining this with the other cut efficiencies list in Table 4.1, the new estimation of the total IBD detection efficiency is $\epsilon_{IBD} = (80.25 \pm 0.95)\%$, with uncertainty dominated by target protons uncertainty (0.92% relative uncertainty) and ϵ_D uncertainty (0.74% relative uncertainty).

Chapter 5 Flux and Spectrum Measurements at Daya Bay

In this chapter, I will present improved measurements on the reactor antineutrino flux and spectrum at Daya Bay based on the updated estimation of the IBD detection efficiency and uncertainty in Chapter 4. The measurements are conducted with the 1230 days' data sample of the four ADs in the two near experimental halls (EH1+EH2) in Daya Bay. Besides, I will also present studies of correlations between the reactor fuel fission cycle and the antineutrino flux and spectrum. These correlations are used to investigate the reactor antineutrino anomaly, including flux anomaly and spectral anomaly.

5.1 Reactor Antineutrino Flux

Generally the commercial reactors in the nuclear power plants (NPPs) use the low-enriched uranium materials as nuclear fuels. In the nuclear fuel, the electron antineutrinos are produced by the beta decays of the fission fragments from the fissionable isotopes, primarily ^{235}U , ^{238}U , ^{239}Pu , and ^{241}Pu . The theoretical model to calculate the antineutrino flux and spectrum have been discussed in Section 1.3.3.1. The generated antineutrino spectra and detected spectra via IBD reactions for the four primary isotopes are shown in Fig. 5.1, where discrepancies in flux and spectrum among isotopes can be seen.

Daya Bay experiment has reported the reactor antineutrino flux^[76] in two model-independent ways of IBD yield per fission (σ_f in $\text{cm}^2/\text{fission}$) and IBD yield per unit thermal power per day (Y in $\text{cm}^2 \cdot \text{GW}^{-1} \cdot \text{day}^{-1}$), which include the IBD cross-section together with the antineutrino flux. The study of antineutrino flux in this thesis will follow the way, mainly giving the antineutrino flux measurement in the form of IBD yield per fission.

5.1.1 Flux Per Fission

The IBD yield per fission is defined as

$$\sigma_f = \sum_{i=1}^4 f_i \int S_i(E) \sigma(E) dE, \quad (5-1)$$

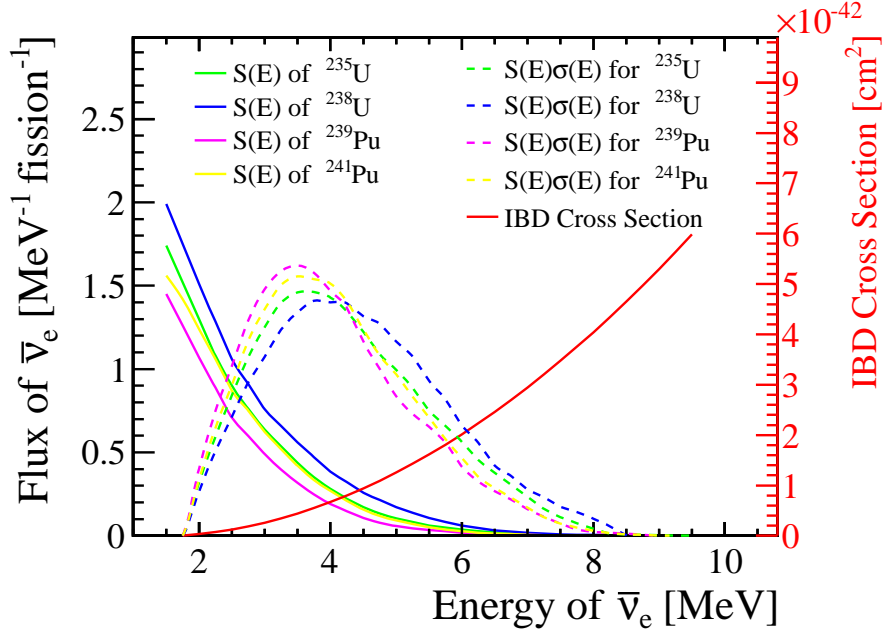


Figure 5.1 The electron antineutrino energy spectra per fission from four primary fissionable isotopes in Huber-Mueller model^[31,32] are shown with solid colorful lines. The red line and axis on the right side is for the IBD reaction cross-section^[33]. The detected neutrino spectra of $S(E)\sigma(E)$ are the dashed lines with corresponding colors, while each of them is self-normalized. The y-axis for these normalized spectra is not drawn.

where i loops for the four primary fissionable isotopes, f_i is the fraction contributed from the i -th isotope in all fission reactions with the sum of them to unit ($\sum_i f_i=1$), $S_i(E)$ is the antineutrino spectrum per fission by the i -th isotope, and $\sigma(E)$ is the IBD reaction cross-section. This IBD yield per fission is independent of detectors but relied on the reactor fuel composition because of the fission fractions. Taking into account these fission fractions, the IBD yields per fission measured by different experiments can be somehow compared.

For a simple case of one detector and one reactor core, the number of expected IBD events per unit time is

$$N_{\text{IBD}} = \frac{N_{\text{proton}}\epsilon W_{\text{th}}}{4\pi L^2 \sum_{i=1}^4 f_i e_i} \int P_{\text{surv}}(E, L)\sigma(E) \sum_{i=1}^4 f_i S_i(E) dE, \quad (5-2)$$

where N_{proton} is the number of target protons, ϵ is the IBD detection efficiency, L is the baseline from reactor core center to the detector, i loops for four primary fissionable isotopes, e_i is the average energy released per fission for isotope i (summarized in Table 5.1), W_{th} is the thermal power of the reactor core, thus $\frac{W_{\text{th}}}{\sum_{i=1}^4 f_i e_i}$ is the average number of fission

reactions per unit time in the reactor core, $P_{\text{surv}}(E, L)$ is the antineutrino survival probability due to neutrino oscillation and it depends on antineutrino energy E and the baseline L , $\sigma(E)$ is the cross-section of IBD reaction, and $S_i(E)$ is the antineutrino spectrum per fission of the i -th isotope.

Table 5.1 The average energy released per fission and their uncertainties for the four primary fissionable isotopes in nuclear fuel^[124].

Isotope	Energy per fission [MeV]
^{235}U	202.36 ± 0.26
^{238}U	205.99 ± 0.52
^{239}Pu	211.12 ± 0.34
^{241}Pu	214.26 ± 0.33

To get a model-independent IBD yield per fission, I need to separate the model-dependent spectrum $S_i(E)$ from others. Thus a flux-weighted average survival probability $\bar{p}(L)$ is defined to make equation (5-2) as

$$\begin{aligned}
 N_{\text{IBD}} &= \frac{N_{\text{proton}} \epsilon W_{\text{th}} \bar{p}(L)}{4\pi L^2 \sum_{i=1}^4 f_i e_i} \sum_{i=1}^4 f_i \int S_i(E) \sigma(E) dE \\
 &= \frac{N_{\text{proton}} \epsilon \bar{p}(L)}{4\pi L^2} \cdot \underbrace{\frac{W_{\text{th}}}{\sum_{i=1}^4 f_i e_i}}_{\text{fissions in reactor}} \cdot \sigma_f \\
 &= N_{\text{fission}}^{\text{detector}} \cdot \sigma_f,
 \end{aligned} \tag{5-3}$$

where $N_{\text{fission}}^{\text{detector}}$ is the number of fission reactions per unit time viewed by the detector and it is modulated by the average survival probability, baseline and also the detector property. Then I can measure a model-independent IBD yield per fission as

$$\sigma_f = \frac{N_{\text{IBD}}}{N_{\text{fission}}^{\text{detector}}}. \tag{5-4}$$

For the complicated experimental configuration of four ADs and six reactor cores with multiple baselines from cores to ADs in Daya Bay, to get the IBD yield per fission, I need to count the measured IBD events in all ADs, and also the total number of fission reactions viewed by ADs. Besides, the thermal powers and fission fractions in reactor

cores are changing all the time. The antineutrino spectrum measured by one AD from six reactor cores during the whole data-taking period can be expressed as

$$N(E)^{\text{AD}} = \sum_{c=1}^6 \frac{N_{\text{proton}} \sigma(E) \epsilon P_{\text{surv}}(E, L_c)}{4\pi L_c^2} \int \frac{d^2 \phi_c(E, t)}{dE dt} dt, \quad (5-5)$$

where E is the antineutrino energy, c presents the c -th reactor core, N_{proton} is the number of target protons, $\sigma(E)$ is the cross-section of IBD reaction depending on antineutrino energy, ϵ is the IBD detection efficiency, $P_{\text{surv}}(E, L_c)$ is the antineutrino survival probability, L_c is the baseline from reactor core c to the AD. The last term $\int \frac{d^2 \phi_c(E, t)}{dE dt} dt$ is the initial antineutrino spectrum from the c -th reactor core during the data-taking time. In Daya Bay, this spectrum has other corrections as

$$\frac{d^2 \phi(E, t)}{dE dt} = \frac{W_{\text{th}}(t)}{\sum_{i=1}^4 f_i(t) e_i} \sum_{i=1}^4 f_i(t) S_i(E) c_i^{\text{NE}}(E, t) + S_{\text{SNF}}(E, t), \quad (5-6)$$

where i loops for the four primary fissionable isotopes, $W_{\text{th}}(t)$ is the thermal power of the reactor core, $f_i(t)$ is the fractional contribution in total fissions from the i -th isotope, e_i is the average energy released per fission for isotope i . The information of weekly fission fractions and reactor real-time thermal power are provided by the Nuclear Power Plant. For the other terms in equation (5-6), $S_i(E)$ is the antineutrino spectrum per fission, $c_i^{\text{NE}}(E, t)$ is the correction due to reactor non-equilibrium (NE) effects^[125] caused by the long-lived fission daughter, and $S_{\text{SNF}}(E, t)$ is the antineutrino spectrum emitted by the spent nuclear fuel (SNF) in the cooling pool adjacent to the reactor core. The corrections contributed from non-equilibrium effects and the spent nuclear fuel are about 0.6% and 0.3% in the total predicted number of antineutrinos, introducing fractional uncertainties of 0.2% and 0.3% respectively^[76]. Though the SNF spectrum is not related to the fission fraction, I can rewrite the antineutrino spectrum to simplify the equations:

$$\sum_{i=1}^4 f_i(t) S_i^{\text{NE+SNF}}(E) = \sum_{i=1}^4 f_i(t) S_i(E) c_i^{\text{NE}}(E, t) + S_{\text{SNF}}(E, t), \quad (5-7)$$

where $S_i^{\text{NE+SNF}}(E)$ is antineutrino spectrum after NE effects and SNF corrections.

Same as in equation (5-3), I calculated the flux-weighted average survival probability

for one reactor core to one AD as

$$\bar{p}(L) \int \sum_{i=1}^4 f_i S_i^{\text{NE+SNF}}(E) \sigma(E) dE = \int \sum_{i=1}^4 P_{\text{surv}}(E, L) f_i S_i^{\text{NE+SNF}}(E) \sigma(E) dE, \quad (5-8)$$

and this average survival probability is quite stable within 0.1% no matter how much the fission fractions change. So I assigned a 0.1% uncertainty in the total number of IBD events for oscillation and treat the survival probability as time-independent and also isotope-independent.

The total number of expected IBD events in one AD is the integral of equation (5-5) over antineutrino energy as:

$$N_{\text{IBD}}^{\text{AD}} = \sum_{c=1}^6 \frac{N_{\text{proton}} \epsilon \bar{p}(L_c)}{4\pi L_c^2} \cdot \underbrace{\sum_{i=1}^4 \left[\int \frac{W_{\text{th},c}(t) f_{i,c}(t)}{\sum_{i=1}^4 f_{i,c}(t) e_i} dt \right]}_{\text{time-dependent}} \cdot \underbrace{\int \sigma(E) S_i^{\text{NE+SNF}}(E) dE}_{\text{energy-dependent}}. \quad (5-9)$$

The total number of fission reactions from six reactor cores viewed by the AD is

$$N_{\text{fission}}^{\text{AD}} = \sum_{c=1}^6 \frac{N_{\text{proton}} \epsilon \bar{p}(L_c)}{4\pi L_c^2} \int \frac{W_{\text{th},c}(t)}{\sum_{i=1}^4 f_{i,c}(t) e_i} dt, \quad (5-10)$$

with the effective fission fraction for one isotope i as

$$\bar{F}_i = \sum_{c=1}^6 \frac{N_{\text{proton}} \epsilon \bar{p}(L_c)}{4\pi L_c^2} \int \frac{W_{\text{th},c}(t) f_{i,c}(t)}{\sum_{i=1}^4 f_{i,c}(t) e_i} dt / N_{\text{fission}}^{\text{AD}}. \quad (5-11)$$

Combining equations (5-9), (5-10) and (5-11), the total number of IBD events and IBD yield per fission for one AD can be expressed as

$$\begin{aligned} N_{\text{IBD}}^{\text{AD}} &= N_{\text{fission}}^{\text{AD}} \sum_{i=1}^4 \bar{F}_i \int \sigma(E) S_i^{\text{NE+SNF}}(E) dE \\ &= N_{\text{fission}}^{\text{AD}} \cdot \sigma_f^{\text{AD}}, \end{aligned} \quad (5-12)$$

where $N_{\text{IBD}}^{\text{AD}}$ is the total number of expected IBD events in one AD, $N_{\text{fission}}^{\text{AD}}$ is the total number of fission reactions viewed by the AD, and σ_f^{AD} is the average IBD yield per fission for the AD.

For a combined measurement with all the four near ADs, the total number of fission reactions viewed by ADs can be obtained by the summation of fission number from each AD as in equation (5-10). After analyzing all the information of thermal power and fission fractions for each reactor core, as well the livetime in each AD, I calculated the total number of fissions viewed by four ADs as 3.720×10^{52} fission \cdot cm⁻² in the 1230-day livetime. The number of detected IBD events in the same data-taking period are determined to be 2.201×10^6 with 0.1% statistic uncertainty obtained from Table 2.4 in Section 2.6 of IBD Event Selection. Eventually, the average IBD yield per fission central value is calculated as 5.92×10^{-43} cm²/fission.

The total flux-weighted average fission fractions contributed from four isotopes can be calculated similar to equation (5-11). In the whole data-taking period for all near ADs, I determined the total flux-weighted average fission fractions of four primary fissionable isotopes (²³⁵U, ²³⁸U, ²³⁹Pu, ²⁴¹Pu) as (0.571, 0.076, 0.299, 0.054) respectively. With these average fission fractions and the energy released per fission in Table 5.1, I calculated the average energy released per fission as 205.9 MeV and the average number of fission reactions for 1 GW thermal power \times 1 day as 2.619×10^{24} fissions. Together with the IBD yield per fission of 5.92×10^{-43} cm²/fission, the IBD yield per GW thermal power per day is 1.55×10^{-18} cm²/GW/day.

The results above are the central values for IBD yield, then I will estimate the systematic uncertainty for the measurement. From equation (5-10) we can know the parameters contributing to the systematic uncertainties of the expected number of fission reactions, as summarized in Table 5.2.

Together with the IBD detection efficiency and uncertainty measured in Chapter 4, the sources of the uncertainties in antineutrino flux measurement are summarized in Table 5.3, eventually leading to a total flux measurement uncertainty as 1.5% for Daya Bay. Due to the 40% improvement in the IBD detect efficiency uncertainty, the flux measurement precision has been improved by about 30% compared with previous Daya Bay measurement^[76].

With this 1.5% uncertainty for the total flux measurement, I obtained the average IBD yield per fission and IBD yield per GW_{th} power per day respectively as

$$\begin{aligned}\sigma_f &= (5.92 \pm 0.09) \times 10^{-43} \text{ cm}^2/\text{fission} \\ Y &= (1.53 \pm 0.02) \times 10^{-18} \text{ cm}^2/\text{GW}/\text{day} .\end{aligned}\tag{5-13}$$

Table 5.2 Summary of model-independent systematic uncertainties (fractional) of the predicted number of fission reactions for a reactor core^[76]. The model-dependent spectrum uncertainty for one isotope is 2.4% in Huber-Mueller model. This term is not listed in the table.

Parameter	Uncertainty
Power	0.5%
Energy per fission	0.2%
IBD cross-section	0.12%
Fission fraction	0.6%
Baseline	(negligible)
Non-equilibrium	0.2%
Spent nuclear fuel	0.3%
Reactor total	0.9%

Table 5.3 Summary of fractional contributions to the total uncertainty of the reactor antineutrino flux measurement. The previous uncertainty was used in previous Daya Bay publication^[76]. The new uncertainty is obtained by the study of this thesis. A reduction about 30% is achieved due to the improvement of the IBD detection efficiency uncertainty.

Contribution	Previous uncertainty	New uncertainty
Statistics	0.1%	0.1%
Oscillation	0.1%	0.1%
Reactor	0.9%	0.9%
Detection efficiency	1.93%	1.19%
Total	2.1%	1.5%

Using the IBD yields for the four isotopes predicted by the flux models (summarized in Table 5.1) and the obtained average fission fractions, I calculated the total average IBD yield per fission predicted by the Huber-Mueller model as $6.22 \times 10^{-43} \text{cm}^2/\text{fission}$. Considering about the total flux measurement uncertainty of 1.5% and the Huber-Mueller model uncertainty of 2.4%, I got the ratio of measurement to prediction as

$$R \text{ (Huber-Mueller)} = 0.952 \pm 0.014(\text{exp.}) \pm 0.023(\text{theo.}), \quad (5-14)$$

in which the model uncertainty dominates. This deficit is at the confidence level of 1.8σ (including the model uncertainty), confirming the reactor antineutrino anomaly is

observed in Daya Bay. If we only consider the experimental uncertainty, the deficit can reach a significance of 3σ .

Table 5.4 The IBD yields per fission of the four primary fissionable isotopes, predicted in Huber-Mueller model^[58]

Isotope	IBD yield per fission [$10^{-43}\text{cm}^2/\text{fission}$]
^{235}U	$6.69 \pm 2.11\%$
^{238}U	$10.10 \pm 8.15\%$
^{239}Pu	$4.36 \pm 2.45\%$
^{241}Pu	$6.05 \pm 2.15\%$

This 1.5% flux measurement uncertainty makes Daya Bay experiment as one of the most precise reactor antineutrino flux measurements. Table 5.5 shows the comparison of current reactor antineutrino flux measurement experiments throughout the world.

Table 5.5 Comparison of present measurements of reactor antineutrino flux throughout the world. R stands for the ratio of measurement to Huber-Mueller model prediction. The high precision experiments are selected of Bugey-4^[126], Chooz^[29], Daya Bay^[76], RENO^[77] and Double Chooz^[127].

	R (meas./pred.)	Uncertainty [%]	Baseline [m]
Bugey-4	0.932	1.4	15
Chooz	0.996	3.2	≈ 1000
Daya Bay	0.946	2.1	≈ 550
RENO	0.946	2.1	≈ 410
Double Chooz	0.935	1.4	≈ 415
Daya Bay with this thesis	0.952	1.5	≈ 550

5.1.2 Flux Evolution With Fuel Cycle

During the long data-taking period of 1230 days, the Daya Bay reactor cores have gone through several nuclear fuel cycles with refueling. The fresh nuclear fuel has a high fission fraction contributed from ^{235}U . As the nuclear fuel burns up, more and more plutonium nuclei are produced via the neutron capture on ^{238}U , giving increasing fission fractions for ^{239}Pu and ^{241}Pu in the reactor core. The change of fission fractions (fuel

composition) leads to variance of the total IBD yield correspondingly, because the four primary fissionable isotopes have different IBD yields. This is called as the antineutrino flux evolution with fuel cycle. This effect can be observed by the change of detected IBD event rate in the detector as a real-time monitoring of the reactor core with fuel burn-up.

The measured daily IBD event rates for all ADs in Daya Bay are shown in Fig. 5.2, where the predictions of IBD event rates calculated with and without neutrino oscillations are overlaid as well. In Fig. 5.2, the fluctuation of daily IBD event rates are due to the thermal power change of reactor cores, while the wide gaps are due to the shutdown of reactor cores for refueling or maintenance reasons. It shows a very good agreement between the measurement and the prediction with neutrino oscillation correction for several nuclear fuel cycles.

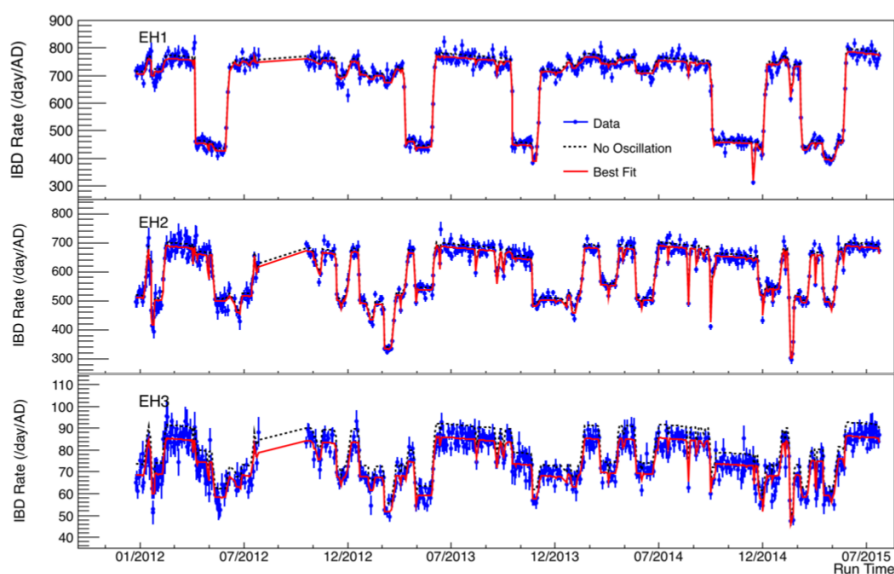


Figure 5.2 The daily IBD event rates for measurement (blue points) and prediction with oscillation effects (red line). Also overlaid is the black dotted line for no oscillation prediction. The figure is from Daya Bay collaborators.

To study the impact of reactor fuel fission cycle (fuel evolution) on the antineutrino flux, I used a shorter time period of one week to measure the IBD yield and investigate the correlation between the antineutrino flux and the fuel fission cycle. The calculations for the weekly effective fission fractions are same as equation (5-11) but the integral over time is for a shorter time period of AD livetime in one week. Explicitly, the effective

fission fractions were calculated as

$$\begin{aligned}
 N_{\text{fission}}^{\text{AD, week}} &= \sum_{c=1}^6 \frac{N_{\text{proton}} \epsilon \bar{p}(L_c)}{4\pi L_c^2} \int_{\text{a week}} \frac{W_{\text{th},c}(t)}{\sum_{i=1}^4 f_{i,c}(t) e_i} dt \\
 F_i &= \sum_{c=1}^6 \frac{N_{\text{proton}} \epsilon \bar{p}(L_c)}{4\pi L_c^2} \int_{\text{a week}} \frac{W_{\text{th},c}(t) f_{i,c}(t)}{\sum_{i=1}^4 f_{i,c}(t) e_i} dt / N_{\text{fission}}^{\text{AD, week}},
 \end{aligned} \tag{5-15}$$

where i presents the i -th isotope of the four. The effective fission fractions for four primary isotopes (^{235}U , ^{238}U , ^{239}Pu , ^{241}Pu) will be denoted as $(F_{235}, F_{238}, F_{239}, F_{241})$ respectively.

I calculated the weekly effective fission fractions with equation (5-15) for each AD basing on the weekly information of reactor core thermal power and fission fractions for four isotopes, as shown in Fig. 5.3. This weekly information was provided by the nuclear power plant and was also validated with the APOLLO2 reactor modeling simulation by previous Daya Bay studies^[128,129].

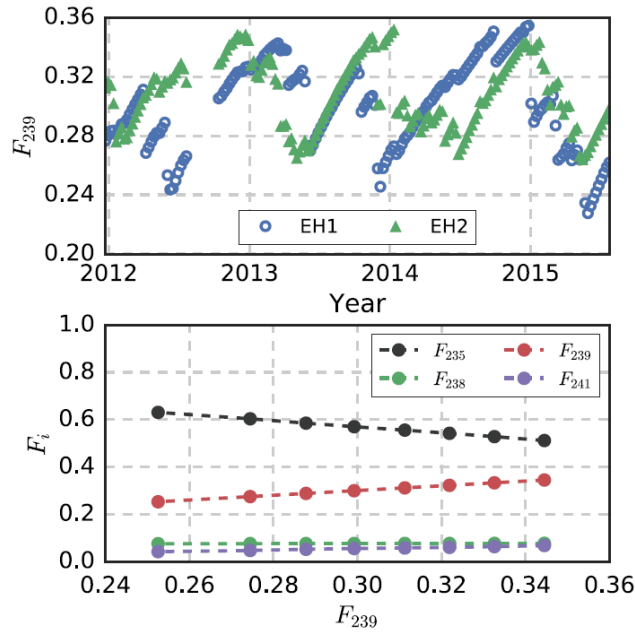


Figure 5.3 Top panel is the weekly information of the effective fission fractions F_{239} for ^{239}Pu in the ADs of EH1 and EH2. Bottom panel shows the effective fission fractions for the four primary fissionable isotopes of (^{235}U , ^{238}U , ^{239}Pu , ^{241}Pu) versus F_{239} .

I used the effective fission fractions F_{239} (it is increasing along with the reactor fuel burn-up) to group the weekly IBD data sets into eight bins with different fuel compositions. Each F_{239} bin has similar statistic of IBD events, which are used to study the correlation between the reactor antineutrino flux and the reactor fuel fission cycles. With the similar

calculation as for the average IBD yield per fission of the total data-taking period in Section 5.1.1, I calculated the numbers of measured IBD events and the numbers of predicted fission reactions viewed by ADs in each F_{239} bin, and subsequently got the average IBD yield per fission within this F_{239} range. I calculated the IBD yield per fission with both the IBD detection efficiencies in previous Daya Bay publications^[76,91] and in the study of this thesis. The study of reactor antineutrino flux evolution with the previous IBD detection efficiency has been published^[92]. Due to the change of IBD detection efficiency and uncertainty from $\epsilon_{\text{IBD}} = (80.60 \pm 1.56)\%$ to $\epsilon_{\text{IBD}} = (80.25 \pm 0.95)\%$, the IBD yield per fission in each F_{239} bin with the new efficiency is 0.4% higher than that with the previous efficiency. The effective fission fractions of four primary fissionable isotopes and the measured IBD yields per fission for eight F_{239} bins are summarized in Table 5.6 and are also shown in Fig. 5.4. In this section and hereafter, I will denote the results obtained with the previous IBD detection efficiency and uncertainty as the “**previous result**”, and denote the results obtained with the new IBD detection efficiency and uncertainty as the “**new result**”.

Table 5.6 The average effective fission fractions for four primary fissionable isotopes and the measured IBD yields per fission with previous/new IBD detection efficiency for eight F_{239} bins.

Bin	F_{239}	F_{235}	F_{238}	F_{241}	$\sigma_f [10^{-43}\text{cm}^2/\text{fission}]$ (previous)	$\sigma_f [10^{-43}\text{cm}^2/\text{fission}]$ (new)
1	0.2525	0.6304	0.0754	0.0417	6.009	6.036
2	0.2744	0.6033	0.0757	0.0466	5.941	5.967
3	0.2878	0.5849	0.0758	0.0515	5.916	5.942
4	0.2992	0.5699	0.0760	0.0549	5.911	5.936
5	0.3113	0.5553	0.0762	0.0572	5.873	5.899
6	0.3219	0.5418	0.0764	0.0599	5.856	5.881
7	0.3326	0.5279	0.0766	0.0629	5.840	5.865
8	0.3445	0.5113	0.0767	0.0675	5.823	5.848

The antineutrino flux measurements (IBD yields per fission) in these eight F_{239} bins are partially correlated to each other. This feature is important for the flux evolution study as I investigate the flux change in different bins. For the uncertainty sources of flux measurement listed in Table 5.3, the statistical uncertainties in eight bins are totally uncorrelated while the systematic uncertainties from oscillation (due to average survival probability), reactor, and IBD detection efficiency are almost fully correlated for eight F_{239} bins. The uncorrelated part in systematic uncertainty is from the 0.13% IBD detection

efficiency variation in the four near ADs although four ADs were designed identically. The statistical uncertainties in eight bins are about 0.2%, which are larger than the 0.1% statistical uncertainty of full data sample because the data set in one F_{239} bin is only a subset of full data sample. The systematic uncertainties in eight bins are the same as the full data sample ($\sigma_{\text{syst.}} = \sqrt{1.5\%^2 - 0.1\%^2} \approx 1.5\%$). The covariance matrix for the flux measurements in eight F_{239} bins are shown in Table 5.7.

Table 5.7 The fractional covariance matrix (\mathbf{M}) for the flux measurements (σ_f) in eight F_{239} bins: $\text{Cov}(\sigma_{f,i}, \sigma_{f,j}) = \mathbf{M}_{ij} \cdot \sigma_{f,i} \cdot \sigma_{f,j}$. This covariance matrix is calculated with the new IBD detection uncertainty.

	bin 1	bin 2	bin 3	bin 4	bin 5	bin 6	bin 7	bin 8
bin 1	2.28E-04	2.23E-04	2.24E-04	2.24E-04	2.23E-04	2.23E-04	2.23E-04	2.24E-04
bin 2	2.23E-04	2.27E-04	2.24E-04	2.23E-04	2.23E-04	2.23E-04	2.23E-04	2.24E-04
bin 3	2.24E-04	2.24E-04	2.29E-04	2.25E-04	2.24E-04	2.24E-04	2.23E-04	2.27E-04
bin 4	2.24E-04	2.23E-04	2.25E-04	2.28E-04	2.24E-04	2.24E-04	2.24E-04	2.26E-04
bin 5	2.23E-04	2.23E-04	2.24E-04	2.24E-04	2.27E-04	2.24E-04	2.24E-04	2.25E-04
bin 6	2.23E-04	2.23E-04	2.24E-04	2.24E-04	2.24E-04	2.27E-04	2.24E-04	2.25E-04
bin 7	2.23E-04	2.23E-04	2.23E-04	2.24E-04	2.24E-04	2.24E-04	2.27E-04	2.24E-04
bin 8	2.24E-04	2.24E-04	2.27E-04	2.26E-04	2.25E-04	2.25E-04	2.24E-04	2.37E-04

After I got the IBD yields per fission and uncertainties in eight F_{239} bins, I fit these data with a linear function to get the total averaged IBD yield ($\bar{\sigma}_f$) wighted by F_{239} and the slope of $d\sigma_f/dF_{239}$ with equation (5-16)

$$\sigma_f(F_{239}) = \bar{\sigma}_f + \frac{d\sigma_f}{dF_{239}}(F_{239} - \bar{F}_{239}). \quad (5-16)$$

The fit was done by minimizing the χ^2 of equation (5-17)

$$\chi^2 = (\boldsymbol{\sigma}_f - \bar{\boldsymbol{\sigma}}_f - \frac{d\sigma_f}{dF_{239}}(\mathbf{F}_{239} - \bar{\mathbf{F}}_{239}))^T \mathbf{V}^{-1} (\boldsymbol{\sigma}_f - \bar{\boldsymbol{\sigma}}_f - \frac{d\sigma_f}{dF_{239}}(\mathbf{F}_{239} - \bar{\mathbf{F}}_{239})), \quad (5-17)$$

where $\boldsymbol{\sigma}_f$ is a vector of the eight measured IBD yields per fission, $\bar{\boldsymbol{\sigma}}_f$ is a vector of eight identical elements for the average IBD yield, \mathbf{F}_{239} is a vector of the eight ^{239}Pu effective fission fraction in eight bins, and $\bar{\mathbf{F}}_{239}$ is a vector of eight identical elements for the average ^{239}Pu relative fission fraction (0.299). The matrix \mathbf{V} is the covariance matrix (calculated by Table 5.7) providing the uncertainties and correlations from the reactor, statistical, and

IBD detection efficiency. With the previous IBD detection efficiency and uncertainty, the best-fit values for the parameters were found to be $\bar{\sigma}_f = 5.90 \pm 0.13 \times 10^{-43} \text{cm}^2/\text{fission}$ and $d\sigma_f/dF_{239} = -1.86 \pm 0.18 \times 10^{-43} \text{cm}^2/\text{fission}$, with a χ^2/NDF of 3.6/6. With the new IBD detection efficiency and uncertainty, the measured IBD yields σ_f and covariance matrix \mathbf{V} were updated. The best-fit values for the parameters were found to be $\bar{\sigma}_f = 5.92 \pm 0.09 \times 10^{-43} \text{cm}^2/\text{fission}$ and $d\sigma_f/dF_{239} = -1.87 \pm 0.18 \times 10^{-43} \text{cm}^2/\text{fission}$, with a χ^2/NDF of 3.6/6, as shown in Fig. 5.4. The Huber-Mueller model prediction and

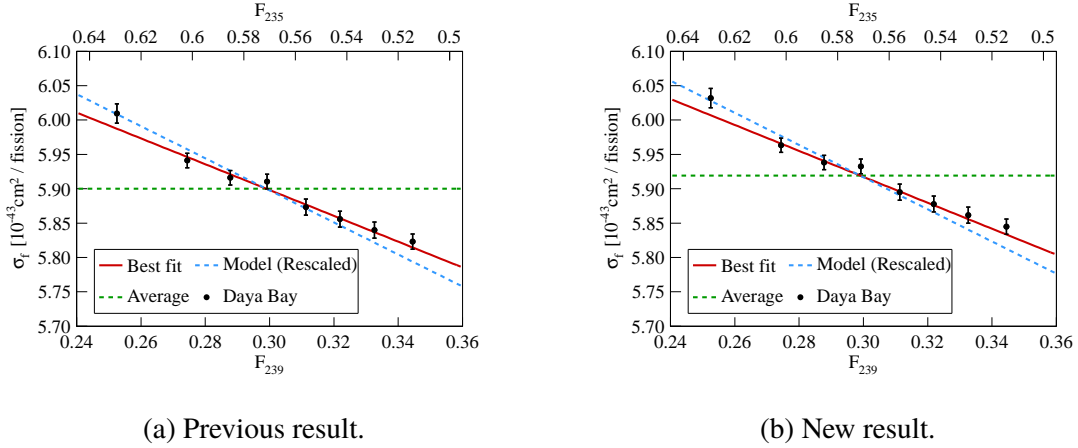


Figure 5.4 Relationship between the IBD yield per fission (σ_f) and the effective fission fraction of ^{239}Pu in the lower x axis (or ^{235}U in the upper x axis). The left figure is for the result with previous IBD detection efficiency and uncertainty^[92], and the right figure is the result with new IBD detection efficiency and uncertainty.

fit result with previous/new IBD detection efficiency and uncertainty are summarized in Table 5.8. The model prediction for $d\sigma_f/dF_{239}$ is calculated with the predicted IBD yields per fission and fission fractions for the four isotopes in the eight F_{239} bins.

Table 5.8 Comparison of average IBD yield and the slope of $d\sigma_f/dF_{239}$ in fit. The theoretical prediction is from Huber-Mueller model.

	Theoretical prediction	Previous result	New result
$\bar{\sigma}_f (10^{-43} \text{cm}^2/\text{fission})$	6.22 ± 0.14	5.90 ± 0.13	5.92 ± 0.09
$\frac{d\sigma_f}{dF_{239}} (10^{-43} \text{cm}^2/\text{fission})$	-2.46 ± 0.06	-1.86 ± 0.18	-1.87 ± 0.18

The flux-weighted average IBD yield $\bar{\sigma}_f$ by the fit is the same as the result in direct measurement in last Section 5.1.1, with a ratio of $R = 0.952 \pm 0.014(\text{exp.}) \pm 0.023(\text{model})$ to the Huber-Mueller model prediction. This difference is at the confidence level of 1.8σ (including model uncertainty) while the measured $d\sigma_f/dF_{239}$ differs from the model

prediction by 3.1σ . From table 5.8, one can find that the uncertainty of $\bar{\sigma}_f$ in new result is reduced by 30% compared with the previous result. However the uncertainty of $d\sigma_f/dF_{239}$ keeps the same as before. Then I did an analysis for the uncertainty budget of the fit, dividing it into the statistical part and the systematic part. The statistical part $\sigma_{stat.}$ is the uncertainty in fit result with only the statistical uncertainty in the covariance matrix. In this case, the covariance matrix is a diagonal matrix. The systematic part $\sigma_{syst.}$ is got by $\sigma_{syst.}^2 = \sigma_{stat.+syst.}^2 - \sigma_{stat.}^2$, where $\sigma_{stat.+syst.}$ is the uncertainty in the fit with complete covariance matrix. The results are shown in Fig. 5.5. For average

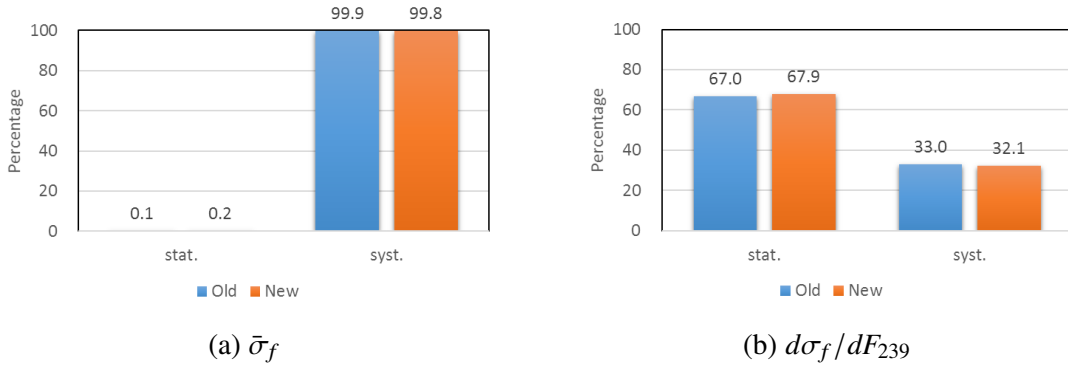


Figure 5.5 Uncertainty budget of the linear fit. The blue bar is for the previous (old) result while the orange bar is for the updated result with new IBD detection efficiency and uncertainty.

IBD yield per fission, systematic uncertainty still dominates in total uncertainty, thus the total uncertainty shrinks a lot with a smaller IBD detection uncertainty than previous result. For the slope, systematic uncertainty improvement has very limited impact as the statistical uncertainty dominates here.

The measurement of correlation between IBD yields per fission and the reactor fuel fission cycle in Daya Bay (shown in Fig. 5.4) can also be used to determine the individual IBD yields per fission from ^{235}U and ^{239}Pu . For each bin, the measured IBD yield per fission can be expressed as the weighted sum of all the four isotopes as

$$\sigma_f^j = \sum_i F_i^j \sigma_i, \quad (5-18)$$

where σ_i is the IBD yield per fission from the i -th isotope and F_i^j is the effective fission fraction of that isotope in bin j . Measurements of σ_f in all bins can be summarized with

the matrix equation

$$\boldsymbol{\sigma}_f = \mathbf{F}\boldsymbol{\sigma}, \quad (5-19)$$

where $\boldsymbol{\sigma}_f$ is a vector of the eight measured IBD yields per fission, $\boldsymbol{\sigma}$ is a four-element vector of the IBD yields for the four fission isotopes, and \mathbf{F} is a matrix for four fission fractions in eight bins (8×4). I constructed a χ^2 based on the matrix equation as:

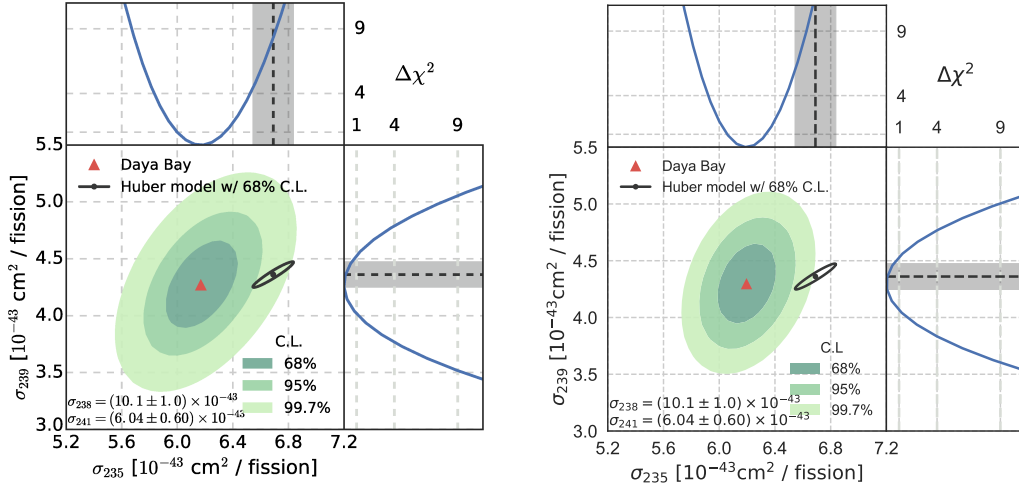
$$\chi^2 = (\boldsymbol{\sigma}_f - \mathbf{F}\boldsymbol{\sigma})^T \mathbf{V}^{-1} (\boldsymbol{\sigma}_f - \mathbf{F}\boldsymbol{\sigma}) + \sum_{i=F_{238}, F_{241}} \frac{(\sigma_i - \hat{\sigma}_i)^2}{\epsilon_i^2}. \quad (5-20)$$

The matrix \mathbf{V} is the same covariance matrix as in the linear fit ahead. The last pull term is a constraint for the two minor fission isotopes ^{238}U and ^{241}Pu to be around the theoretical predictions, as their contributions to the total fissions are too small. $\hat{\sigma}_i$ are the theoretically predicted IBD yields from Huber-Mueller model. ϵ_i is the uncertainty for constraint, which is set as 10% of the predicted IBD yield per fission in Huber-Mueller model and this is significantly higher than the quoted Huber-Mueller uncertainties (8.15% for ^{238}U and 2.15% for ^{241}Pu), in order to reduce the potential bias to the fit.

With the previous IBD detection efficiency and uncertainty, the fit determined the IBD yields per fission for ^{235}U and ^{239}Pu as $\sigma_{235} = (6.17 \pm 0.17) \times 10^{-43} \text{cm}^2/\text{fission}$ and $\sigma_{239} = (4.27 \pm 0.26) \times 10^{-43} \text{cm}^2/\text{fission}$ separately, with a χ^2/NDF of 3.6/6, as shown in Fig. 5.6(a). The figure also shows the one-dimensional $\Delta\chi^2$ profiles for σ_{235} and σ_{239} , and the 1σ allowed region by Huber-Mueller model. With the new IBD detection efficiency and uncertainty, the fit determined the IBD yields per fission for ^{235}U and ^{239}Pu as $\sigma_{235} = (6.19 \pm 0.14) \times 10^{-43} \text{cm}^2/\text{fission}$ and $\sigma_{239} = (4.29 \pm 0.23) \times 10^{-43} \text{cm}^2/\text{fission}$ separately, with a χ^2/NDF of 3.6/6, as shown in Fig. 5.6(b). Now the Huber-Mueller model prediction is outside the 3σ allowed region by the new measurement.

The fit results are summarized in Table 5.9. The new measured σ_{235} is lower than Table 5.9 Comparison of IBD yields per fission for ^{235}U and ^{239}Pu in previous result and new result. The theoretical prediction is from Huber-Mueller model.

	Theoretical prediction	Previous result	New result
$\sigma_{235}(10^{-43} \text{cm}^2/\text{fission})$	6.69 ± 0.15	6.17 ± 0.17	6.19 ± 0.14
$\sigma_{239}(10^{-43} \text{cm}^2/\text{fission})$	4.36 ± 0.11	4.27 ± 0.26	4.29 ± 0.23



(a) Previous result.

(b) New result.

 Figure 5.6 Combined measurement of IBD yields for ^{235}U and ^{239}Pu , σ_{235} and σ_{239} in previous result and new result.

the Huber-Mueller model value, with a deficit of $7.5\% \pm 2.3\%(\text{exp.}) \pm 2.2\%(\text{model})$. The new measured σ_{239} value is consistent with the predicted value within the 5% uncertainty of the measurement, which is relative big compared with the 2.5% model uncertainty.

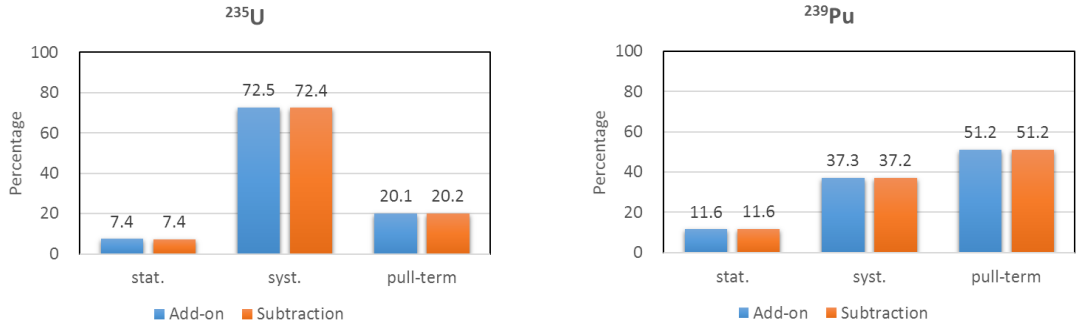
An analysis for the uncertainty budget in fit was done as well. The total uncertainty has three sources: the statistic uncertainty, the systematic uncertainty and the uncertainty from pull terms of ^{238}U and ^{241}Pu constraint. Two estimation methods were used to evaluate the fractional contribution from each source:

- 1) Add-on: $\sigma_{syst.}^2 = \sigma_{stat.+syst.}^2 - \sigma_{stat.}^2$;
- 2) Subtraction: $\sigma_{syst.}^2 = \sigma_{stat.+syst.+pull-term}^2 - \sigma_{stat.+pull-term}^2$.

The results are shown in Fig. 5.7. With a smaller systematic uncertainty in IBD detection efficiency, the fractional systematic uncertainty in total budget in σ_{235} and σ_{239} are both reduced. The pull-terms for ^{238}U and ^{241}Pu constraint now contribute much in the total uncertainty budget, especially for the IBD yield of ^{239}Pu , σ_{239} . This pushes us to have more careful treatment for the pull term in the future study.

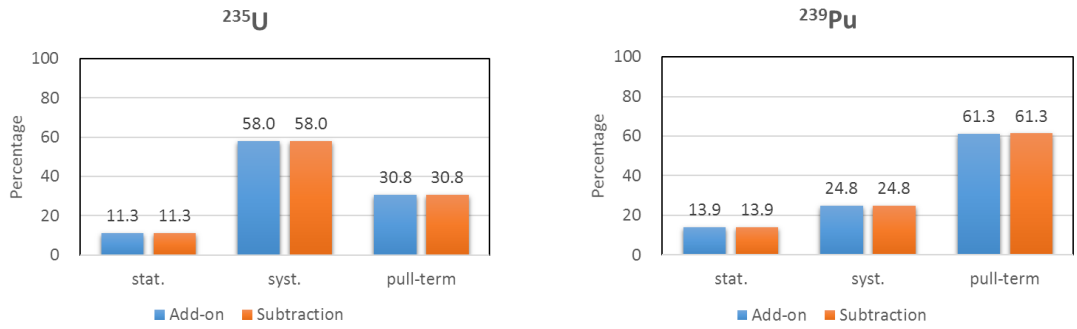
5.1.3 Flux Anomaly at Daya Bay

With the new efficiency and uncertainty, the measured total IBD yield per fission is $\bar{\sigma}_f = (5.92 \pm 0.09) \times 10^{-43} \text{cm}^2/\text{fission}$. The ratio of measured to predicted flux is measured as $0.952 \pm 0.014(\text{exp.}) \pm 0.023(\text{theo.})$ for the Huber-Mueller model. This confirms the reactor antineutrino anomaly in Daya Bay at a confidence level of 1.8σ . In the study of the correlation between the antineutrino flux and the reactor fuel fission, the



(a) σ_{235} uncertainty budget for previous result.

(b) σ_{239} uncertainty budget for previous result.



(c) σ_{235} uncertainty budget for new result.

(d) σ_{239} uncertainty budget for new result.

Figure 5.7 Uncertainty budget of IBD yields for ^{235}U and ^{239}Pu , σ_{235} and σ_{239} . (a) and (b) are the uncertainty budget for the previous result. (c) and (d) are for the new result, with a smaller systematic uncertainty. The blue bars are for add-on method while the red bars for subtraction method.

measured $d\sigma_f/dF_{239}$ derives from the model prediction at 3.1σ confidence level. These discrepancies imply that the present reactor antineutrino flux model has possible issues.

If we trust in the antineutrino flux model and introduce a eV-scale sterile neutrino to explain this flux deficit, the extra oscillation mode due to the sterile neutrino will lead to an equal fractional deficit in IBD yields per fission for all the four primary fissionable isotopes. In this condition, a ratio of $d\sigma_f/dF_{239}$ to $\bar{\sigma}_f$ will have agreement between measurement and model prediction. With the detailed figures in Table 5.8, I calculated the ratios for measurement and prediction as -0.31 ± 0.03 and -0.39 ± 0.01 respectively. These numbers are incompatible at a confidence level of 2.6σ , disfavoring the hypothesis of eV-scale sterile neutrino.

By studying the correlation between the antineutrino flux and the effective fission fractions, I can obtain the individual antineutrino flux for the four primary fissionable isotopes. The IBD yields per fission of ^{235}U and ^{239}Pu are measured to be $(6.19 \pm 0.14) \times$

$10^{-43}\text{cm}^2/\text{fission}$ and $(4.29 \pm 0.23) \times 10^{-43}\text{cm}^2/\text{fission}$ separately with the new efficiency and uncertainty. The combined contour of ^{235}U and ^{239}Pu flux shows that now the Huber-Mueller model prediction is outside of the 3σ allowed region by the measurement. The IBD yield per fission of ^{235}U has a deficit of $7.5\% \pm 2.3\%(\text{exp.}) \pm 2.2\%(\text{model})$ compared with the prediction while that of ^{239}Pu is consistent with the prediction within uncertainty, with a small deficit of $1.4\% \pm 5.3\%(\text{exp.}) \pm 2.5\%(\text{model})$.

Furthermore, to investigate the source of the reactor antineutrino anomaly, I proposed three hypotheses:

- (1) Reactor antineutrino anomaly is caused solely by incorrect predictions of ^{235}U ;
- (2) Reactor antineutrino anomaly is caused solely by incorrect predictions of ^{239}Pu ;
- (3) Reactor antineutrino anomaly is caused by an equal fractional deficit with respect to predictions for all the four isotopes.

We removed the pull term in equation 5-20 and applied corresponding additional constraints to check the hypotheses. For hypotheses (1) and (2), the IBD yields of other isotopes (including ^{238}U and ^{241}Pu) are fixed at their predicted values in model. I compared the χ^2/NDF of the best fit to the original fit result and got the $\Delta\chi^2/\text{NDF}$ for each hypothesis. The results are summarized in Table 5.10. From the table one can find that

Table 5.10 Comparison of $\Delta\chi^2/\text{NDF}$ of hypotheses in the previous result and new result.

$\Delta\chi^2/\text{NDF} (\sigma)$	Previous result	Updated result
Solely by ^{235}U	0.17/1 (0.4 σ)	0.27/1 (0.5 σ)
Solely by ^{239}Pu	10.1/1 (3.2 σ)	20.8/1 (4.6 σ)
Equal fractional deficits	7.9/1 (2.8 σ)	7.9/1 (2.8 σ)

the new result are similar to the previous result. This result favored the hypothesis that ^{235}U is primarily contributor to the reactor flux anomaly. The ^{239}Pu -only deficit and equal fractional deficit hypotheses were disfavored by 4.6σ and 2.8σ separately. Here, the equal fractional deficit hypothesis possibly due to the existence of eV-scale sterile neutrino is disfavored at similar confidence level as in the analysis for the ratio of $d\sigma_f/dF_{239}$ to $\bar{\sigma}_f$ above.

5.2 Reactor Antineutrino Spectrum

5.2.1 Spectrum and Its Evolution

For the antineutrino spectrum measurement, I can get the positron spectrum (prompt spectrum of IBD events) from data directly after subtracting the spectrum of backgrounds, as shown in Fig. 5.8, and then do an unfolding with the detector response to get the antineutrino spectrum inversely. The detector response obtained from MC simulation is

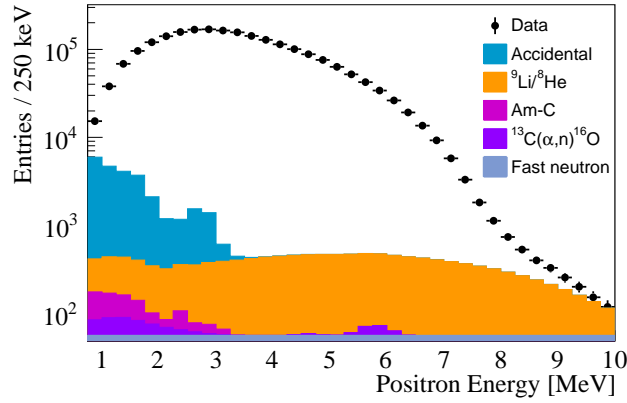


Figure 5.8 The prompt spectra of the raw IBD candidates and backgrounds in data. The spectrum after subtracting all the backgrounds is the detected positron spectrum.

illustrated in Fig., which shows the relationship between the initial antineutrino energy and the reconstructed positron energy.

The predicted antineutrino spectrum in one AD can be obtained by equation (5-5) and (5-6) with the antineutrino spectra for four isotopes in model. The total predicted antineutrino spectrum is the sum of the four near ADs. Considering that the process of applying the detector response to the antineutrino spectrum thus getting the positron spectrum is much easier than the inverse process of unfolding to get the antineutrino spectrum from positron spectrum, I decided to get the positron spectrum in measurement and prediction, and then make a comparison between them. Besides, since the antineutrino energy and corresponding positron energy in IBD reaction has a approximate relationship of $E_{e^+} \approx E_{\bar{\nu}_e} - 0.78\text{MeV}$, the main structures of antineutrino and positron spectra are quite alike. So in this section, I will study the positron spectrum, effectively for the study of antineutrino spectrum.

The measured and predicted positron spectrum from IBD events with 1230 days' data sample are shown in Fig. 5.10, compared with the previous measurement with the

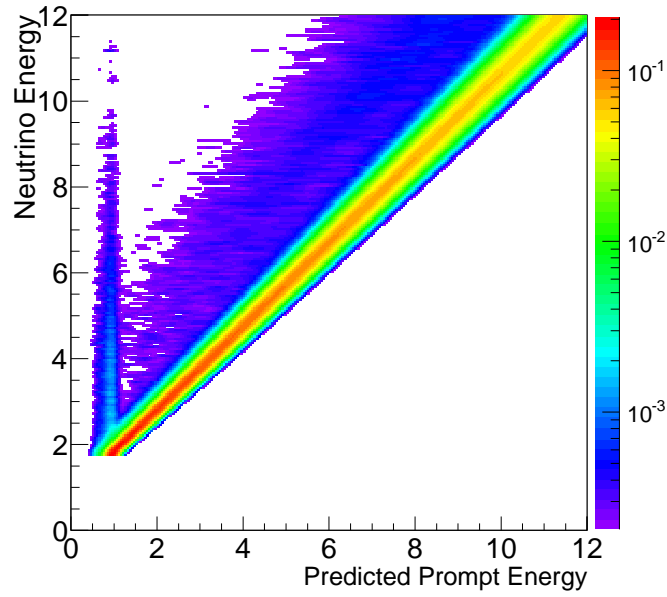


Figure 5.9 The detector response in Daya Bay AD obtained from MC simulation. The y-axis is the initial antineutrino energy, and the y-axis is the reconstructed positron energy. Each row for a given antineutrino energy is normalized, where the positron spectrum is determined by the factors such as energy leakage, energy resolution.

data sample of 621-day livetime^[76]. Similar bump between 4-6 MeV is observed as the previous measurement, and the excess events take $(1.39 \pm 0.04)\%$ of the total spectrum. Considering that the positron spectrum is converted from the antineutrino spectrum as $E_{e^+} \sim E_{\bar{\nu}_e} - 0.78$ MeV including the detector response, this bump in positron spectrum is effectively to a spectral anomaly between 5-7 MeV in the antineutrino spectrum.

Same as the measurement of the antineutrino flux evolution along with reactor fuel fission cycle in Section 5.1.2, I also studied the correlation between the antineutrino spectrum and reaction fuel fission cycle, with the same data grouping by the effective fission fraction F_{239} as in Section 5.1.2. The ratios of measured to predicted antineutrino spectrum in the eight F_{239} bins are shown in Fig. 5.11. We can see that the histograms of ratios in different F_{239} bins are almost consistent with each other within the uncertainty, showing a stable bump in the 4-6 MeV region. In Fig. 5.11, only the statistical uncertainty is included here as the systematic uncertainty for predictions in eight F_{239} bins are correlated. As I have calculated the IBD yields per fission for eight F_{239} bins, the amount of excess events in 4-6 MeV region of prompt spectrum in each F_{239} bin can be converted as an excess in the IBD yield per fission, as shown in Fig. 5.12. The statistical uncertainty for the spectrum excess in each bin is about 10%. This is due to the fact that the excess events takes about 4.5% of the total events in 4-6 MeV region of the measured prompt

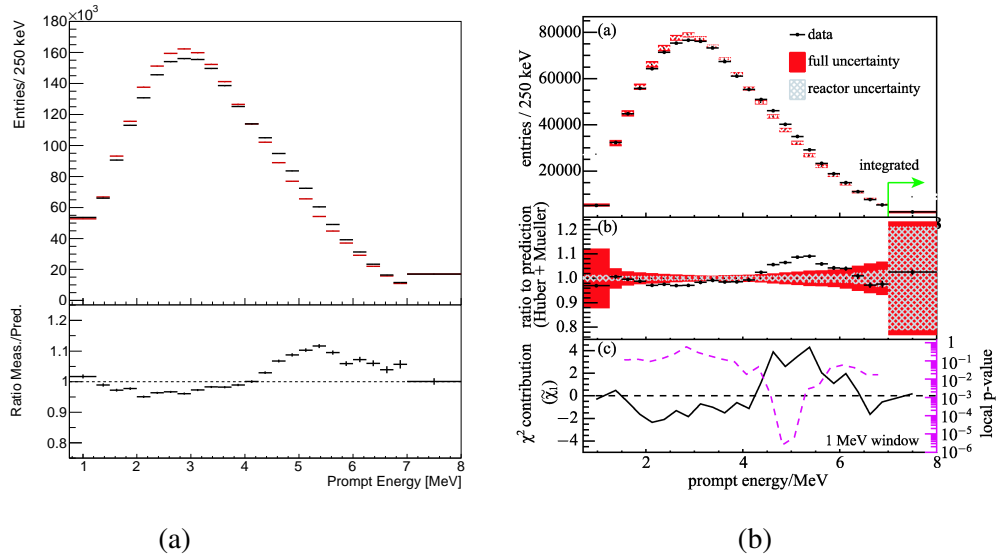


Figure 5.10 Left: Measured prompt spectrum of 1230 days' data sample compared with the Huber-Mueller prediction in the top panel; the ratio of them in the bottom panel. Right: The same comparison as the left but with 621 days' data sample. The right figure from reference^[76].

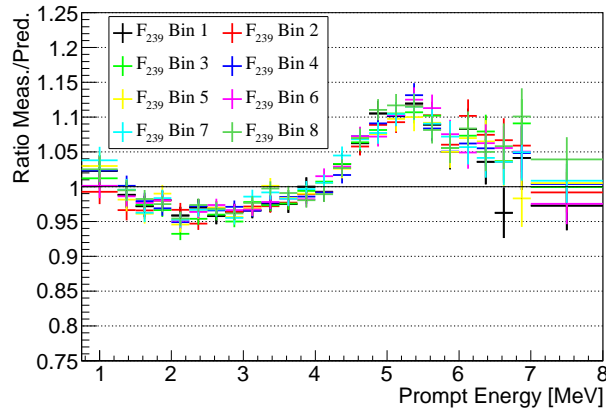


Figure 5.11 The ratios of measured to predicted prompt spectrum in all the eight F_{239} bins.

spectrum while the statistical uncertainty of the number of total events in this region is about 0.45%. The 1.5% systematic uncertainty from IBD detection efficiency and reactor is small compared with this statistical uncertainty. From Fig. 5.12 we can see that the amount of excess in IBD yield per fission looks stable in eight bins, though the effective fission fraction F_{239} has changed from 25.3% to 34.5% with an increase of 36%.

5.2.2 Spectrum Anomaly at Daya Bay

I observed same bump between 4 to 6 MeV in the antineutrino spectrum, same as the previous reactor spectrum anomaly. Moreover, I calculated the excess in IBD yield

per fission for eight F_{239} bins and measured the correlation between these excesses and the reactor fuel fission cycle. The result showed that the excess would not change along with the fuel burn-up within the statistical uncertainty. Since the eV-scale sterile neutrino can only introduce extra oscillation mode to modulate the antineutrino spectrum relying on the term of $\sin \Delta m^2 \frac{L}{E}$, it can not cause a significant bump in 5-7 MeV region in the antineutrino spectrum while have no impact on the other energy region. Thus it can not be the reason to cause the reactor spectrum anomaly. Then the reactor spectrum anomaly may be due to the incorrect modeling of the antineutrino spectrum in the flux models.

To investigate the reason of the bump, four hypotheses were proposed:

- (1) Reactor spectrum anomaly is caused by a common distortion in the antineutrino spectra for all the four isotopes compared with model prediction. This will lead to a constant amount of excess in IBD yield per fission though F_{239} changes.
- (2) Reactor spectrum anomaly is caused by a common distortion in the antineutrino spectra for the four isotopes and additionally ^{239}Pu has an extra distortion compared with model prediction. This will lead to a linear relationship between the amount of excess in IBD yield per fission and F_{239} .
- (3) Reactor spectrum anomaly is caused solely by a distortion in the antineutrino spectrum of ^{239}Pu compared with model prediction. This will lead to a proportional relationship between the amount of excess in IBD yield per fission and F_{239} .
- (4) Reactor spectrum anomaly is caused solely by a distortion in the antineutrino spectrum of ^{235}U compared with model prediction. This will lead to a proportional relationship between the amount of excess in IBD yield per fission and F_{235} .

I applied the four fit to the measured excess amount in IBD yield per fission in eight F_{239} bins, as shown in Fig. 5.12. The fit parameter $\Delta\sigma$ in the proportional function fit with F_{239} and F_{235} are the excesses of IBD yield per fission for bump region in the antineutrino spectrum for ^{239}Pu or ^{235}U respectively.

The fit results are summarized in Table 5.11. From the table we can see that the hypotheses that the reactor spectrum anomaly is caused only by incorrect modeling of antineutrino spectrum for ^{239}Pu or ^{235}U are disfavored at about 2σ confidence levels while the hypothesis that the reactor spectrum anomaly is caused by a common distortion in antineutrino spectra of all the four isotopes is the most favored. This common distortion in antineutrino spectra may be contributed from the same forbidden decays of the fission fragments which have not been involved in the reactor flux model. Eventually it leads to

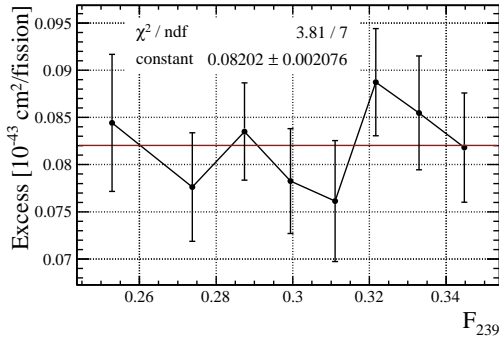
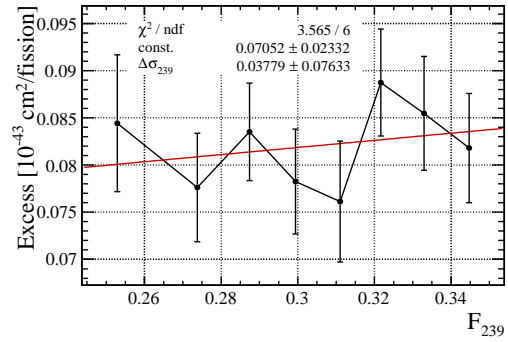
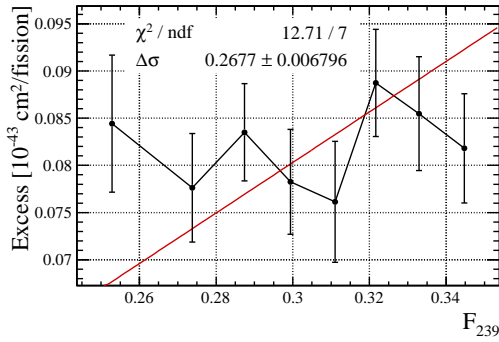
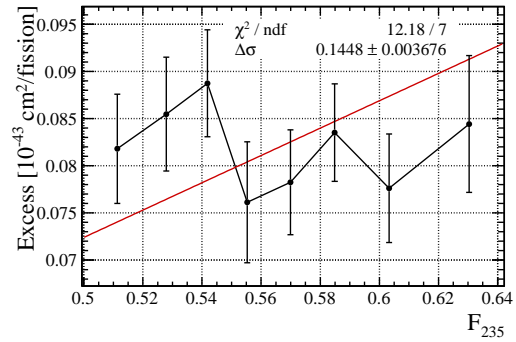

 (a) Constant fit with F_{239}

 (b) Linear function fit with F_{239}

 (c) Proportional function fit with F_{239}

 (d) Proportional function fit with F_{235}

 Figure 5.12 Fit to the measured excess amount in IBD yield per fission in eight F_{239} (F_{235}) bins for the four hypotheses.

a stable bump in the total antineutrino spectra regardless of the fuel burn-up and fission fractions changing.

Table 5.11 Comparison of fit results for the four hypotheses to explain the reactor spectrum anomaly.

	χ^2/NDF (σ)	p -value
Common distortion for all isotopes	3.81/7	0.80
Common distortion + ^{239}Pu	3.57/6	0.74
Solely by ^{239}Pu	12.71/7	0.08
Solely by ^{235}U	12.18/7	0.09

Chapter 6 Summary and Outlook

The Daya Bay reactor neutrino experiment started data-taking with one far experimental hall and two near experimental halls in December, 2011. Each near experimental hall has a pair of antineutrino detectors (ADs). The total four near ADs have minimum baselines to the six 2.9-GWth nuclear power reactor cores down to about 300 m to 500 m. The 3-flavor neutrino oscillation effect is limited at these short baselines, which provide an opportunity to investigate the reactor antineutrino anomalous deficit in flux observed by previous experiments (referred to as “reactor antineutrino anomaly”). This anomaly may be due to systematic effects in the previous experiments, or the incomplete theoretical calculations. Additionally, it has been regarded as an indication of the existence of sterile neutrinos beyond the Standard Model.

We identified the antineutrino event candidates by selecting the prompt signal of positron and delayed signal of neutron capture on gadolinium from the inverse beta decay (IBD) reactions. With a dataset of 1230-day livetime, about 2.2 million antineutrino event candidates were collected by the four near ADs. A measurement of reactor antineutrino flux was performed based on this data sample. I used the ^{241}Am - ^{13}C and ^{241}Am - ^9Be sources to generate neutrons with different kinetic energy and independently simulate the IBD delayed signals inside the detector. The study of the correlations between the delayed spectrum and the neutron captures on various isotopes gave us a comprehensive understanding in the underlying neutron physics, including the processes of neutron propagation in different detector materials and the de-excitation of nuclei after capturing the neutrons. This eventually enabled us to improve the entire agreement between simulations and real detector performance and obtain precision Monte Carlo simulation for the neutron and IBD events. Based on the Monte Carlo simulation and real data, I had an estimation for the absolute IBD detection efficiency as $\epsilon_{\text{IBD}} = (80.25 \pm 0.95)\%$, with a 40% improvement on the efficiency uncertainty in comparison to the previous result of $\epsilon_{\text{IBD}} = (80.60 \pm 1.56)\%$ ^[76].

With this IBD detection efficiency, I measured the reactor antineutrino flux using the number of IBD candidates. The flux was calculated with the average fission fractions for the fissionable isotopes during the data-taking period, and the ratio of the measured antineutrino flux to the Huber-Mueller model prediction is found to be $R = 0.952 \pm$

$0.014(\text{exp.}) \pm 0.023(\text{theo.})$ after the correction of 3-flavor neutrino oscillation ($1 \sim 2\%$). I confirm the reactor antineutrino anomaly at more than 3σ confidence level, in term of experimental uncertainty, which is much better than the theoretical model uncertainty.

In addition, I investigated the correlation between the antineutrino flux and the reactor fuel fission cycle. I found that the correlation was inconsistent with the theoretical model prediction at 2.6σ confidence level, which includes both experimental and theoretical uncertainties. Based on this correlation, the IBD yield from ^{235}U fissions was measured to be $(6.19 \pm 0.14) \times 10^{-43} \text{cm}^2/\text{fission}$, yielding a $(7.5 \pm 2.3(\text{exp.}) \pm 2.2(\text{theo.}))\%$ deficit with respect to the Huber-Mueller model prediction. The mismatches imply that the reactor antineutrino anomaly is likely caused by an improper treatment of correlation and/or an overestimate in the model prediction. The hypothesis of the existence of an eV-scale sterile neutrino, which will lead to an equal fractional deficit in IBD yields per fission for all the four primary fissionable isotopes, is disfavored at about 2.8σ confidence level.

Finally, I conducted a measurement on the antineutrino spectrum with the energy information of the IBD candidates, and compared it with the Huber-Mueller model prediction including the detector response effects. By studying the correlation between the antineutrino spectra and reactor fuel fission cycle, I observed an almost constant excess for the bump of 5-7 MeV in the antineutrino spectra regardless of the fuel evolution. Since the fission fractions of the fissionable isotope of ^{235}U or ^{239}Pu change as large as 20% in the fuel cycle and the antineutrino spectra from these two isotopes are different, this observation disfavors the hypothesis that the bump is caused solely by ^{235}U or ^{239}Pu .

Daya Bay experiment will continue the operation and data-taking till the year of 2020, and at that time more than five millions of IBD event candidates will be collected. This big data sample will improve the measurement precision of $\sin^2 2\theta_{13}$ to 3% and that of Δm_{ee}^2 to 2.5%, and also reduce the statistical uncertainty in the measurement on IBD yield for different fissionable isotopes in the nuclear fuel, in particular, for ^{239}Pu . The investigation of correlation between the antineutrino flux and spectrum with the reactor fuel fission cycle will benefit from the reduced statistic uncertainty as well. Besides the general IBD events of neutron captured on gadolinium, the statistically independent IBD sample with neutron captured on hydrogen collected at the same time can enlarge our statistic by nearly a factor of 2, while the relative large uncertainty due to more backgrounds should be carefully handled with. For the reactor spectrum anomaly, a joint analysis with future highly enriched uranium (HEU) reactor experiments is likely to find

the origin of the bump of 5-7 MeV in the antineutrino spectrum observed by Daya Bay, RENO and Double CHOOZ.

References

- [1] C. Patrignani *et al.* P D G. Review of particle physics[J/OL]. *Chin. Phys. C*, 2016, 40(10): 100001. <https://doi.org/10.1088/1674-1137/40/10/100001>.
- [2] Chadwick J. The intensity distribution in the magnetic spectrum of beta particles from radium (B + C)[J]. *Verh. Phys. Gesell.*, 1914, 16: 383–391.
- [3] Brown L M. The idea of the neutrino[J/OL]. *Phys. Today*, 1978, 31(9): 23–28. <https://doi.org/10.1063/1.2995181>.
- [4] Fermi E. Versuch einer theorie der β -strahlen. i[J/OL]. *Zeitschrift für Physik*, 1934, 88(3-4): 161–177. <https://doi.org/10.1007/bf01351864>.
- [5] Wilson F L. Fermi's theory of beta decay[J/OL]. *Am. J. Phys.*, 1968, 36(12): 1150–1160. <https://doi.org/10.1119/1.1974382>.
- [6] Cowan C L, Reines F, Harrison F B, et al. Detection of the free neutrino: a confirmation[J/OL]. *Science*, 1956, 124(3212): 103–104. <https://doi.org/10.1126/science.124.3212.103>.
- [7] LANL. Celebrating the neutrino[J/OL]. *Los Alamos Science*, 1997, No. 25. <http://la-science.lanl.gov/lascience25.shtml>.
- [8] Danby G, Gaillard J M, Goulianos K, et al. Observation of high-energy neutrino reactions and the existence of two kinds of neutrinos[J/OL]. *Phys. Rev. Lett.*, 1962, 9(1): 36–44. <https://doi.org/10.1103/physrevlett.9.36>.
- [9] Fermilab. Physicists find first direct evidence for tau neutrino at fermilab[EB/OL]. 2000. <http://news.fnal.gov/2000/07/physicists-find-first-direct-evidence-tau-neutrino-fermilab/>.
- [10] Kodama K, Ushida N, Andreopoulos C, et al. Observation of tau neutrino interactions[J/OL]. *Phys. Lett. B*, 2001, 504(3): 218–224. [https://doi.org/10.1016/s0370-2693\(01\)00307-0](https://doi.org/10.1016/s0370-2693(01)00307-0).
- [11] Goldhaber M, Grodzins L, Sunyar A W. Helicity of neutrinos[J/OL]. *Phys. Rev.*, 1958, 109(3): 1015–1017. <https://doi.org/10.1103/physrev.109.1015>.
- [12] Pontecorvo B. Mesonium and antimesonium[J/OL]. *J. Exp. Theor. Phys.*, 1958, 6(2): 429. <http://www.jetp.ac.ru/cgi-bin/e/index/e/6/2/p429?a=list>.
- [13] Maki Z, Nakagawa M, Sakata S. Remarks on the unified model of elementary particles[J/OL]. *Progr. Theor. Exp. Phys.*, 1962, 28(5): 870–880. <https://doi.org/10.1143/ptp.28.870>.
- [14] Pontecorvo B. Neutrino experiments and the problem of conservation of leptonic charge[J/OL]. *J. Exp. Theor. Phys.*, 1968, 26(5): 984. <http://www.jetp.ac.ru/cgi-bin/e/index/e/26/5/p984?a=list>.
- [15] Wolfenstein L. Neutrino oscillations in matter[J/OL]. *Phys. Rev. D*, 1978, 17(9): 2369–2374. <https://doi.org/10.1103/physrevd.17.2369>.
- [16] Wolfenstein L. Neutrino oscillations and stellar collapse[J/OL]. *Phys. Rev. D*, 1979, 20(10): 2634–2635. <https://doi.org/10.1103/physrevd.20.2634>.
- [17] Mikheev S P, Smirnov A Yu. Resonance amplification of oscillations in matter and spectroscopy of solar neutrinos[J]. *Phys. At. Nucl.*, 1985, 42: 913–917.

- [18] Bethe H A. Possible explanation of the solar-neutrino puzzle[J/OL]. *Phys. Rev. Lett.*, 1986, 56 (12): 1305–1308. <https://doi.org/10.1103/physrevlett.56.1305>.
- [19] Rosen S P, Gelb J M. Mikheyev-smirnov-wolfenstein enhancement of oscillations as a possible solution to the solar-neutrino problem[J/OL]. *Phys. Rev. D*, 1986, 34(4): 969–979. <https://doi.org/10.1103/physrevd.34.969>.
- [20] S. Schael *et al.* Precision electroweak measurements on the Z resonance[J/OL]. *Phys. Rep.*, 2006, 427(5-6): 257–454. <https://doi.org/10.1016/j.physrep.2005.12.006>.
- [21] Giunti C, Kim C W. Fundamentals of neutrino physics and astrophysics[M]. Oxford: Oxford University Press, 2007: 262–360
- [22] Bilenky S, Hošek J, Petcov S. On the oscillations of neutrinos with dirac and majorana masses [J/OL]. *Phys. Lett. B*, 1980, 94(4): 495–498. [https://doi.org/10.1016/0370-2693\(80\)90927-2](https://doi.org/10.1016/0370-2693(80)90927-2).
- [23] Capozzi F, Lisi E, Marrone A, et al. Neutrino masses and mixings: Status of known and unknown 3 ν parameters[J/OL]. *Nucl. Phys. B*, 2016, 908: 218–234. <https://doi.org/10.1016/j.nuclphysb.2016.02.016>.
- [24] An F P, *et al.* Observation of electron-antineutrino disappearance at daya bay[J/OL]. *Phys. Rev. Lett.*, 2012, 108(17). <https://doi.org/10.1103/physrevlett.108.171803>.
- [25] Fukuda Y, *et al.* Evidence for oscillation of atmospheric neutrinos[J/OL]. *Phys. Rev. Lett.*, 1998, 81(8): 1562–1567. <https://doi.org/10.1103/physrevlett.81.1562>.
- [26] Eguchi K, Enomoto S, Furuno K, et al. First results from KamLAND: Evidence for reactor antineutrino disappearance[J/OL]. *Phys. Rev. Lett.*, 2003, 90(2). <https://doi.org/10.1103/physrevlett.90.021802>.
- [27] Araki T, *et al.* Measurement of neutrino oscillation with KamLAND: Evidence of spectral distortion[J/OL]. *Phys. Rev. Lett.*, 2005, 94(8). <https://doi.org/10.1103/physrevlett.94.081801>.
- [28] James M. Energy released in fission[J/OL]. *J. Nucl. Energy*, 1969, 23(9): 517–536. [https://doi.org/10.1016/0022-3107\(69\)90042-2](https://doi.org/10.1016/0022-3107(69)90042-2).
- [29] Apollonio M, Baldini A, Bemporad C, et al. Search for neutrino oscillations on a long baseline at the Chooz nuclear power station[J/OL]. *Eur. Phys. J. C*, 2003, 27(3): 331–374. <https://doi.org/10.1140/epjc/s2002-01127-9>.
- [30] Bemporad C, Gratta G, Vogel P. Reactor-based neutrino oscillation experiments[J/OL]. *Rev. Mod. Phys.*, 2002, 74(2): 297–328. <https://doi.org/10.1103/revmodphys.74.297>.
- [31] Huber P. Determination of antineutrino spectra from nuclear reactors[J/OL]. *Phys. Rev. C*, 2011, 84(2). <https://doi.org/10.1103/physrevc.84.024617>.
- [32] Mueller T A, Lhuillier D, Fallot M, et al. Improved predictions of reactor antineutrino spectra [J/OL]. *Phys. Rev. C*, 2011, 83(5). <https://doi.org/10.1103/physrevc.83.054615>.
- [33] Vogel P, Beacom J F. Angular distribution of neutron inverse beta decay, $\bar{\nu}_e + p \rightarrow e^+ + n$ [J/OL]. *Phys. Rev. D*, 1999, 60(5). <https://doi.org/10.1103/physrevd.60.053003>.
- [34] Parke S. What is Δm_{ee}^2 ?[J/OL]. *Phys. Rev. D*, 2016, 93(5). <https://doi.org/10.1103/physrevd.93.053008>.
- [35] Boehm F, Busenitz J, Cook B, et al. Final results from the palo verde neutrino oscillation experiment[J/OL]. *Phys. Rev. D*, 2001, 64(11). <https://doi.org/10.1103/physrevd.64.112001>.

- [36] Mikaélyan L A, Sinev V V. Neutrino oscillations at reactors: What is next?[J/OL]. Phys. Atom. Nuclei, 2000, 63(6): 1002–1006. <https://doi.org/10.1134/1.855739>.
- [37] Abe K, *et al.* Indication of electron neutrino appearance from an accelerator-produced off-axis muon neutrino beam[J/OL]. Phys. Rev. Lett., 2011, 107(4). <https://doi.org/10.1103/physrevlett.107.041801>.
- [38] Abe Y, Aberle C, Akiri T, *et al.* Indication of reactor $\bar{\nu}_e$ disappearance in the double chooz experiment[J/OL]. Phys. Rev. Lett., 2012, 108(13). <https://doi.org/10.1103/physrevlett.108.131801>.
- [39] Ahn J K, Chebotaryov S, Choi J H, *et al.* Observation of reactor electron antineutrinos disappearance in the RENO experiment[J/OL]. Phys. Rev. Lett., 2012, 108(19). <https://doi.org/10.1103/physrevlett.108.191802>.
- [40] An F P, *et al.* Measurement of electron antineutrino oscillation based on 1230 days of operation of the daya bay experiment[J/OL]. Phys. Rev. D, 2017, 95(7). <https://doi.org/10.1103/physrevd.95.072006>.
- [41] Minkowski P. $\mu \rightarrow e\gamma$ at a rate of one out of 10^9 muon decays?[J/OL]. Phys. Lett. B, 1977, 67(4): 421–428. [https://doi.org/10.1016/0370-2693\(77\)90435-x](https://doi.org/10.1016/0370-2693(77)90435-x).
- [42] Mohapatra R N, Senjanović G. Neutrino mass and spontaneous parity nonconservation[J/OL]. Phys. Rev. Lett., 1980, 44(14): 912–915. <https://doi.org/10.1103/physrevlett.44.912>.
- [43] Dib C O, Kim C. Discovering sterile neutrinos lighter than M_W at the LHC[J/OL]. Phys. Rev. D, 2015, 92(9). <https://doi.org/10.1103/physrevd.92.093009>.
- [44] Dodelson S, Widrow L M. Sterile neutrinos as dark matter[J/OL]. Phys. Rev. Lett., 1994, 72(1): 17–20. <https://doi.org/10.1103/physrevlett.72.17>.
- [45] Gandhi R, Kayser B, Masud M, *et al.* The impact of sterile neutrinos on CP measurements at long baselines[J/OL]. J. High Energy Phys., 2015, 2015(11). [https://doi.org/10.1007/jhep11\(2015\)039](https://doi.org/10.1007/jhep11(2015)039).
- [46] Dell’Oro S, Marcocci S, Viel M, *et al.* Neutrinoless double beta decay: 2015 review[J/OL]. Adv. High Energy Phys., 2016, 2016: 1–37. <https://doi.org/10.1155/2016/2162659>.
- [47] Giunti C, Zavanin E M. Predictions for neutrinoless double-beta decay in the 3+1 sterile neutrino scenario[J/OL]. J. High Energy Phys., 2015, 2015(7). [https://doi.org/10.1007/jhep07\(2015\)171](https://doi.org/10.1007/jhep07(2015)171).
- [48] Athanassopoulos C, Auerbach L B, Burman R L, *et al.* Results on $\nu_\mu \rightarrow \nu_e$ neutrino oscillations from the LSND experiment[J/OL]. Phys. Rev. Lett., 1998, 81(9): 1774–1777. <https://doi.org/10.1103/physrevlett.81.1774>.
- [49] Aguilar A, Auerbach L B, Burman R L, *et al.* Evidence for neutrino oscillations from the observation of $\bar{\nu}_e$ appearance in a $\bar{\nu}_\mu$ beam[J/OL]. Phys. Rev. D, 2001, 64(11). <https://doi.org/10.1103/physrevd.64.112007>.
- [50] Aguilar-Arevalo A A, Brown B C, Bugel L, *et al.* Improved search for $\bar{\nu}_\mu \rightarrow \bar{\nu}_e$ oscillations in the MiniBooNE experiment[J/OL]. Phys. Rev. Lett., 2013, 110(16). <https://doi.org/10.1103/physrevlett.110.161801>.
- [51] Armbruster B, Blair I M, Bodmann B A, *et al.* Upper limits for neutrino oscillations $\bar{\nu}_\mu \rightarrow \bar{\nu}_e$ from muon decay at rest[J/OL]. Phys. Rev. D, 2002, 65(11). <https://doi.org/10.1103/physrevd.65.112001>.

- [52] Antonello M, Baibussinov B, Benetti P, et al. Experimental search for the LSND anomaly with the ICARUS detector in the CNGS neutrino beam[J/OL]. *Eur. Phys. J. C*, 2013, 73(3). <https://doi.org/10.1140/epjc/s10052-013-2345-6>.
- [53] Astier P, *et al.* Search for $\nu_\mu \rightarrow \nu_e$ oscillations in the NOMAD experiment[J/OL]. *Phys. Lett. B*, 2003, 570(1-2): 19–31. <https://doi.org/10.1016/j.physletb.2003.07.029>.
- [54] Huang E C. Precise measurement of mixing parameters and sterile neutrino search at daya bay [D]. USA: University of Illinois at Urbana-Champaign, 2016.
- [55] Abdurashitov J N, Gavrin V N, Gorbachev V V, et al. Measurement of the solar neutrino capture rate with gallium metal. III. results for the 2002-2007 data-taking period[J/OL]. *Phys. Rev. C*, 2009, 80(1). <https://doi.org/10.1103/physrevc.80.015807>.
- [56] Kaether F, Hampel W, Heusser G, et al. Reanalysis of the gallex solar neutrino flux and source experiments[J/OL]. *Phys. Lett. B*, 2010, 685(1): 47–54. <https://doi.org/10.1016/j.physletb.2010.01.030>.
- [57] Kopp J, Machado P A N, Maltoni M, et al. Sterile neutrino oscillations: the global picture [J/OL]. *J. High Energy Phys.*, 2013, 2013(5). [https://doi.org/10.1007/jhep05\(2013\)050](https://doi.org/10.1007/jhep05(2013)050).
- [58] Abazajian K N, *et al.* Light sterile neutrinos: A white paper[EB/OL]. 2012. <https://arxiv.org/abs/1204.5379>.
- [59] Giunti C, Laveder M. Short-baseline electron neutrino disappearance, tritium beta decay, and neutrinoless double-beta decay[J/OL]. *Phys. Rev. D*, 2010, 82(5). <https://doi.org/10.1103/physrevd.82.053005>.
- [60] Mention G, Fechner M, Lasserre T, et al. Reactor antineutrino anomaly[J/OL]. *Phys. Rev. D*, 2011, 83(7). <https://doi.org/10.1103/physrevd.83.073006>.
- [61] Huber P. Reactor antineutrino fluxes - status and challenges[J/OL]. *Nucl. Phys. B*, 2016, 908: 268–278. <https://doi.org/10.1016/j.nuclphysb.2016.04.012>.
- [62] Carter R E, Reines F, Wagner J J, et al. Free antineutrino absorption cross section. II. expected cross section from measurements of fission fragment electron spectrum[J/OL]. *Phys. Rev.*, 1959, 113(1): 280–286. <https://doi.org/10.1103/physrev.113.280>.
- [63] von Feilitzsch F, Hahn A, Schreckenbach K. Experimental beta-spectra from ^{239}Pu and ^{235}U thermal neutron fission products and their correlated antineutrino spectra[J/OL]. *Phys. Lett. B*, 1982, 118(1-3): 162–166. [https://doi.org/10.1016/0370-2693\(82\)90622-0](https://doi.org/10.1016/0370-2693(82)90622-0).
- [64] Schreckenbach K, Colvin G, Gelletly W, et al. Determination of the antineutrino spectrum from ^{235}U thermal neutron fission products up to 9.5 MeV[J/OL]. *Phys. Lett. B*, 1985, 160(4-5): 325–330. [https://doi.org/10.1016/0370-2693\(85\)91337-1](https://doi.org/10.1016/0370-2693(85)91337-1).
- [65] Hahn A, Schreckenbach K, Gelletly W, et al. Antineutrino spectra from ^{241}Pu and ^{239}Pu thermal neutron fission products[J/OL]. *Phys. Lett. B*, 1989, 218(3): 365–368. [https://doi.org/10.1016/0370-2693\(89\)91598-0](https://doi.org/10.1016/0370-2693(89)91598-0).
- [66] Vogel P, Schenter G K, Mann F M, et al. Reactor antineutrino spectra and their application to antineutrino-induced reactions. II[J/OL]. *Phys. Rev. C*, 1981, 24(4): 1543–1553. <https://doi.org/10.1103/physrevc.24.1543>.
- [67] Achkar B, Aleksan R, Avenier M, et al. Comparison of anti-neutrino reactor spectrum models with the Bugey 3 measurements[J/OL]. *Phys. Lett. B*, 1996, 374(1-3): 243–248. [https://doi.org/10.1016/0370-2693\(96\)00216-x](https://doi.org/10.1016/0370-2693(96)00216-x).

- [68] Hayes A C, Vogel P. Reactor neutrino spectra[J/OL]. *Annu. Rev. Nucl. Part. Sci.*, 2016, 66(1): 219–244. <https://doi.org/10.1146/annurev-nucl-102115-044826>.
- [69] M.A. Kellett O B, Mills R. The JEFF-3.1/-3.1.1 Radioactive Decay Data and Fission Yields Sub-libraries JEFF Report 20[R/OL]. Nuclear Energy Agency, 2009. https://www.oecd-nea.org/dbdata/nds_jefreports/jefreport-20/nea6287-jeff-20.pdf.
- [70] Chadwick M, Herman M, Obložinský P, et al. ENDF/b-VII.1 nuclear data for science and technology: Cross sections, covariances, fission product yields and decay data[J/OL]. *Nuclear Data Sheets*, 2011, 112(12): 2887–2996. <https://doi.org/10.1016/j.nds.2011.11.002>.
- [71] Sonzogni A, McCutchan E, Johnson T, et al. Effects of fission yield data in the calculation of antineutrino spectra for $^{235}\text{U}(n, \text{fission})$ at thermal and fast neutron energies[J/OL]. *Phys. Rev. Lett.*, 2016, 116(13). <https://doi.org/10.1103/physrevlett.116.132502>.
- [72] Fallot M, Cormon S, Estienne M, et al. New antineutrino energy spectra predictions from the summation of beta decay branches of the fission products[J/OL]. *Phys. Rev. Lett.*, 2012, 109(20). <https://doi.org/10.1103/physrevlett.109.202504>.
- [73] Haag N, Gütlein A, Hofmann M, et al. Experimental determination of the antineutrino spectrum of the fission products of ^{238}U [J/OL]. *Phys. Rev. Lett.*, 2014, 112(12). <https://doi.org/10.1103/physrevlett.112.122501>.
- [74] Hayes A, Friar J, Garvey G, et al. Systematic uncertainties in the analysis of the reactor neutrino anomaly[J/OL]. *Phys. Rev. Lett.*, 2014, 112(20). <https://doi.org/10.1103/physrevlett.112.202501>.
- [75] Wietfeldt F E, Greene G L. Colloquium: The neutron lifetime[J/OL]. *Rev. Mod. Phys.*, 2011, 83(4): 1173–1192. <https://doi.org/10.1103/revmodphys.83.1173>.
- [76] An F P, *et al.* Improved measurement of the reactor antineutrino flux and spectrum at daya bay [J/OL]. *Chin. Phys. C*, 2017, 41(1): 013002. <https://doi.org/10.1088/1674-1137/41/1/013002>.
- [77] and E K. Precise measurement of reactor antineutrino spectrum flux and spectrum at RENO [J/OL]. *J. Phys. Conf. Ser.*, 2017, 888: 012137. <https://doi.org/10.1088/1742-6596/888/1/012137>.
- [78] Abe Y, *et al.* Measurement of θ_{13} in double chooz using neutron captures on hydrogen with novel background rejection techniques[J/OL]. *J. High Energy Phys.*, 2016, 2016(1). [https://doi.org/10.1007/jhep01\(2016\)163](https://doi.org/10.1007/jhep01(2016)163).
- [79] Choi J, Choi W, Choi Y, et al. Observation of energy and baseline dependent reactor antineutrino disappearance in the RENO experiment[J/OL]. *Phys. Rev. Lett.*, 2016, 116(21). <https://doi.org/10.1103/physrevlett.116.211801>.
- [80] Abe Y, *et al.* Improved measurements of the neutrino mixing angle θ_{13} with the double chooz detector[J/OL]. *J. High Energy Phys.*, 2014, 2014(10). [https://doi.org/10.1007/jhep10\(2014\)086](https://doi.org/10.1007/jhep10(2014)086).
- [81] Hayes A, Friar J, Garvey G, et al. Possible origins and implications of the shoulder in reactor neutrino spectra[J/OL]. *Phys. Rev. D*, 2015, 92(3). <https://doi.org/10.1103/physrevd.92.033015>.
- [82] Dwyer D, Langford T. Spectral structure of electron antineutrinos from nuclear reactors[J/OL]. *Phys. Rev. Lett.*, 2015, 114(1). <https://doi.org/10.1103/physrevlett.114.012502>.

- [83] Huber P. NEOS data and the origin of the 5 MeV bump in the reactor antineutrino spectrum [J/OL]. *Phys. Rev. Lett.*, 2017, 118(4). <https://doi.org/10.1103/physrevlett.118.042502>.
- [84] Buck C, Collin A, Haser J, et al. Investigating the spectral anomaly with different reactor antineutrino experiments[J/OL]. *Phys. Lett. B*, 2017, 765: 159–162. <https://doi.org/10.1016/j.physletb.2016.11.062>.
- [85] Ashenfelter J, Balantekin A B, Band H R, et al. The PROSPECT physics program[J/OL]. *J. Phys. G*, 2016, 43(11): 113001. <https://doi.org/10.1088/0954-3899/43/11/113001>.
- [86] Cao J, Luk K B. An overview of the daya bay reactor neutrino experiment[J/OL]. *Nucl. Phys. B*, 2016, 908: 62–73. <https://doi.org/10.1016/j.nuclphysb.2016.04.034>.
- [87] An F P, *et al.* New measurement of θ_{13} via neutron capture on hydrogen at daya bay[J/OL]. *Phys. Rev. D*, 2016, 93(7). <https://doi.org/10.1103/physrevd.93.072011>.
- [88] An F, *et al.* Search for a light sterile neutrino at daya bay[J/OL]. *Phys. Rev. Lett.*, 2014, 113 (14). <https://doi.org/10.1103/physrevlett.113.141802>.
- [89] An F P, *et al.* Improved search for a light sterile neutrino with the full configuration of the daya bay experiment[J/OL]. *Phys. Rev. Lett.*, 2016, 117(15). <https://doi.org/10.1103/physrevlett.117.151802>.
- [90] Adamson P, *et al.* Limits on active to sterile neutrino oscillations from disappearance searches in the MINOS, daya bay, and bugey-3 experiments[J/OL]. *Phys. Rev. Lett.*, 2016, 117(15). <https://doi.org/10.1103/physrevlett.117.151801>.
- [91] An F P, *et al.* Measurement of the reactor antineutrino flux and spectrum at daya bay[J/OL]. *Phys. Rev. Lett.*, 2016, 116(6). <https://doi.org/10.1103/physrevlett.116.061801>.
- [92] An F P, *et al.* Evolution of the reactor antineutrino flux and spectrum at daya bay[J/OL]. *Phys. Rev. Lett.*, 2017, 118(25). <https://doi.org/10.1103/physrevlett.118.251801>.
- [93] An F P, *et al.* Study of the wave packet treatment of neutrino oscillation at daya bay[J/OL]. *Eur. Phys. J. C*, 2017, 77(9). <https://doi.org/10.1140/epjc/s10052-017-4970-y>.
- [94] An F P, *et al.* Cosmogenic neutron production at daya bay[EB/OL]. 2017. <https://arxiv.org/abs/1711.00588v1>.
- [95] An F P, *et al.* The detector system of the daya bay reactor neutrino experiment[J/OL]. *Nucl. Instr. Meth. Phys. Res. A*, 2016, 811: 133–161. <https://doi.org/10.1016/j.nima.2015.11.144>.
- [96] An F P, *et al.* A side-by-side comparison of daya bay antineutrino detectors[J/OL]. *Nucl. Instr. Meth. Phys. Res. A*, 2012, 685: 78–97. <https://doi.org/10.1016/j.nima.2012.05.030>.
- [97] Ding Y, Zhang Z, Liu J, et al. A new gadolinium-loaded liquid scintillator for reactor neutrino detection[J/OL]. *Nucl. Instr. Meth. Phys. Res. A*, 2008, 584(1): 238–243. <https://doi.org/10.1016/j.nima.2007.09.044>.
- [98] Birks J B. Scintillations from organic crystals: Specific fluorescence and relative response to different radiations[J/OL]. *Proc. Phys. Soc. A*, 1951, 64(10): 874–877. <https://doi.org/10.1088/0370-1298/64/10/303>.
- [99] Birks J B. The theory and practice of scintillation counting[M]. Oxford: Pergamon Press, 1964: 278–312

- [100] Xiao H L, Li X B, Zheng D, et al. Study of absorption and re-emission processes in a ternary liquid scintillation system[J/OL]. *Chin. Phys. C*, 2010, 34(11): 1724–1728. <https://doi.org/10.1088/1674-1137/34/11/011>.
- [101] Cherenkov P. Visible luminescence of pure liquids under the influence of γ -radiation[J/OL]. *Uspekhi Fizicheskikh Nauk*, 1967, 93(10): 385–388. <https://doi.org/10.3367/ufnr.0093.196710n.0385>.
- [102] An F P, *et al.* The muon system of the daya bay reactor antineutrino experiment[J/OL]. *Nucl. Instr. Meth. Phys. Res. A*, 2015, 773: 8–20. <https://doi.org/10.1016/j.nima.2014.09.070>.
- [103] Xu J L, Guan M Y, Yang C G, et al. Design and preliminary test results of daya bay RPC modules [J/OL]. *Chin. Phys. C*, 2011, 35(9): 844–850. <https://doi.org/10.1088/1674-1137/35/9/011>.
- [104] Ma L, Lebanowski L, Chen J, et al. The mass production and quality control of RPCs for the daya bay experiment[J/OL]. *Nucl. Instr. Meth. Phys. Res. A*, 2011, 659(1): 154–160. <https://doi.org/10.1016/j.nima.2011.03.060>.
- [105] Ma L H, Wang Y F, Zhang J W, et al. Study of RPC gas composition using daya bay RPCs [J/OL]. *Chin. Phys. C*, 2010, 34(8): 1116–1121. <https://doi.org/10.1088/1674-1137/34/8/015>.
- [106] An F P, *et al.* A precision measurement of the neutrino mixing angle θ_{13} using reactor antineutrinos at daya bay[EB/OL]. 2007. <https://arxiv.org/abs/hep-ex/0701029>.
- [107] Liu J, Cai B, Carr R, et al. Automated calibration system for a high-precision measurement of neutrino mixing angle θ_{13} with the daya bay antineutrino detectors[J/OL]. *Nucl. Instr. Meth. Phys. Res. A*, 2014, 750: 19–37. <https://doi.org/10.1016/j.nima.2014.02.049>.
- [108] Liu J, Carr R, Dwyer D, et al. Neutron calibration sources in the daya bay experiment[J/OL]. *Nucl. Instr. Meth. Phys. Res. A*, 2015, 797: 260–264. <https://doi.org/10.1016/j.nima.2015.07.003>.
- [109] Gu W, Cao G, Chen X, et al. Background evaluation for the neutron sources in the daya bay experiment[J/OL]. *Nucl. Instr. Meth. Phys. Res. A*, 2016, 833: 27–32. <https://doi.org/10.1016/j.nima.2016.07.007>.
- [110] Zhang Q, Wang Y, Zhang J, et al. An underground cosmic-ray detector made of RPC[J/OL]. *Nucl. Instr. Meth. Phys. Res. A*, 2007, 583(2-3): 278–284. <https://doi.org/10.1016/j.nima.2007.09.052>.
- [111] An F, *et al.* A side-by-side comparison of daya bay antineutrino detectors[J/OL]. *Nucl. Instr. Meth. Phys. Res. A*, 2012, 685: 78–97. <https://doi.org/10.1016/j.nima.2012.05.030>.
- [112] An F P, *et al.* Spectral measurement of electron antineutrino oscillation amplitude and frequency at daya bay[J/OL]. *Phys. Rev. Lett.*, 2014, 112(6). <https://doi.org/10.1103/physrevlett.112.061801>.
- [113] An F P, *et al.* New measurement of antineutrino oscillation with the full detector configuration at daya bay[J/OL]. *Phys. Rev. Lett.*, 2015, 115(11). <https://doi.org/10.1103/physrevlett.115.111802>.
- [114] An F P, *et al.* Independent measurement of the neutrino mixing angle θ_{13} via neutron capture on hydrogen at daya bay[J/OL]. *Phys. Rev. D*, 2014, 90(7). <https://doi.org/10.1103/physrevd.90.071101>.

- [115] M.J. Berger M Z, J.S. Coursey, Chang J. Stopping-Power & Range Tables for Electrons, Protons, and Helium Ions[R/OL]. National Institute of Standards and Technology, 2017. <https://www.nist.gov/pml/stopping-power-range-tables-electrons-protons-and-helium-ions>.
- [116] Agostinelli S, Allison J, Amako K, et al. Geant4—a simulation toolkit[J/OL]. Nucl. Instr. Meth. Phys. Res. A, 2003, 506(3): 250–303. [https://doi.org/10.1016/s0168-9002\(03\)01368-8](https://doi.org/10.1016/s0168-9002(03)01368-8).
- [117] Allison J, Amako K, Apostolakis J, et al. Geant4 developments and applications[J/OL]. IEEE Transactions on Nuclear Science, 2006, 53(1): 270–278. <https://doi.org/10.1109/tns.2006.869826>.
- [118] Allison J, Amako K, Apostolakis J, et al. Recent developments in geant 4[J/OL]. Nucl. Instr. Meth. Phys. Res. A, 2016, 835: 186–225. <https://doi.org/10.1016/j.nima.2016.06.125>.
- [119] Krasznahorkay A, et al. Lepton pairs from a forbidden M0 transition: Signaling an elusive light neutral boson?[J]. Acta Phys. Polon., 2006, B37: 239–244.
- [120] MacFarlane R. New thermal neutron scattering files for ENDF/b-VI release 2[R/OL]. Office of Scientific and Technical Information (OSTI), 1994. <https://doi.org/10.2172/10192168>.
- [121] Bhat M R. Evaluated nuclear structure data file (ENSDF)[M/OL]/Nuclear Data for Science and Technology. Springer Berlin Heidelberg, 1992: 817–821. https://doi.org/10.1007/978-3-642-58113-7_227
- [122] Groshev L, Demidov A, Pelekhov V, et al. Compendium of thermal-neutron-capture γ -ray measurements part II $z = 47$ to $z = 67$ (ag to ho)[J/OL]. Nuclear Data Sheets. Section A, 1968, 5(1-2): 1–242. [https://doi.org/10.1016/s0550-306x\(68\)80008-4](https://doi.org/10.1016/s0550-306x(68)80008-4).
- [123] Cheng J H, Wang Z, Lebanowski L, et al. Determination of the total absorption peak in an electromagnetic calorimeter[J/OL]. Nucl. Instr. Meth. Phys. Res. A, 2016, 827: 165–170. <https://doi.org/10.1016/j.nima.2016.05.010>.
- [124] Ma X B, Zhong W L, Wang L Z, et al. Improved calculation of the energy release in neutron-induced fission[J/OL]. Phys. Rev. C, 2013, 88(1). <https://doi.org/10.1103/physrevc.88.014605>.
- [125] Kopeikin V I. Flux and spectrum of reactor antineutrinos[J/OL]. Phys. Atom. Nuclei, 2012, 75 (2): 143–152. <https://doi.org/10.1134/s1063778812020123>.
- [126] Declais Y, de Kerret H, Lefèvre B, et al. Study of reactor antineutrino interaction with proton at bugey nuclear power plant[J/OL]. Phys. Lett. B, 1994, 338(2-3): 383–389. [https://doi.org/10.1016/0370-2693\(94\)91394-3](https://doi.org/10.1016/0370-2693(94)91394-3).
- [127] Giunti C. Precise Determination of the U-235 Reactor Antineutrino Cross Section per Fission [C/OL]/12th Workshop on Applied Antineutrino Physics (AAP 2016) Liverpool, UK, December 1-2, 2016. 2017. <https://inspirehep.net/record/1513295/files/arXiv:1702.04139.pdf>.
- [128] Sanchez R, Zmijarevic I, Coste-Delclaux M, et al. APOLLO2 YEAR 2010[J/OL]. Nucl. Eng. Technol., 2010, 42(5): 474–499. <https://doi.org/10.5516/NET.2010.42.5.474>.
- [129] An F P, *et al.* Electron-antineutrino Disappearance Observed by the Daya Bay Reactor Neutrino Experiment[J/OL]. Nuclear Data Sheets, 2014, 118: 91–97. <https://doi.org/10.1016/j.nds.2014.04.009>.

Acknowledgement

First of all, I would like to express great gratitude to my supervisor Prof. Shaomin Chen and Assoc. Prof. Zhe Wang. I do need to thank them for their guidance and help in my PhD study, work and life. I have been deeply inspired and encouraged by their intelligence, experiences and kindness.

Secondly, I would like to thank Prof. Yuanning Gao, Assoc. Prof. Zhenwei Yang, and Assoc. Prof. Xianglei Zhu for their thought-provoking and constructive suggestions and kind help in many respects in my PhD life. Special thanks are given to Prof. Jianglai Liu and Wenqiang Gu from Shanghai Jiao Tong University as they have provided me a lot of useful discussions and valuable help.

Moreover, I would like to thank my colleagues and also friends in the Center for High Energy Physics and the Daya Bay collaborators. The name list is so long but I still want to write it down for these nice folks: Xuhao Yuan, Suzhi Wu, Haibing Zhang, Yanxi Zhang, Guangrui Liao, Yiming Li, Fanfan Jing, Liang Zhong, Yang Zhang, Ligang Xia, Hanyu Wei, Xiangpan Ji, Bei-Zhen Hu, Gaosong Li, Soren Jetter, Jia-Hua Chen, Hussain Ghulam, Kai Liu, Logan Lebanowski, Linyan Wan, Liupan An, Ziyi Guo, Xuesong Liu, Lei Guo, and at last our dear office secretary Ling Zhang and Luping Yang.

In the end, I want to thank my dear parents, my sister and my girlfriend. They accompany with me and encourage me all the time, making me feel be loved.

Declaration

本人郑重声明：所呈交的学位论文，是本人在导师指导下，独立进行研究工作所取得的成果。尽我所知，除文中已经注明引用的内容外，本学位论文的研究成果不包含任何他人享有著作权的内容。对本论文所涉及的研究工作做出贡献的其他个人和集体，均已在文中以明确方式标明。

签 名： _____ 日 期： _____

Appendix A Systematic uncertainty calculation for accidental background subtraction in neutron calibration data

The FGd value for the neutron calibration data can be easily calculated with the delayed spectrum after background subtraction, following the definition of

$$\text{FGd} = \frac{N_{6 \text{ MeV} < E < 12 \text{ MeV}}}{N_{1.5 \text{ MeV} < E < 12 \text{ MeV}}} . \quad (\text{A-1})$$

The uncertainty calculation with the systematic uncertainty from background subtraction is a little tricky.

Firstly, for the accidental background subtraction, the systematic uncertainty mainly comes from the uncertainty of the scale factor (denoted as A) for the singles' spectrum. This scale factor is calculated with the distance distribution for 2-fold raw candidates and single pairs. For a binned delayed spectrum (with prompt energy cut in Table 4.3 to select specific neutron kinetic energy) to do the subtraction, every bin of the spectrum uses the same scale factor, thus the uncertainty contributed from scale factor are correlated for every bin. When we calculate the integral of a given energy region, this correlation should be carefully handled with.

For convenience, in the following discussion, we would tag the energy region from 6 MeV to 12 MeV with suffix 1 and tag the energy region from 1.5 MeV to 6 MeV with suffix 2. The 2-fold raw candidates spectrum before background subtraction is denoted as r (raw), the singles pair spectrum is denoted as b (background), and the spectrum after accidental background subtraction is denoted as n (neutron). The FGd calculation can be presented as

$$\begin{aligned} \text{FGd} &= \frac{N_{6 \text{ MeV} < E < 12 \text{ MeV}}}{N_{1.5 \text{ MeV} < E < 12 \text{ MeV}}} \\ &= \frac{n_1}{n_1 + n_2} \\ &= \frac{r_1 - A \cdot b_1}{(r_1 - A \cdot b_1) + (r_2 - A \cdot b_2)} . \end{aligned} \quad (\text{A-2})$$

The integral of events in energy region 1 and 2 are subsets of the total spectrum from 1.5 MeV to 12 MeV, like the two parts in a binomial distribution. So they are correlated to each other and the uncertainties follow the binominal uncertainty calculation. The raw

candidates spectrum, single pair spectrum and scale factor are independent from each other. These basic uncertainties and covariances are calculated as

$$\begin{aligned}\sigma_{r_1}^2 &= \sigma_{r_2}^2 = -\text{cov}(r_1, r_2) = r_1 r_2 / (r_1 + r_2) \\ \sigma_{b_1}^2 &= \sigma_{b_2}^2 = -\text{cov}(b_1, b_2) = b_1 b_2 / (b_1 + b_2) \\ \text{cov}(s_1, t_2) &= 0 \quad s, t = r, b, A .\end{aligned}\tag{A-3}$$

With these basic uncertainties and the uncertainty propagation principles, the complete uncertainty calculation for FGd can be written as

$$\begin{aligned}\sigma_{n_1}^2 &= \sigma_{r_1}^2 + A^2 \cdot \sigma_{b_1}^2 + b_1^2 \cdot \sigma_A^2 \\ \sigma_{n_2}^2 &= \sigma_{r_2}^2 + A^2 \cdot \sigma_{b_2}^2 + b_2^2 \cdot \sigma_A^2 \\ \text{cov}(n_1, n_2) &= \text{cov}(r_1 - A \cdot b_1, r_2 - A \cdot b_2) \\ &= \text{cov}(r_1, r_2) + A^2 \cdot \text{cov}(b_1, b_2) + b_1 \cdot b_2 \cdot \sigma_A^2 \\ \sigma_{\text{FGd}}^2 &= \frac{n_1^2}{(n_1 + n_2)^4} \sigma_{n_2}^2 + \frac{n_2^2}{(n_1 + n_2)^4} \sigma_{n_1}^2 - \frac{2n_1 n_2}{(n_1 + n_2)^4} \text{cov}(n_1, n_2) .\end{aligned}\tag{A-4}$$

The systematic uncertainty only comes from the uncertainty of the scale factor (σ_A). All other terms are the statistic uncertainty. The total uncertainty of FGd can be categorized by systematic part and statistics part as

$$\begin{aligned}\sigma_{\text{FGd}}^2 &= \frac{n_1^2}{(n_1 + n_2)^4} \sigma_{n_2}^2 + \frac{n_2^2}{(n_1 + n_2)^4} \sigma_{n_1}^2 - \frac{2n_1 n_2}{(n_1 + n_2)^4} \text{cov}(n_1, n_2) \\ \sigma_{\text{FGd}}^2(\text{stat.}) &= \frac{r_1 r_2 / (r_1 + r_2) + A^2 \cdot b_1 b_2 / (b_1 + b_2)}{(n_1 + n_2)^2} \\ \sigma_{\text{FGd}}^2(\text{syst.}) &= \frac{(n_1 b_2 - n_2 b_1)^2 \cdot \sigma_A^2}{(n_1 + n_2)^4} .\end{aligned}\tag{A-5}$$

Equation (A-5) are then used in the neutrino calibration data analysis for uncertainty estimation of FGd.

Resume and Publications

个人简历

1989年10月6日出生于湖北省孝感市。

2005年9月考入湖北省孝感高级中学学习。

2008年9月考入清华大学工程物理系工程物理专业，2012年7月本科毕业并获得工学学士学位。

2012年9月免试进入清华大学工程物理系攻读物理系博士学位至今。

发表的学术论文

- [1] Yiming Zhang for the Daya Bay collaboration, et al. Evolution of the reactor antineutrino flux and spectrum at daya bay. Phys. Rev. Lett., 2017, 118:251801
- [2] F. P. An et al., New measurement of θ_{13} via neutron capture on hydrogen at Daya Bay, Phys. Rev. D 93, 2016, 072011
- [3] F. P. An, et al. , Independent measurement of the neutrino mixing angle θ_{13} via neutron capture on hydrogen at Daya Bay, Phys. Rev. D 90, 2014, 071101(R)